UNIVERSITÀ DEGLI STUDI DELL'INSUBRIA
DIPARTIMENTO DI FISICA E MATEMATICA

OSSERVATORIO ASTRONOMICO DI BRERA

INAF ISTITUTO NAZIONALE DI ASTROFISICA

DOTTORATO DI RICERCA IN ASTRONOMIA E ASTROFISICA
XXIII ciclo

THE E-ELT ADAPTIVE MIRROR: PROTOTYPE AND OPTICAL TESTS

di *Daniela Tresoldi*

Supervisore:
DOTT. EMILIO MOLINARI
Tutore:
DOTT. MAURO GHIGO

Coordinatore della scuola di dottorato:
PROF. ALDO TREVES

a Gabriele
e al ſuo papà

“Captain’s log, Stellardata 32823,21. We have entered a spectacular binary star system in the Kavis Alpha sector on a most critical mission of astrophysical research. Our eminent guest, Dr. Paul Stubbs, will attempt to study the decay of neutronium expelled at relativistic speeds from a massive stellar explosion which will occur here in a matter of hours.” [1]

... otherwise you can build large telescopes. In this way you can look very far with the convenience of remaining down to Earth! And this is the story I want to tell you.

Contents

Abstract

Ground-based optical-infrared 10m-class telescopes, such as Keck, Gemini, and Very Large Telescopes (VLT), are currently leading many of the astronomical research fields due to their unprecedented collecting areas. However, many new astrophysical quests arose from recent observations, justifying the need for even larger telescopes, with diameters >30 m.

The European scientific community, led by the European Southern Observatory (ESO), takes part in this challenging competition whit the "European-Extremely Large Telescope" (E-ELT), a revolutionary project for a 40m-class telescope that will allow us addressing many of the most pressing unsolved questions about our Universe.

Building Extremely Large Telescopes asked for innovative technologies, from larger and repeatable optical manufacturing techniques to produce hundredths of aspherical off-axis hexagonal segments and large monolithic mirrors, or large thin optical shell mirrors, to better and faster controls (active and adaptive optics), together with more specialized focal plane instrumentations devoted to address specific astrophysical questions, more likely to large particle physics experiments.

Moreover the challenge of building extremely large telescope pushes forward the parallel ability to measure and test optical components of large sizes.

Adaptive Optics (AO) techniques allow to obtain enhanced ground-based astronomical observations, partially restoring diffraction-limited spatial resolutions, by compensating the degrading effects of the atmospheric turbulence. The delivered image quality of an AO-assisted telescope depends on the level of the correction of the wavefront error due to the atmosphere.

My work focuses on the adaptive deformable mirror unit (M4AU) of the E-ELT. During my Ph.D. study, I took part in the competitive "EELT-M4 project" study, led by an Italian-French consortium (Microgate, ADS, SAGEM, INAF-O.A.Brera).

Optical measurements were conceived, designed and performed on a similar, scaled-down, fully-representative prototype of the final system, to fully validate the proposed concept. Due to very stringent requirements in term of wavefront correction (10-100 nm rms), only interferometric optical setups were able to provide enough accuracy and sensitivity to carry out the work.

A set of three devices has been designed for the tests:

- a Ritchey-Common test setup (RCT), able to cover the full area of the M4AU DP optical surface with a single measurement, taken with a phase-shifting Fizeau interferometer;
- a Stitching Interferometric Setup (SIS), where a scanning smaller optical beam is able to reconstruct the same optical surface with increased capture range and spatial resolution, useful in the first steps of the calibration procedures;
- a piston sensing unit (PSU), which exploits the optical path difference between adjacent optical shells, after careful analysis of diffraction patterns.

Those devices, together with purposely designed control softwares and data reduction softwares, were used during a 6-months measurement campaign, demonstrating the fully compliance of the prototype system with the requirements to be obtained in the final system (flattening of each optical shell, co-phasing of the optical shells, optical stroke calibration, stability of calibration under time and changing environmental conditions).

Results have been positively reviewed by the EELT project office, and were used as feedback on the design of final optical test system, to be operated on the 2.5m M4AU unit.

Chapter 1

ELT's: The Next Generation

1.1 Challenges and New Technologies

The telescope is an important scientific instrument that from time of Galileo Galilei, allowed to the humanity to "see far" in any sense. It may be said that the first real scientific revolution has happened thanks to the Galilei telescope, realized at the beginning of XVII century.

With his astronomical discoveries, described in his master-work *Siderus Nuncius*, Venezia, 1610 [33], G.Galilei had confirmed the Copernicus Thesis giving rise to the *Copernicus revolution* that which led the end of all geocentric theories.

The history of the telescope is also an excellent example of how the development of science is interlaced to the development of the technology and vice versa. [13]

It is possible emphasize some important steps in the evolution of the telescope sometimes linked to other theoretical discoveries and/or technological inventions.

For example, when was clear that large mirrors were much more easy to build that large lenses then huge advances in the coating techniques was performed. So reflecting telescope have almost dominated the whole history of modern astronomy, starting from the Newtonian telescope.

In the optical design, an important progress was made when in 1637 Descartes, in his opera *"Dioptriques"* [22], studied the conics properties and their use in the production of mirrors without spherical aberrations. In figure 1.1 we can see the evolution of the optical design of the telescope [55], [54].

The well known optical configuration with the use of conical surfaces were created by *J. Gregory* and *L. Cassegrain*. The Gregorian telescope was composed by a primary concave parabolic mirror and a concave elliptical secondary mirror. One focus of the elliptical mirror is the same of the parabolic mirror, in this way the secondary mirror focuses in the second focus of the ellipse.

The second optical configuration, Cassegrain telescope, was composed by a primary concave parabolic mirror and a convex hyperbolic secondary mirror. Again, one focus of hyperbole coincides with the parabola focus and the hyperbolic mirror forms the image in his second focus.

The introduction of the conics in the optical configuration was the most important step into the *modern era*. In the last image of the figure 1.1 lies the Ritchey-Chrétien (RC) configuration. In this optical configuration, the primary mirror is a hyperbolic mirror and the secondary is a convex hyperbolic mirror. In this way the RC design was free of coma and spherical aberration and is capable to reduce significantly the off-axis aberrations. RC configurations are most commonly found on high-performance modern telescopes.

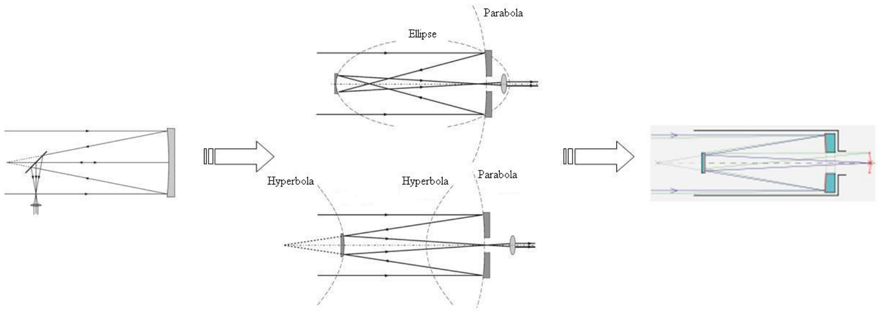

Figure 1.1: Evolution in optical design of the telescope. The first telescope in this picture (left) is the Newtonian configuration. The characteristic of this configuration is the folding mirror at 45° that focalize the beam perpendicular to the principal optical axis. The configuration in the middle of picture are: Gregorian configuration (top) and Cassegrain configuration. This telescope was the first telescope with the use of conical surphaces. The last optical configuration is the Ritchey-Chrétien telescope, with the aid of mathematics, he has succeeded in optimizing a configuration free of spherical aberration and Coma.

This was the first time in history that the concept of optimization in the reflecting telescope was understood in a truly scientific sense.

At this point the main goal is improving the quality of the image (reduce to a minimum aberrations) and increasing the magnification (enhance the resolution).

In the sequence of image in figure 1.2 we show there are the evolution of the telescope. It is evident that the main characteristic in this evolution is the *increasing of the size*. But when the diameter increase, the weight increase (to remember the empirical formula: thickness = 1/6 of diameter) and the large surface change shape under their own weight, moreover, the resolving power of the telescope improove and ***the atmospheric turbulences (seeing) become a problems.***

New technologies were then studied.

The problem of the deformation of the mirror under their weight has been solved with new concept of supporting the mirror. For example the *"active optics technologies"* where the mirror is placed on a support with a number of actuators that adjust actively the shape of the mirror in order to correct the deformation due to the gravity, thermal expansion and other (low-frequency deformation) during the observation, thanks to the help of a wavefront sensor that monitors and detects the smallest deviations from the optimum image quality. In figure 1.3 we can see some example of application of this technologies. The active mirror support of the primary mirror of the TNG (top) and VLT (bottom).

The second innovative technology used in order to enhance the resolving power of the telescope is the *"adaptive optics"* (see figure 1.4). In this case sophisticated, ultrathin deformable mirrors, controlled by computers can correct in real-time for the distortion caused by the turbulence of the Earth's atmosphere. These distortions contrary to the active optics corrected deformations, are mainly high-frequency deformations. A wavefront sensor again control the image quality. This technology is the heart of this thesis, and more details are showed in the next chapter.

The active corrections have a frequency of 10 Hz, while typical frequencies for the adaptive corrections are 100 -1000 Hz. Is therefore clear that another important step through the modern era of the telescope was done with the advent of the powerful computing machine able to handling millions of computations per second.

The first telescope that introduce the technology of *active optics* was the ESO New

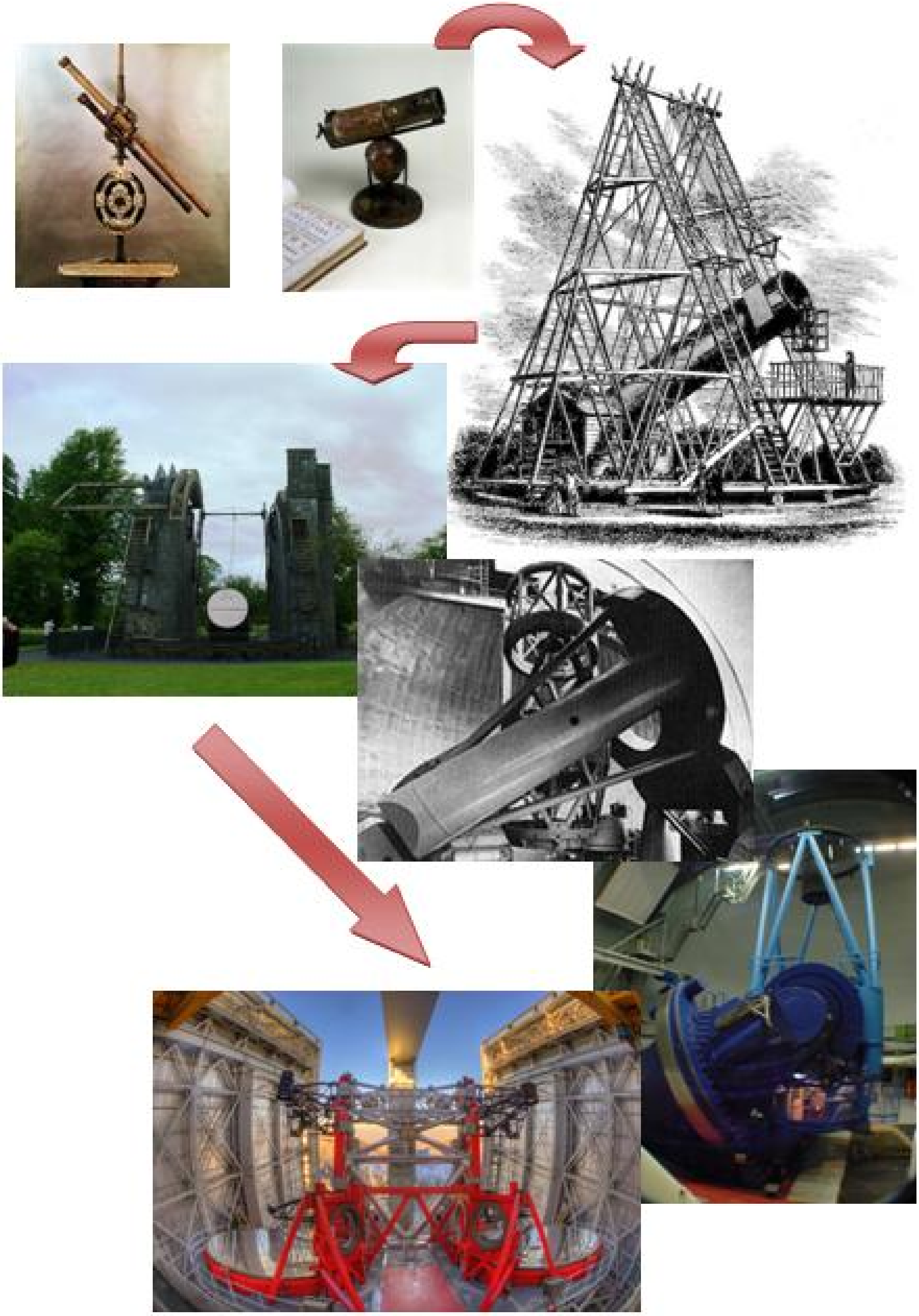

Figure 1.2: The evolution of the instrument "Telescope"

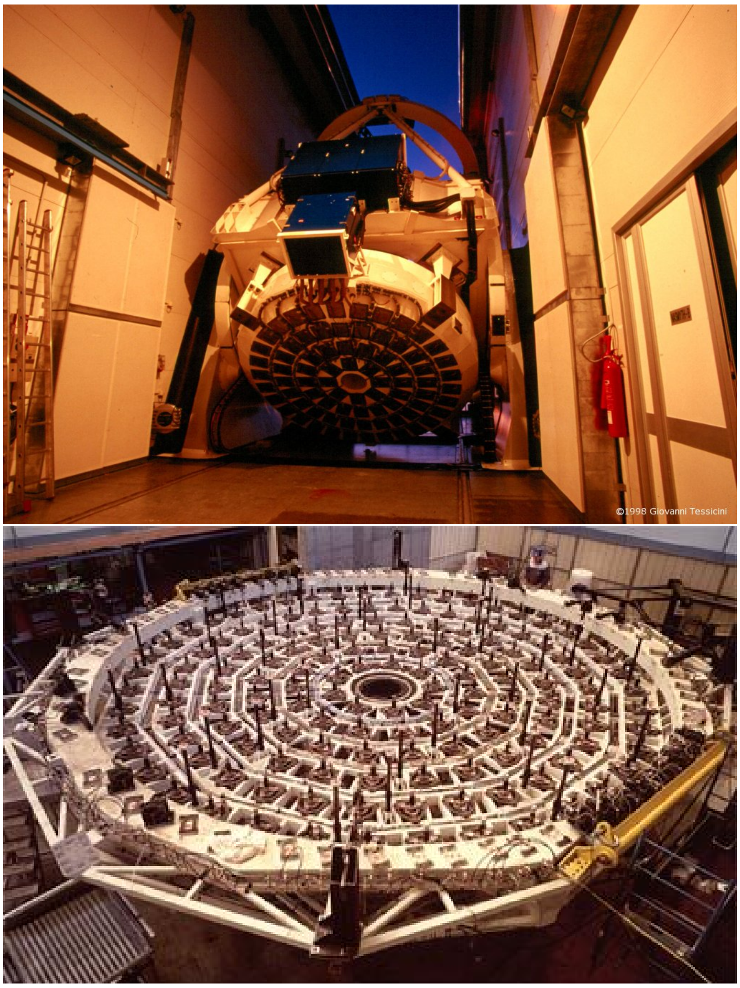

Figure 1.3: The active mirror support of the primary mirror of the TNG (top) and VLT (bottom).

Figure 1.4: An adaptive optics mirror system.

Technology Telescope (or **NTT**) [8], located at La Silla Observatory, Chile, with a primary mirror of 3.6 m diameter. With this system the resolution of the telescope was improved to 0.33 *arcsec* (unit of measurement commonly used to define the seeing. In a typical astronomical image of a star with an exposure time of seconds or even minutes, the different distortions average out as a filled disc called the point spread function or "seeing disc". The diameter of the seeing disk, most often defined as the full width at half maximum (FWHM), is a measure of the astronomical seeing conditions.). To better understand what this means, we can see the two images in the figure 1.5

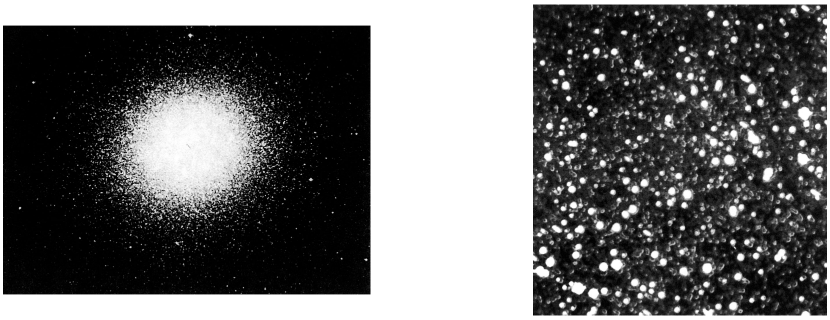

Figure 1.5: left:The Omega Centauri globular cluster of stars is the brightest of its type in the sky and contains several millions of stars. It is here reproduced from a photographic plate obtained with the ESO 1 m Schmidt telescope - right: Small field near center of Omega Centauri (NTT). It shows a field near the center of the bright southern globular cluster Omega Centauri; the size is approximately square arcsecond.

We learned that to improve the quality of our optical system, it is possible to intervene in various ways, for example, use different optical surfaces shapes (aspheric or not), using refractive or reflective elements and using the powerful mathematical tool of optimization. If we desire to increase the magnification power of our telescope, the only thing to do is: increase the size. The current technological capabilities allow the creation of mirrors up to 8-10 m in diameter. But to increase the size of the mirror it is necessary to resort to the *technique of segmentation*.

In order to broaden our horizons in the world of ground telescopes we briefly describe the most important existent telescope in the world. The table 1.1 shows some example of telescope that use the technology of indirect segmentation. The table 1.2 shows instead the telescopes with the direct segmentation solution.

The **Multiple Mirror Telescope** (MMT) [12], located on top of Mt. Hopkins, Arizona, began as indirect segmented telescope. The original configuration of the telescope was effectively six small "individual" telescopes mounted in a circle on the same support structure. Each of the six telescopes had a primary mirror with a diameter of 1.8m. By combining the light of the six small telescopes an effective collecting area of a 4.5m telescope was achieved. In 2000, when progress in the production of large mirrors has been done, the six mirrors were replaced with a single 6.5-m mirror. The telescope enclosure was modified, the optical support structure was replaced, and a single 6.5m primary mirror was installed.

The **Very Large Telescope** (VLT) [5], situated in Paranal, Chile, consists of an arrangement of four large (8.2 meter diameter) telescopes. The telescopes can work all together or in groups of two or three, to form a giant "interferometer", the Very Large Telescope Interferometer (VLTI), allowing astronomers to see details up to 25 times finer than with the individual telescopes. The light beams are combined in the VLTI using a complex system of mirrors in underground tunnels where the light paths must be kept equal to distances less than 1/1000 mm over a hundred meters. With this kind of precision the VLTI can reconstruct images with an angular resolution of

Table 1.1: The telescope that use the indirect segmentation solution

Telescope	**First light**	**Where**	**D**(m)	**Configuration**
MMT	1979 (segm. mirror)	Mt. Hopkins	eq. 4.5	Cassegrain
	2000 (single mirror)	Arizona	6.5	
VLT	1998 (first telescope)	Paranal Chile	8.2	Ritchey - Chrétien
	2002 (all)	Chile	eq. 16	
LBT	2005 first mirror	Mount Graham	8.4	Gregorian Binocular
	2008 binocular vision	Arizona	eq. 11.8	
Gemini	1999 2000	Hawaii'i Chile	8.1	Cassegrain

milliarcseconds, equivalent to distinguishing the two headlights of a car at the distance of the Moon.

The VLT has stimulated a new age of discoveries, with several notable scientific firsts, including the first image of an extra solar planet, tracking individual stars moving around the super massive black hole at the center of the Milky Way, and observing the afterglow of the furthest known Gamma-Ray Burst.

The **Gemini Observatory** [9] consists of twin 8.1-meter diameter optical/infrared telescopes located at different sites in Hawaii and Chile. Gemini Observatory telescopes can collectively access the entire sky. Both of the Gemini telescopes have been designed to take advantage of the latest technology and thermal controls to excel in a wide variety of optical and infrared capabilities.

The **Large Binocular Telescope** (LBT) [10] is a collaboration between the Italian astronomical community, The University of Arizona, the Germany Institute of Astronomie and Astrophysik, The Ohio State University, Research Corporation in Tucson, and the University of Notre Dame. This telescope is a binocular telescope consisting of two 8.4-meter mirrors on a common mount, equivalent in light-gathering power to a single 11.8 meter instrument. Because of its binocular arrangement, the telescope will have a resolving power corresponding to a 22.8-meter telescope.

Table 1.2: Some example of direct segmentation solution

Telescope	**Year**	**Where**	**D** (m)	**Segments**
KeckI	1993	Hawaii	10	36
KeckII	1996	Hawaii	10	36
GTC	2007	La Palma - Spain	10,4	36

The **Keck Observatory** consist of the twin Keck telescopes, in the Hawaii Island. The telescope primary mirrors are 10 meters in diameter and are each composed of 36 hexagonal segments. Because of the large size of the 10-meter primary mirrors, the Keck telescopes offer the greatest potential sensitivity and clarity available in astronomy. The W. M. Keck Foundation funded both the original Keck I telescope and six years later, its twin, Keck II. The project was managed by the University of California and the California Institute of Technology. The Keck I telescope began science observations in May 1993; Keck II saw first light in October 1996.

Gran Telescopio Canarias (also known as GTC or GRANTECAN), with a total surface equivalent to a 10.4m single circular mirror in diameter, is currently the biggest telescope in the world, but still in its final tuning phase, [20].

This is the current situation in the telescope science. Now we are ready to start our journey in the next generation telescope, in the ELT's era.

1.2 The *ELT's* Era

Extremely Large Telescopes are considered worldwide as one of the highest priorities in ground-based astronomy. There are question such [36]:

- *What is* the nature and composition of the universe?

  Ordinary matter can generally be detected directly, from the light emitted by stars, from radiation emitted by hot gas in galaxies and clusters, and by absorption of light from background luminous sources. We can infer the presence of dark matter from its gravitational attraction, which affects the motion of galaxies and the propagation of light. In contrast, the gravitational effect of dark energy is repulsive, manifested by an increase in the rate of expansion of the Universe. A census of these components reveals the surprising result that normal matter accounts for only a small fraction of the composition of the Universe. The rest is dominated by dark energy and dark matter.

- *When* did the first galaxies and *how* did they evolve

  By looking into space to greater and greater distances, we are able, thanks to the finite speed of light, to see further and further back into the past. To see the very first stars and galaxies we must look over enormous distances, some 13 billion light years. So far these objects remain beyond the reach of present telescopes. At lesser distances, moving forward in time, we see galaxies interacting dynamically and forming stars. But it is not yet clear how this produces the diversity of galaxy types that are seen today

- *What is* the relationship between the black holes and the galaxies? We do not know when or how these super massive black holes formed, or how they fit into the overall picture of galaxy formation and evolution.

- *How* do stars and planets form? Stars form within molecular clouds, by a combination of complex physical processes. What determines when these clouds form stars? What determines the masses of these stars? What fraction has planetary systems? There are many questions that we are just beginning to explore

- *What is* the nature of extra solar planet? The exoplanets that have so far been detected are gas giants like Jupiter and Neptune. They were found because their large mass noticeably perturbs the motion of the host star. Surprisingly, many are found very close to their host star. As the higher temperatures there would prevent such planets from forming, it seems that they must have migrated inward, after forming at greater distances. We believe that smaller terrestrial planets exist, but these cannot be detected with present telescopes. Are such planets common? Can they survive the disruption that would result from migration of the massive planets? Do they have atmospheres like Earth?

- *What.... How.... When....*

- ***Is there life elsewhere in the Universe? ...***

that seek answers.

The Extremely Large Telescopes are tools which may help answer these and other questions. At the present there are Three credible projects shown in the table 1.3

Table 1.3: The ELT project

Telescope	**Where**	**D** (m)	**Configuration**	λ (μm)	**Segments**
TMT	Mauna Kea, Hawaii	30	R-C	0.3-30	492
GMT	Las Campanas, Chile	24,5	Gregorian	0.3-25	7
E-ELT	Cerro Armazones,Chile	39-42	Korsch-like	0.3-30	906

The **Thirty Meter Telescope Observatory** Corporation was founded in June 2003 by its partners: the Association of Canadian Universities for Research in Astronomy (ACURA), the University of California (UC), and the California Institute of Technology (Caltech). The core of the TMT Observatory will be a wide-field, alt-az Ritchey-Chretien telescope with a 492 segment, 30 meter diameter primary mirror, a fully active secondary mirror and an articulated tertiary mirror. The optical beam of this telescope will feed a constellation of adaptive optics (AO) systems and science instruments. TMT operating over the wavelength range 0.3-30 μm, provides 9 times the collecting area of the current largest optical/IR telescopes and, using adaptive optics, will provide spatial resolution 12.5 times sharper than the Hubble Space Telescope and 3 times sharper than the largest current-generation O/IR telescopes. For many applications, diffraction-limited observations provide gains in sensitivity that scale like D^4 (where D is the primary-mirror diameter); thus, TMT will provide a sensitivity gain of a factor more than 100 as compared to current 8m telescopes. TMT will couple unprecedented light collection area (almost 10 times more than one of the Keck telescopes) with diffraction-limited spatial resolution that exceeds Keck by a factor of 3. In July 2009, the board of directors of the TMT Observatory Corporation selected Mauna Kea as the preferred site for the Thirty Meter Telescope.

The **Giant Magellan Telescope** (GMT) Consortium has formed around a nucleus of the Partners in the highly successful Magellan Project, the Observatories of the Carnegie Institution of Washington, Harvard University, the Massachusetts Institute of Technology, the University of Michigan, and the University of Arizona. The GMT is the smallest and perhaps most conservative of all the ELT projects. It will consist of a segmented primary mirror of six 8.4 meter, off-axis circular mirrors arranged in a hexagon and a seventh 8.4 meter mirror in the center with an equivalent full aperture of a 24.5 m primary mirror. The 25-meter diameter GMT will produce diffraction-limited infrared images 2.5 times sharper than the current largest telescopes and 10 times sharper than those from the Hubble Space Telescope, enabling the GMT to resolve greater detail and work on much fainter sources. The optical design uses an aplanatic Gregorian prescription with a concave secondary mirror. It will use the latest in adaptive optics technology to correct for image degradation due to atmospheric turbulence. The GMT Consortium officially announced the selection of Las Campanas, Chile.

The **European Extremely Large Telescope** (E-ELT) is a European Southern Observatory (ESO) project which is being developed together with the wider European astronomical community. This project derives in part from an earlier Eso ELT project called the Overwhelmingly Large Telescope (OWL) which was intended to be a 100m diameter optical telescope. The euro-50 project (led by the Lund University with assistance from astronomers from Finland, Ireland, Spain, Sweden and the United Kingdom) is also part of the E-ELT heritage. On 26 April 2010, the ESO Council selected Cerro Armazones as the baseline site. The present core concept is for a telescope with a mirror 42 meters in diameter, covering a field on the sky about a tenth the size of the full Moon. The mirror design itself is revolutionary and is based on a novel five-mirror scheme that results in an exceptional image quality. The primary mirror consists of almost 1000 segments, each 1.4 meters wide, but only 50 mm thick. The optical design calls for a secondary mirror 6 meters in diameter, almost as large as the biggest primary telescope mirrors in operation today. Adaptive mirror are incorporated into the optics of the telescope to compensate the atmospheric turbulence. One of these mirrors is supported by more than 5000 actuators that can distort its shape a thousand times per second. The telescope will have several science instruments. It will be possible to switch from one instrument to another within minutes. The telescope and dome will also be able to change positions on the sky and start a new observation in a very short time. The ability to observe over a wide range of wavelengths from the optical to mid-infrared will allow scientists to exploit the telescope's size to the full extent.

1.3 Adaptive Optics

The performance of all ground-based telescopes, is limited by the turbulence of the Earth atmosphere which distorts astronomical images. When light from a star or another astronomical object enters the Earth atmosphere, atmospheric turbulence (introduced, for example, by different temperature layers and different wind speeds) can distort and move the image in various ways. When the diameter of aperture of telescopes become large, this effect overtop all other effects that deteriorate the images (more detail are illustrated after in this section). The effects of atmospheric blurring can be avoided by going into space. However, facilities like the Hubble Space Telescope are extremely costly to build and operate, and their expense, space-based telescopes remain relatively small. Astronomers have recently overcome the effect of atmospheric blurring using an established and fundamental technique called adaptive optics (AO).

An adaptive optics system tries to correct these distortions, using a wavefront sensor which takes some of the astronomical light and measures the distortions the atmosphere has introduced on the timescale of a few milliseconds, a deformable mirror that lies in the optical path, and a computer that receives input from the detector, processes the data and sends the correction command to the mirror that is reshaped accordingly .

In figure 1.7 it is possible to see the differences between a telescope with or without a system of adaptive optics.

therefore an adaptive optics system is composed of [52]:

- deformable mirror
- wavefront sensor
- computers calculator

1.3.1 Imaging and Atmospheric Turbulence parameters

Some definition:

Under ideal circumstances, the resolution of an optical system is limited by the diffraction of light waves. This so-called *"diffraction limit"* is generally described by the following angle (in radians) calculated using the light wavelength λ and optical system pupil diameter D:

$$\alpha = 1.22\lambda/D$$

What happens if the telescope is not an optical ideal system? The Point Spread Function (PSF) $P(\vec{\alpha})$ take into account all defects introduced by the imperfections of optical elements, noise of the detector, atmospheric turbulences etc. The point spread function (PSF) describes the response of a real imaging system to a point source. The image of

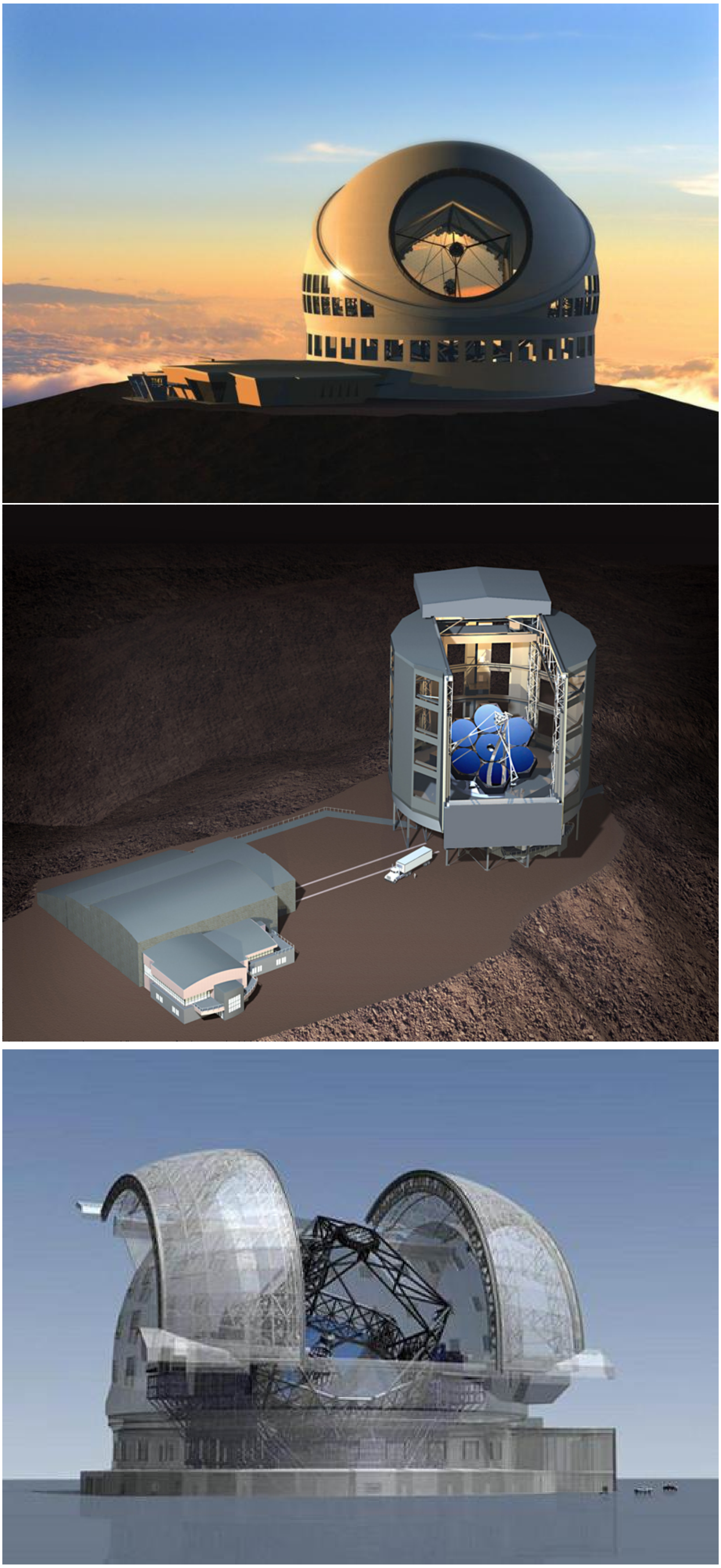

Figure 1.6: TMT,GMT and E-ELT picture

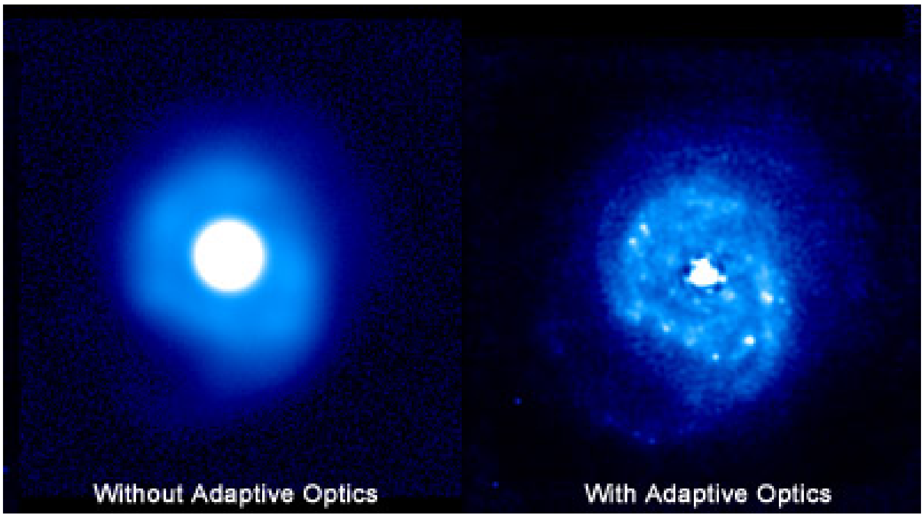

Figure 1.7: The nuclear region of the nearby galaxy NGC7469, with and without AO

a complex object can then be seen as a convolution of the true object and the PSF, so if the object plane field is represented by

$$O(x_o, y_o) = \int\int O(u,v)\delta(x_o - u, y_o - v)dudv$$

mathematically, the image is expressed as:

$$I(x_i, y_i) = \int\int O(u,v)P(x_i - Mu, y_i - Mv)dudv$$

where M is the magnification of the optical system and $P(x_i - Mu, y_i - Mv)$ is the image of the delta impulse function

Other important resolution criteria are:

- *the Full Width at Half Maximum* of the PSF
- *the Strehl ratio*. It is defined as the ratio of the observed peak intensity at the detection plane from a point source as compared to the theoretical maximum peak intensity of a perfect imaging system working at the diffraction limit. The higher is Strehl ratio, the better is resolution. Diffraction-limited image is the best, hence $S \leq 1$ always.
- *the Encircled energy*. By definition, the integral of PSF is equal to 1. The PSF integral over the circle of radius β is called the encircled energy. A typical criterion for encircled energy (EE) is the radius of the PSF at which either 50% or 80% of the energy is encircled

Atmospheric turbulence may be regarded as random phase aberrations added to the telescope. These aberrations constantly change in time, so does the PSF. This is the *seeing*. For large telescopes with good optical quality the resolution is entirely defined by the atmosphere. So the seeing is a reference to the best possible angular resolution which can be achieved by an optical telescope in a long photographic exposure, and corresponds to the diameter of the fuzzy blob seen when observing a point-like star through the atmosphere. The size of the seeing disc is determined by the astronomical seeing conditions at the time of the observation.

The best conditions give a seeing disk diameter of 0.4 arcseconds and are found at high-altitude observatories on small islands such as Mauna Kea or La Palma, while the big telescopes have theoretically milli-arcsecond resolution. The real image will never be better than the average seeing disc during the observation. This can easily mean a factor of 100 between the potential and practical resolution. It is for this reason that big telescopes require adaptive optics corrections.

There are some mathematical models to describe the atmospheric turbulences. The Kolmogorov model developed by Tatarski, ([50]) based partly on the studies of turbulence by the Russian mathematician A. Kolmogorov ([38],[39]), is widely used in simulations of astronomical imaging.

The model assumes that the wavefront perturbations are brought about by variations in the refractive index of the atmosphere. These refractive index variations lead directly to phase fluctuations described by $\phi_a(r)$ while the amplitude fluctuations have negligible effect on the structure of the images seen in the focus of a large telescope.

Another important functions in the atmospheric science is the *Phase Structure Function* $D_\phi(\vec{r})$ that is the average difference between the two values of a random process:

$$D_{\phi_a}(\rho\vec{r}) = \langle|\phi_a(r) - \phi_a(r+\rho)|^2\rangle_r$$

this function can be described in term of a single parameter r_0,

$$D_\phi(\vec{r}) = 6.88\left(\frac{|\rho|}{r_0}\right)^{5/3}$$

r_0 indicates the "strength" of the phase fluctuations as it corresponds to the diameter of a circular telescope aperture at which atmospheric phase perturbations begin to seriously limit the image resolution. It is called *atmospheric coherence radius*, or *Fried parameter*. Typical r_0 values for I band observations at good sites are 20–40 cm. It is clear that r_0 is closely related to the seeing. Approximately if $r_0 = 10.1\ cm \Longleftrightarrow seeing = 1arcsec$ at $\lambda = 0.5\mu m$. The Strehl number of the atmospheric PSF is exactly the same as in an ideal telescope of diameter r_0.

Turbulence can often be modeled as fixed phase screens which are driven by the wind in front of the telescope. Knowing the spatial properties of the phase screens (structure function) and the wind velocity, we know also the temporal behavior of the perturbations. The *atmospheric time constant* τ_0 (or the Greenwood Frequencies $1/\tau_0$) is defined as

$$\tau_0 = 0.31\frac{r_0}{\bar{V}},$$

where $\bar{V}$ is the wind velocity averaged over the altitude. This parameter is important to project an AO system because defines how fast the system need to be. The images of astronomical objects taken with exposure time τ_0 or shorter are called short-exposure images. They correspond to fixed (frozen) atmospheric aberrations. At longer exposure times, the aberrations are averaged, and for exposures much longer than τ_0 the long-exposure PSF is obtained.

Summarizing: r_0 also corresponds to the length-scale over which the turbulence becomes significant (10/20 cm at visible wavelengths at good observatories), and τ_0 corresponds to the time-scale over which the changes in the turbulence become significant. r_0 determines the spacing of the actuators needed in an adaptive optics system, and τ_0 determines the correction speed required to compensate for the effects of the atmosphere.

1.3.2 Adaptive Optics technologies

The generic AO system is presented in the Figure 1.8.

All AO systems work by determining the shape of the distorted wavefront, and using an “*adaptive*” optical element, a deformable mirror, to restore the uniform wavefront by applying an opposite canceling distortion. The most basic systems use a point source of light as a reference beacon, whose light is used to probe the shape of the wavefronts.

This may be a bright star, or a laser guide spot (LGS).

Light from this reference source is analyzed by a wavefront sensor, and then commands are sent to actuators (pistons) which change the surface of a deformable mirror to provide the necessary compensations.

We have previously listed the principal element of an adaptive optics system, now we try to describe it in detail.

Wavefront sensing

The wavefront coming from the stars must be detected and analyzed in order to be corrected. The problem of measuring wave-front distortions is common to optics (e.g. in the fabrication and control of telescope mirrors), and typically is solved with the help of interferometers, but an AO system must use the light of stars passing through the turbulent atmosphere to measure the wave-fronts, hence use incoherent (and sometimes non-point) sources, moreover interferometers have an intrinsic phase ambiguity of 2π, whereas atmospheric phase distortions exceed 2π, typically and even if here are algorithms to "un-wrap" the phase and to remove this ambiguity, they are slow, while atmospheric turbulence evolves fast, on a millisecond time scale. In practice a convenient wavefront sensing must:

- work on white-light incoherent sources
- be fast
- use the photons very efficiently

Different kinds of wavefront sensing (WFS) exist. The most used are the *Shack-Hartmann WFS*, the *curvature WFS* and the *Pyramid WFS*.

The first is perhaps the best known WFS, devised initially for telescope optics control (see [19]). An image of the exit pupil is projected onto a lenslet array.

Each lens takes a small part of the aperture, called sub-pupil, and forms an image of the source. All images are formed on the same detector, typically a CCD.

When an incoming wave-front is plane, all images are located in a regular grid defined by the lenslet array geometry (see fig 1.9) As soon as the wave-front is distorted, the images become displaced from their nominal positions.

Displacements of image centroids in two orthogonal directions x, y are proportional to the average wave-front slopes in x, y over the sub-apertures. Thus, a Shack-Hartmann (S-H) WFS measures the wave-front slopes.

The wave-front itself is reconstructed from the arrays of measured slopes, up to a constant which is of no importance for imaging.

Resolution of a S-H WFS is equal to the sub-aperture size.

The *Curvature Wavefront sensing* was developed by F. Roddier since 1988 [46]. His idea was to couple a curvature sensor (CS) and a bimorph Deformable mirror directly, without a need for intermediate calculations (although nobody actually does this).

In figure 1.10 [4] is shown a scheme of curvature sensor. Let $I_1(\vec{r})$ be the light intensity distribution in the intra-focal stellar image, defocused by some distance l, and $I_2(\vec{r})$ - the corresponding intensity distribution in the extra-focal image. Here $\vec{r}$ is the coordinate in the image plane and F is the focal distance of the telescope. These two images are like pupil images reduced by a factor of $\frac{l}{F-l}$. In the geometrical optics

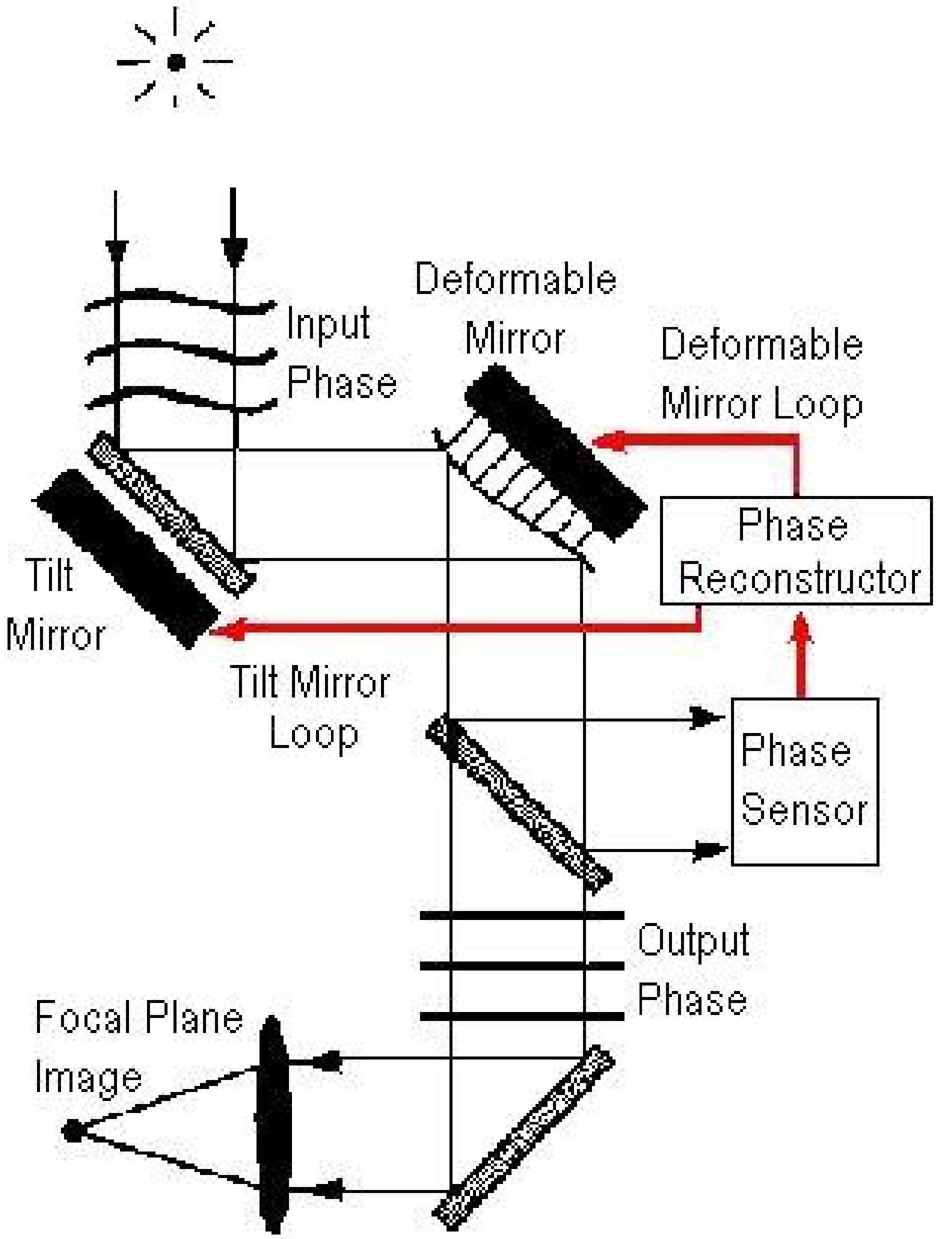

Figure 1.8: Adaptive Optics System scheme

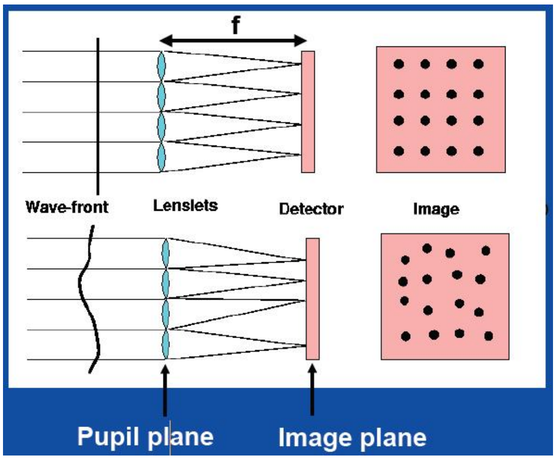

Figure 1.9: Principle of working of a Shack-Hartmann Wavefront Sensor

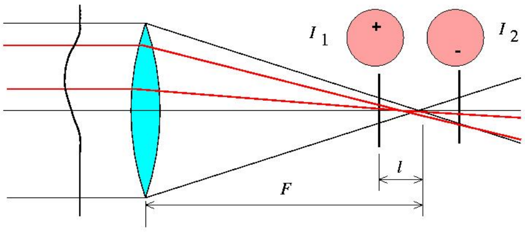

Figure 1.10: Principle of working of a Curvature Wavefront Sensing

approximation, a local wave-front curvature makes one image brighter and the other one dimmer; the normalized intensity difference is written as

$$\frac{I_1 - I_2}{I_1 + I_2} \propto \frac{\partial \phi}{\partial \vec{r}} \vec{\delta}_c - \nabla^2 \phi$$

The operator $\bigtriangledown^2$ is the Laplacian and is used to compute the curvature of the phase distribution $\phi(\vec{x})$. The first term in the above equation is the phase gradient at the edge of the aperture (this is written symbolically as a partial derivative over the direction perpendicular to edge multiplied by an "edge function" δ_c). CS is achromatic (recall that $\phi(\vec{x})$ is inversely proportional to λ).

The important thing is that the sensitivity of CS is inversely proportional to the de-focusing l.

The *pyramid WFS (P-WFS)* is being developed by Esposito et al. (see [25] and [24] for more detail).

A transparent pyramid is placed in the focal plane and dissects the stellar image into four parts. Each beam is deflected, these beams form four images of the telescope pupil on the same CCD detector (see fig. 1.11). Thus, each sub-aperture is detected by 4 CCD pixels. This optical setup is similar to Foucault knife-edge test.

Let us suppose that the light source is extended and use the geometric optics. A wave-front slope at some sub-aperture changes the source position on the pyramid, hence changes the light flux detected by the 4 pixels which would otherwise be equal. By computing the normalized intensity differences we get two signals proportional to the wave-front slopes in two directions. The sensitivity of a P-WFS depends on a source size β. P-WFS can be viewed as an array of quad-cells and is similar to a S-H WFS.

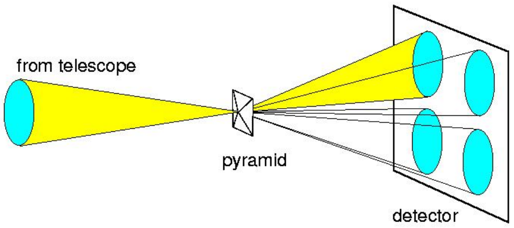

Figure 1.11: Principle of working of a Pyramid Wavefront Sensing

Deformable Mirror

The main parts of a deformable mirror (DM) are: a thin mirror shell, a backplate structure, different actuators and the electronic components.

The shape of the DM can be controlled with a speed that is appropriate for compensation of dynamic aberrations present in the optical system. In practice the DM shape should be changed much faster than the process to be corrected, as the correction process, even for a static aberration, may take several iterations.

A DM usually has many degrees of freedom. Typically, these degrees of freedom are associated with the mechanical actuators and it can be roughly taken that one actuator corresponds to one degree of freedom. Therefore the number of actuator determines the number of degrees of freedom, i.e. the wavefront inflections that the mirror can correct.

It is very common to compare an arbitrary DM to an ideal device that can perfectly reproduce wavefront modes in the form of Zernike polynomials. For statistics of aberrations a deformable mirror with M actuators can be equivalent to an ideal Zernike corrector with N (usually N < M) degrees of freedom.

For correction of the atmospheric turbulence, elimination of low-order Zernike terms usually results in significant improvement of the image quality, while further correction of the higher-order terms introduces less significant improvements.

For strong and rapid wavefront error fluctuations such as shocks and wake turbulence typically encountered in high-speed aerodynamic flow fields, the number of actuators, actuator pitch and stroke determine the maximum wavefront gradients that can be compensated for.

The *actuator pitch* is the distance between actuator centers. Deformable mirrors with large actuator pitch and large number of actuators are bulky and expensive.

The *actuator stroke* is the maximum possible actuator displacement, typically in positive or negative excursions from some central null position. Stroke typically ranges from $\pm 1\ \mu m$ to $\pm 10\ \mu m$. Free actuator stroke limits the maximum amplitude of the corrected wavefront, while the inter-actuator stroke limits the maximum amplitude and gradients of correctable higher-order aberrations.

There are different type of deformable mirrors concept:

- **Segmented concept mirrors** are formed by independent flat mirror segments. Each segment can move a small distance back and forth to approximate the average value of the wavefront over the patch area. Normally these mirrors have little or zero cross-talk between actuators. Stepwise approximation works poorly for smooth continuous wavefronts. Sharp edges of the segments and gaps between the segments contribute to light scattering, limiting the applications to those not sensitive to scattered light. Considerable improvement of the performance of the segmented mirror can be achieved by introduction of three degrees of freedom per segment: piston, tip and tilt. These mirrors require three times more actuators than piston segmented mirrors and they suffer from diffraction on the segment edges. This concept was used for fabrication of large segmented primary mirrors for the Keck telescopes.

- **Continuous faceplate concept mirrors** with discrete actuators are formed by the front surface of a thin deformable membrane. The shape of the plate is controlled by a number of discrete actuators that are fixed to its back side. The shape of the mirror depends on the combination of forces applied to the faceplate, boundary conditions (the way the plate is fixed to the mirror) and the geometry and the material of the plate. These mirrors are often the most desirable implementation, as they allow smooth wavefront control with very large - up to several thousands - degrees of freedom.

- **Microelectromechanical systems (MEMS) concept mirrors** are fabricated using bulk and surface micromachining technologies. MEMS mirrors have a great potential to be cheap. They can break the high price threshold of conventional adaptive optics. MEMS mirrors typically have high response rates, high precision and have no hysteresis, unlike other types of deformable mirrors.

- **Membrane concept mirrors** are formed by a thin conductive and reflective membrane stretched over a solid flat frame. The membrane can be deformed electrostatically by applying control voltages to electrostatic electrode actuators that can be positioned under or over the membrane. If there are any electrodes positioned over the membrane, they are transparent. It is possible to operate the mirror with only one group of electrodes positioned under the mirror. In this case a bias voltage is applied to all electrodes, to make the membrane initially spherical. The membrane can move back and forth with respect to the reference sphere.

- **Bimorph concept mirrors** are formed by two or more layers of different materials. One or more of (active) layers are fabricated from a piezoelectric or electrostrictive material. Electrode structure is patterned on the active layer to facilitate local response. The mirror is deformed when a voltage is applied to one or more of its electrodes, causing them to extend laterally, which results in local mirror curvature. Bimorph mirrors are rarely made with more than 100 electrodes.

Calculator and Controller

The adaptive optics system brain is situated in the modern computers that are able to resolve linear system or to be more precise a quasi-linear system of thousands equations in few milliseconds.

In fact, the measurements come from the WFS data can be represented by a vector S The unknowns (wave-front) is a vector ϕ, which can be specified as phase values on a grid, or, more frequently, as Zernike coefficients. It is supposed that the relation between the measurements and unknowns is linear, at least in the first approximation. The most general form of a linear relation is given by matrix multiplication,

$$S = A\phi,$$

where the matrix A is called interaction matrix. In real AO systems the interaction matrix is determined experimentally and it is often a rectangular matrix: all possible signals (e.g. mechanical modes, Zernike modes) are applied to a DM, and the WFS reaction to these signals is recorded. A reconstructor matrix B performs the inverse operation, retrieving wave-front vector from the measurements:

$$\phi = BS.$$

The number of measurements is typically more than the number of unknowns, so a least-squares solution is useful. In the least-squares approach we look for such a phase vector ϕ that would best match the data. The resulting reconstructor is

$$B = (A^T A)^{-1} A^T.$$

Here superscript T means matrix transpose, and superscript -1 means *pseudo-inverse* matrix. Matrix operations are very frequently encountered in the AO. In almost all cases the matrix inversion presents problems because the matrix $A^T A$ is singular. It means that some parameters (or combinations of parameters) are not constrained by the data. For example, we can not determine the first Zernike mode (piston) from the slope measurements. In practice the matrix inversion is done by removing the undetermined (or poorly determined) parameters with the help of Singular Value Decomposition (SVD) algorithm.

A Laser Guide Star

Most of the current astronomical AO systems use Natural Guide Stars (NGSs or GSs) to measure the wave-fronts. This imposes a severe restriction on the choice of targets. Infact, if some set of targets for observation is selected randomly on the sky, the probability to find suitable guide stars (called sky coverage) may be low.

The idea to use artificial Laser Guide Stars (LGSs), also called laser beacons, for Adaptive Optics appeared in the end of 70-s, although its first open publication is dated 1985. The existing two types of LGS use either the Rayleigh scattering from air molecules or the fluorescence of sodium atoms in the mesosphere, and are called Rayleigh and sodium LGSs, respectively. The Rayleigh LGS use a UV, blue of green laser, the sodium GS use a 589nm laser to excite atoms locate in the sodium layer.

Additional degradation of the AO performance (so-called cone effect) comes from the fact that LGS is at finite altitude, whereas scientific target is at infinity.

The laser spot is formed at some finite altitude H above the telescope: H=10-20 km for Rayleigh LGS or 90 km for sodium LGS. A turbulent layer at altitude h will be sampled differently by the laser and stellar beams. In this way the turbulence above H is not sensed by the LGS and also the outer portions of the stellar wave-front are not sensed. The laser and stellar wave-fronts are scaled differently: the laser beam diameter is reduced by (1 - h/H) times. Hence, there is a differential "stretching" between the LGS and target wave-fronts, so while the laser wave-front is compensated by the AO, the stellar wave-front has a residual error due to the cone effect.

Clearly, the cone effect is a serious limitation precluding the use of LGSs at large telescopes and at short wavelengths, precisely where they are most needed! Several complicated schemes were proposed (but not implemented) that aim to reduce the cone effect by using several laser beams and segmenting the aperture of the telescope, effectively reducing D. We do not discuss them, because the best solution for the cone effect is to use multiple laser beams for reconstructing the 3-dimensional turbulence perturbations.

AO with multiple guide stars: MCAO, MOAO, and GLAO

We have seen that the adaptive optics system have some limitations.

If the long-exposure atmospheric PSF is independent of the viewing direction (is isoplanatic), the instantaneous atmospheric phase aberrations do depend on the direction. Exists a critical angle that limits the distance between guide star and the scientific objects. It is called the *atmospheric isoplanatic angle* θ_0 and his definition is:

$$\theta_0 = 0.31 \frac{r_0}{\bar{h}},$$

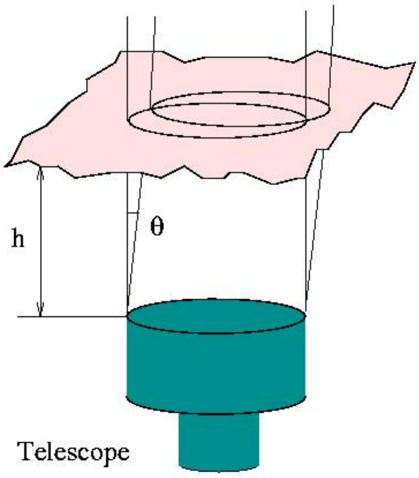

Figure 1.12: The isoplanatic angle of telescope

where $\bar{h}$ is some characteristic average turbulence altitude and r_0 is the Fried parameter. The isoplanatic angle limits the corrected field, and the cone effect avoid a good wavefront correction. Moreover conventional adaptive optics systems are only able to correct for the effects of atmospheric turbulence over a very small patch (a few arcseconds in diameter) of the sky, effectively limiting their use to a single object at a time.

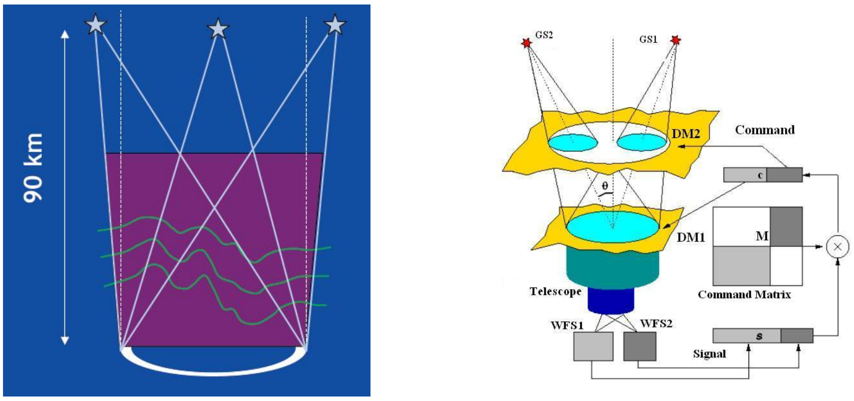

Figure 1.13: left:Reduction of the cone effect in the tomography concept. - right: Multi-Conjugate Adaptive Optics scheme.

In order to solve all this problems, different system have been developed. First the *Tomography concept*, that permits to infer the compensation signal for a target which is at a large angular distance from the GS, with the help of different GSs, LGSs and one deformable mirror. In this way a better compensation quality is achieved comparing to the use of just one GS, and the sky coverage of an AO system with natural GSs is improved. With LGSs, tomography helps to reduce the cone effect (see fig 1.13 left): solving for several turbulent layers from the signals of several GSs permits to combine these layers in a correct way (without stretching or missing portions) to achieve the best compensation for a selected target (for more detail see [16]).

The *Multi-Conjugate Adaptive Optics* (MCAO) is a further development of the original AO concept. It consists in correcting the turbulence in three dimensions with more than one deformable mirror (DM) and more wavefront sensor. Each WFS looks at one star, each DM (see the Figure 1.13, right) is optically conjugated to a certain distance from the telescope. The correction applied at each DM is computed using all the input data. We call this conjugation altitude, although the term range would be more correct. The benefit of MCAO is reduced anisoplanatism, hence an increase of the compensated field-of-view (FoV) size. As field of view increases, average Strehl drops and variation over field increases.

In the figure 1.14 we can see the predicted performance of MCAO. It is a simulation of Multi Conjugate AO correction of a crowded star field.

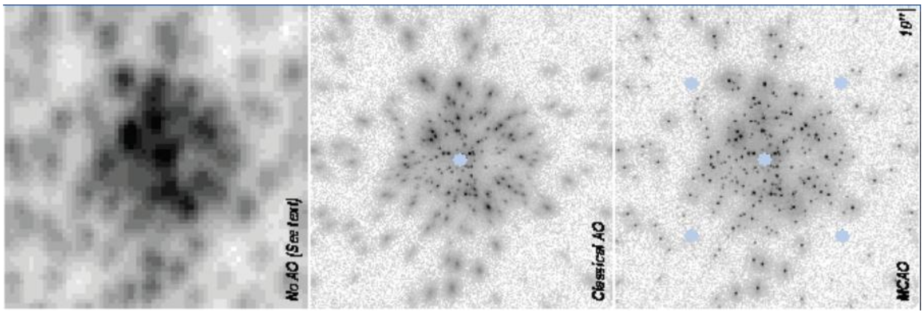

Figure 1.14: Simulation of MCAO performances with 320 stars in K band with 0.7" seeing

Another wide field AO technique is the *Multiple-Object Adaptive Optics* (MOAO). MOAO also requires multiple wavefront sensors and deformable mirrors to correct over a wide field but can be differentiated from MCAO in two principal ways:

1. Rather than correcting for the entire field of view, MOAO corrects only along individual lines of sight within a wider field of view. This means that a single DM will be used to compensate for the effects of atmospheric turbulence for every single target within the telescope field of view.
2. So that the number of wavefront sensors can be less than the number of deformable mirrors, each DM is operated in open-loop i.e. without any feedback to the output of the processes.

Several LGSs are used to measure the turbulence above a telescope. By comparing the light from each LGS, the turbulence in any direction above the telescope can be calculated. The correction required for each individual science target is applied to an individual DM that points along a single line of sight.

The last wide field AO technique is the *Ground-Layer Adaptive Optics* (GLAO). GLAO uses one ground-conjugated DM, corrects near-ground turbulence

Summary:

- Tomography: a way to measure the full volume of turbulence above the telescope
- Once you have measured the turbulence and know its height distribution, there are several ways to do the wavefront correction to get wider field of view
  - Multi-conjugate AO: multiple DMs, each optically conjugate to a different layer in the atmosphere.
  - Multi-object AO: correct many individual objects, each over a small field.
  - Ground-layer AO: correct just the turbulence close to the ground. Gives very large field of view but only modest correction. Should work in both the visible and the IR.

This is the current scenario in the Adaptive Optics science.

Chapter 2

The European Extremely Large Telescope

The E-ELT is an ambitious project of the European Southern Observatory (ESO). I will describe the whole telescope project, with a brief look at future possible instruments at the focal plane.

2.1 The E-ELT Project

(*Most informations present in this chapter are taken from:*
http://www.eso.org/sci/facilities/eelt/docs/index.html [6])

Europe is at the forefront of all areas of contemporary astronomy, thanks, in particular, to the flagship ground-based facilities operated by European Southern Observatory (ESO), the eminent intergovernmental science and technology organization in astronomy.

The challenge is to consolidate and strengthen this position for the future. This will be achieved with a revolutionary new ground-based telescope concept, the European Extremely Large Telescope (E-ELT).

The E-ELT project is coordinated by ESO for its community. The organigram in figure 2.1 sketches the project structure. Blue boxes mark structures internal to ESO, green-ones show community committees and green/blue ones denote mixed committees.

The E-ELT program office (dotted square in the organigram) coordinates the E-ELT activities within ESO. It is headed by the Principal Investigator and includes three project offices: one for the telescope, one for the instrumentation and one for the operational aspects.

The program office is further complemented by the Project System Engineer and the Project Scientist (in charge of the E-ELT Science Office).

The Principal Investigator coordinates the ESO and community efforts in the framework of the EU sponsored FP6 and FP7 activities. The Principal Investigator and the Project Scientist are advised by the Science Working Group.

The Instrument Project Office coordinates ten instrument studies.

The basic reference design for the European Extremely Large Telescope was completed in April 2006. The starting point of the project was located in the five report produced by five working groups composed by ESO and community experts. This working groups were:

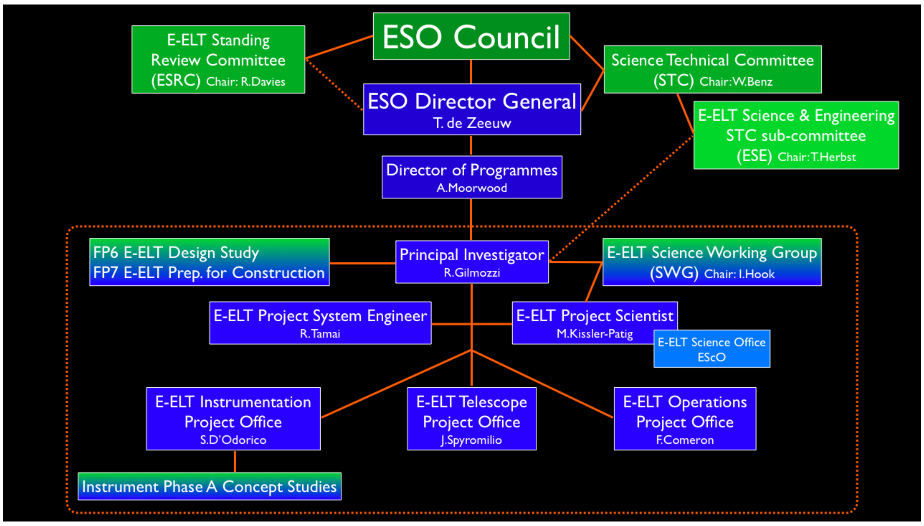

Figure 2.1: Organigram of the E-ELT project (2008)

WG1 Science - The ESO-ELT Science Working group studied science cases for the ESO-ELT in the beginning of 2006. The working group established, developed, and discussed a list of individual science cases and how these would be impacted by trade-offs in the telescope aperture and instrumentation suite. One of the important goals of the Science Working group was to estimate the scientific capabilities using a homogeneous set of assumptions.

WG2 Instruments - The Instrumentation ELT Working Group has drawn together with work done to date on instruments for ELTs, and generated a list of key issues and requirements from the instrumentation point of view for the telescope and AO teams to consider in optimizing the specification and design of a European ELT.

WG3 Site Evaluation - The WG3 has been tasked to categorize site characteristics, to list all sites considered throughout the world (including Antarctica). Probably the most important issue concerning the ELT site selection was the need of a comprehensive and homogeneous data base which covers a long enough time period (years/decades).

On 26 April 2010, the ESO Council selected Cerro Armazones as the baseline site for the planned 42-meter European Extremely Large Telescope (E-ELT). Cerro Armazones is a mountain at an altitude of 3060 meters in the central part of Chile Atacama Desert, some 130 kilometers south of the town of Antofagasta and about 20 kilometers from Cerro Paranal, home of ESO Very Large Telescope.

WG4 Telescope Design - The Telescope Design Working Group attempted to define the pros and cons of every design and gave a summary of the main design features in order to facilitate the discussion with other working groups and hopefully reach a consensus. For the sake of simplicity, an aperture of 42 m (geometric average area between 30 and 60m) has been selected on the ground that any 42m concept could also be up or down scaled for any size between 30 and 60m. The telescope design has been to consider requirements set by the users and, more specifically by instrumentation constraints. In addition, the design has been to take into account technological constraints imposed by its subsystems, for example the feasibility to manufacture large mirrors and to operate adaptive optics systems. Trade-offs has be done in order to accommodate demanding and sometimes incompatible requirements, to contain the cost and finally to make the telescope reliable and maintenance friendly.

WG5 Adaptive Optics - The AO WG wanted to raise the following statement. While it is well recognized that adaptive optics is absolutely essential for an ELT, we have to keep in mind that it represents a challenge. The complexity of the systems to be built is very high when compared to the systems in operation today. Most of the key components are substantially "larger", like the number of actuators in deformable mirror for instance. However, some key technologies, relevant for ELT, are already under development through FP6 programs like OPTICON and the ELT Design Study. The requirements of the AO systems are driven by the scientific goals of the ELT, converted into scientific instruments. Additional requirements are given by the telescope needing adaptive correction to reach its performance.

E-ELT Advanced Preliminary Design

In December 2006 the ESO Council resolved that ESO should proceed into Phase B (detailed design) with the aim to have a proposal for construction ready to be submitted to the ESO Council in 2010.

During this phase, the project placed contracts with industries and institutes in Europe amounting to about 60 million euros including 110 FTEs (Full-time equivalent). During phase B, contracts have been placed with industry for the advancement of major subsystems to preliminary design status. Specifically, contracts were set in place for the development of the main structure, the dome, the adaptive mirrors (the principal argument of this thesis), the tip-tilt unit and the primary mirror support.

Several prototype mirror segments have been procured and polished to the specifications of the project: this enable industrial partners to establish robust production processes.

Integrated modeling, development of concepts for the control system, the mirror cells and the adapter rotators are ongoing, as is the design of the secondary unit.

For critical subsystems where more than one technology exists or where more than one approach is possible, multiple contracts have been placed. The E-ELT construction proposal was submitted to the ESO governing body by the end of 2010.

The construction phase is planned to start in 2012 and the construction cost is estimated to be around 1050 K euros.

2.2 Science with E-ELT

It is very difficult to design an overall picture of the situation of what will be possible to see and discover with the E-ELT. It is sure that the universe will have new wider boundaries thanks to the higher sensitivity and resolution of the new telescope generation. Moreover, like it happened for the 8-10m class of telescope, we hope that the knowledge of the astronomy and astrophysics sciences will be enlarge above expectations.

The science cases that the community has selected, have been divided in three main categories (for more detail see [53]):

1. Planets and Stars
2. Stars and Galaxies
3. Galaxies and Cosmology

Planets and Stars

In this research's branch we found different key points. First of all the study and research of *exoplanets*. The planets are very faint light source, and their direct detection is very difficult also because the planets revolve around their parent star, usually a million times brighter. For these reasons different methods exist for detecting it. The most used is the *radial velocity method.* The presence of a planet in the gravitational field of a star causes variations in the star's radial velocity with respect to Earth that can be detected from displacements in the star's spectral lines due to the Doppler effect. With the large collecting power of the E-ELT, will be possible to detect reflected light from mature giant planets (Jupiter to Neptune-like) orbiting at separations smaller than 1 AU around thousands of stars up to distances of 50 pc. And with the help of ultra-stable spectrograph will achieve measurement precisions of 1 cm/s in the radial velocity method. This is the precision needed for the detection of rocky planets. These studies will lead to an understanding of the formation of Solar System twins and will provide an answer to an important part of the fundamental question: *"Are we alone in the Universe?"*

Another research field that will be possible to expand with the E-ELT is related with the birth, the life, and the death of stars. The E-ELT, with its gain in sensitivity and, in particular, in angular resolution, will be a major player in proto-stellar/proto-planetary disc research, even in their early stages. High spatial resolution imaging will make it possible to probe the full range of stellar and brown dwarf companion masses. Direct imaging with high contrast will enable the detection of brown dwarfs and giant planets orbiting within several AU of the central star. Thus, the E-ELT will reveal the evolution of sub-stellar mass objects, supporting its work on exoplanets and bringing us closer to a full understanding of the evolution of planets and stars over the full mass spectrum. At the end, the E-ELT will be able to study supernova explosions in very high resolution detail. Understanding the evolution of stars is critical to our understanding of the evolution of the Universe: the continuous recycling process of matter, the energetic processes shaping the interstellar medium, the feedback processes in the evolution of galaxies, and the overall chemical enrichment history of the Universe, all the way to the chemistry enabling life (*"We Are All Made of Stars"*).

Another important area of study in astrophysics is the formation and evolution of circumstellar disks. The European ELT will make crucial contributions to this field, the goal will be to search for gaps non-axisymmetric structure such as spirals and hot spots in the young and more mature disks, indicative of ongoing or completed planet formation (high quality, high contrast adaptive optics over a limited field (few arcsec) is required at 2-20 microns).

Stars and Galaxies

Galaxies are the main building blocks of the visible large-scale structure of the Universe. When you look out a galaxies what you see is nothing more than the light of the stars in the galaxy. The galaxies are made up of billions of stars of all ages and chemical compositions. This is why it is very important to be able to resolve the stellar population in distant galaxies. Only an extremely large telescope with his unprecedented high spatial resolution will be successful in this challenge.

It is clear that to understand the formation and evolution of any galaxy it is necessary to investigate the different stellar components, which together carry a memory of the entire star forming history. Low mass stars have extremely long life times, comparable to the age of the Universe, and can retain in their atmospheres the gas, with the elemental abundances intact from the time of their birth. Thus if the stars of different ages are picked out of a stellar population, and this is most accurately done if the population is resolved into individual stars, then the star formation rate and metallicity at different times is measured directly.

Another goal is to investigate young massive star clusters in order to study the formation conditions of star clusters and the formation of high mass stars in general.

The study of individual stars in nearby and distant galaxies not only reveals the history of their host, but is also crucial for our understanding of fundamental star formation and stellar evolution. The predominant factor determining the evolution of a star is its initial mass. The initial mass function (IMF) is a fundamental physical property of stellar populations and is one of the most crucial ingredients in models of galaxy formation and evolution. Knowledge of the IMF is very much needed if we want to understand the star formation history and chemical enrichment of galaxies of various types as well as their photometric properties, so we need access to stars with a wide range of masses and metal content, to probe a star formation environment as diverse as possible.

The availability of the Extremely Large Telescope, with its combination of resolving power and collecting area, will make this research possible for the first time.

Further, to space out even in the AGN research field, the high angular resolution and sensitivity of an ELT will allow mass determination of Black Holes with masses similar to the one in the center of the Milky Way out to the distance of Virgo, to resolve bright stars in the circumnuclear region and so the measurement of age, metallicity and velocities of the nuclear stellar populations in the host galaxy, to obtain estimates of BH masses throughout the universe. Such measurements are fundamental to the understanding of the relationship between the evolution of the BH and the host galaxy, including the possible connection between AGN and Star burst activity.

The E-ELT will expand the portion of the Universe resolvable into stars by a factor of more than ten. It will allow scientists to obtain accurate knowledge of the present day stellar populations in galaxies out to nearby galaxy clusters. It will return a comprehensive picture of galaxy formation and evolution through a detailed study of stellar populations in nearby galaxies and provide the most stringent tests to date for current theories of galaxy formation

Galaxies and Cosmology

At the end of the 1990s the measured dimming of Type Ia supernovae (used as standard candles) with increasing redshift revealed that the expansion of the Universe is not slowing down but appear to increase. This result has profoundly changed cosmology and implies a need for new physics. The most direct way to probe the nature of the acceleration in order to distinguish between these possibilities is to determine the expansion history of the Universe.

With an instrument like the E-ELT, will be able to determine the accelerating expansion of the Universe directly, allowing us to quantify the nature of the dark energy responsible for the acceleration, by measuring the time derivative of the redshift of objects at fixed coordinate distance. As the redshift of the spectra of distant objects is an indication of the expansion of the Universe, so is the change in this redshift with time a measure of the change of the rate of expansion. The wavelength shift corresponds to a Doppler shift of about 2-20 cm/s over a period of 10 yrs. It has a very characteristic redshift dependence and increases linearly with time. Measuring such a small wavelength shift requires a substantial improvement in the accuracy of the wavelength calibration compared to existing spectrograph and a sufficient numbers of photons to measure the shift statistically from a large number of spectral features observed with very high signal-to noise.

With the E-ELT will be possible to study the reionization epoch, by study galaxies at redshift around 8-10 with high resolution spectroscopy, or by observation of quasar or GRB with redshifts larger than of 8 or more.

The large diameter of the ELT will enable very high spatial resolution imaging and spectroscopy, and thereby unique insight into the physical processes occurring in the high redshift galaxies. Imaging at this resolution will give immediate insight into the dynamical state of the galaxy, and will address questions like: is the galaxy merging? Is there a rain of small galaxies/units falling in? Does the galaxy have a wind? Does it have a cold disc? etc.

At the end, only astronomical observations hold the potential to probe the values of fundamental constants in the past, and in remote regions of space.

2.3 E-ELT Optical Design concept

In this section we describe the configuration selected for the telescope optical layout. We refer to [21]. The starting point of the optical design is that the extremely large telescope will rely on adaptive corrections, so the telescope is a *diffraction-limited*.

This fact imposes an increase in the requirements on optical quality of the telescope. For this reason, the optical design is not a simple Ritchey-Chrétien solution, like the most optical design of huge telescope, able to correct the image quality over a 30 arcmin of field of view but in a *seeing-limited* telescope, but is based on five mirrors solution, three of theme with optical power (three-mirror anastigmatic designs see [40]). (see Figure 2.2 for a direct comparison of image quality between a Ritchey-Chrétien solution and a five-mirror solution with the same f-numbers of the primary mirrors and the telescopes.)

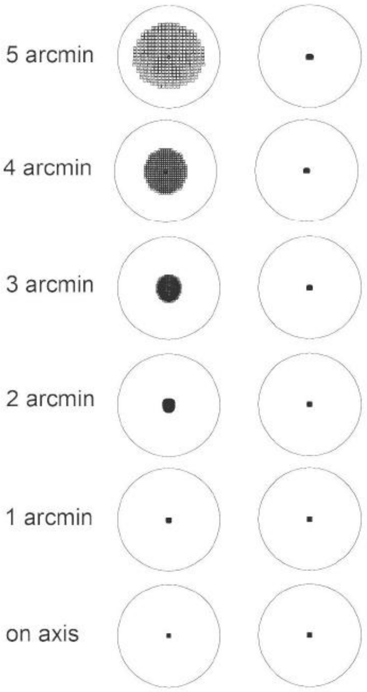

Figure 2.2: S
pot diagrams at various field angles produced by a Ritchey-Chrétien (left) and the five-mirror design (right) with identical f-numbers of the primary mirrors and the telescopes. The diameter of the circles is 0.2 arcsec.

The goal is that the telescope should be able to correct, at least partially, the wavefront aberrations generated by atmospheric turbulence in the ground layer, over a field of view with a diameter of approximately 10 arcmin, because if this correction will be achieved by a post focal instrument, the field of view corrected will be limited at 2 arcmin. In addition, the design of a telescope should take into account the instrument requirements.

These considerations are reflected in the telescope requirements. For example the adaptive mirror should not be strongly tilted, in order to be sure that every point of the wavefront to be corrected, covers the same path and should be conjugated to a layer approximately 200 m above the ground, in order to correct the major component of the atmospheric distortion. For technological reasons, the dimension of adaptive mirror are limited at about 2.5 m in diameter, at the same time the mirror should be large enough to accommodate a sufficient number of actuators in order to correct the wavefront errors with small strokes.

The requirements of small strokes is the reason why the fast tip-tilt, which need large strokes, should be made by a different mirror. To avoid strong pupil movements in the instruments, such a mirror should be close to a telescope pupil.

In addition, in order to meet the instrument requirements, the telescope design should have a focal ratio of about 15. The instruments of a telescope like ELT will be bulky and heavy. The telescope will then have a Nasmyth focus, where it will be possible to install stable platform, and for instruments with extreme stability requirements, both in terms of gravity and temperature, the telescope should also offer a Coudé focus.

Another important question is the spherical or not spherical shape of the primary mirror. If the primary mirror has a spherical shape, we known that the cost of realization will drastically reduce, and the alignment procedure will be easier, but we introduce in the image quality of the telescope huge spherical aberration that should be removed with the help of other optical element (increasing the number of the mirrors), and this made much more complicated the optical design and decreasing the design performances of the telescope. For this reason the final choice is to design an aspherical primary mirror. The main features of the present optical design are summarized in table 2.1 where *Th* is the distance to the following optical element for the first four mirrors and the distance to the focus for M5.

Table 2.1: Fundamental optical parameters of the five-mirror design

Surface	***Th*/mm**	r_{curv} **/mm**	**D**	
M1	-36200.00	84000.0	42000	
M2	42800.00	-14800.0	5985	
M3	-16 000.00	24790.0	4290	
			$d_{long} - d_{short}$ outer edge	$d_{long} - d_{short}$ inner hole
M4	6000.00	∞	2570 - 2490	710 - 700
M5	-33309.61	∞	2834 - 2360	350 - 200

All these considerations have led to the following optical five mirrors design for the E-ELT (see the figure 4.7)

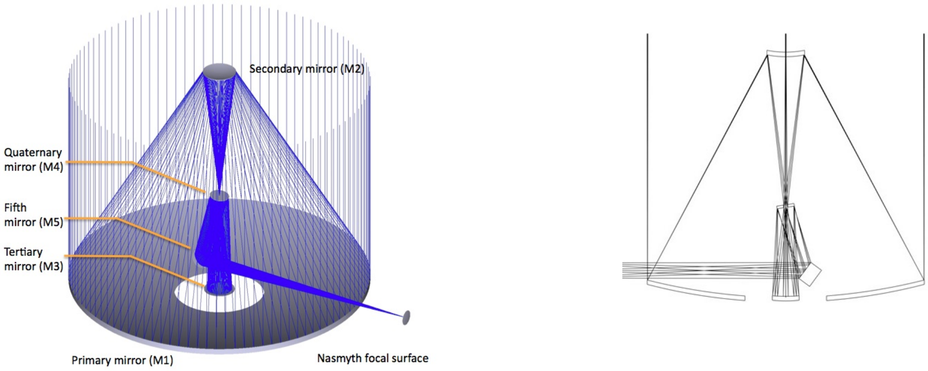

Figure 2.3: E-ELT optical layout

In this optical design the output beam is an f/17.7 and it is very nearly diffraction limited over the entire 10-arcminute field of view. But to achieve an image quality as close as possible to the theoretical values all powered mirrors should be active.

Summarizing, *the E-ELT will be a five-mirrors optical design with adaptive corrections and will be diffraction limited over a field of view of 10 arcmin at a visible wavelength.*

This optical design strikes the balance between the cost, schedule, risk and the technological challenges from one side and the 42pgkhg image quality and other performances of the telescope from the other.

2.3.1 Other E-ELT Characteristic

The Mirrors

The primary mirror is a segmented mirror composed by 984 hexagonal segments and uses a common support structure for all segments. The dimension of each segment is 1.45 m corner to corner and 50 mm thick. Each segment is supported by an identical whiffletrees with 27 axial support points that can move each segment in piston and tip-tilt using three position actuators in order to compensate for deflections.

The secondary mirror is a thin meniscus convex active mirror of 5.6 m in diameter with 156 axial actuators. Six position actuators provide the alignment functions.

After the secondary mirror the beam is direct into the Adaptive Relay Unit Tower (ARU) composed by the tertiary mirror M3, that is another thin meniscus active mirror, 4.2 m of diameter able to provide a variable focal length for the telescope with a flexible positioning system used to shift the mirror in all six degrees of freedom.The flat adaptive mirror of 2.6m diameter, for high temporal frequency (M4) and the tip/tilt, field stabilization unit (at low temporal frequency) M5, that is a second flat mirror with dimensions approximately of 2.4 m by 3.0 m.

The Telescope Main Structure

The telescope structure is an alt-az mount. Two massive cradles provide the rotation of the altitude axis while two azimuth tracks take the axial loads and allow the rotation of the telescope about the zenith. The main structure of the telescope was designed to comply with critical performance needs, such as pointing and tracking specifications of 1 and 0.3-arcseconds, respectively. The azimuth structure contains also the two Nasmyth platforms, mounted on the sides of the azimuth ring and the base for the support of the altitude cradles. The altitude structure hosts the telescope optics. The whole structure weighs nearly 5000 tons.

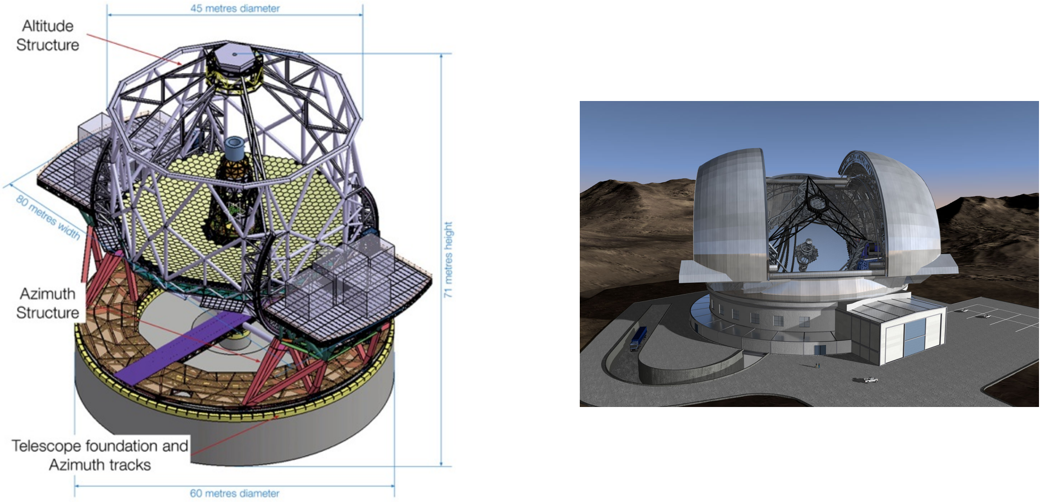

Figure 2.4: E-ELT main structure (left-side) and dome(right-side)

The Dome

The structure has a height of nearly 87 meters from the ground and almost 100 meters of diameter, with a single pair of large sliding doors for the observing slit. The relative size of the opening to the total dome size is very large. In terms of astronomical performance the dome is required to be able to track about the 1-degree zenithal avoidance locus and preset to a new target within the allocated 5 minutes for the preset. This requires the dome to be able to accelerate and move at angular speed of 2 degrees/s. The dome is designed to allow complete freedom to the telescope to position itself within the dome whether it be opened or closed and to permit observations from zenith down to 20 degrees from the horizon. It requires the presence of a windscreen to protect the telescope and is fully air-conditioned.

NOTE

The ESO consortium has recently endorsed a revised baseline design for the E-ELT. The overall concept of the 40-meter-class telescope remains unchanged. A slight reduction of the diameter of the primary mirror to 39.3 meters combined with a faster f-ratio, allows a more compact dome and main structure. This leads to a significant cost saving, as well as reduced risk on major items such as the secondary mirror.

A summary of the telescope characteristics can be found below and for more detail in [7]

The present concept features as a baseline for the primary mirror (M1) an elliptical f/0.93 segmented mirror of 39-m diameter and a 11.1-m central obstruction. The 4.2-m secondary mirror (M2) is convex and returns the beam, through a hole in the quaternary mirror (M4), to the 3.8-m mildly aspheric concave tertiary mirror (M3) located at the vertex of the primary. The beam is reflected by M3 to the adaptive optics system, the 2380x2340mm quaternary flat adaptive mirror M4, supported by up to 8000 actuators, and the fifth mirror in the train (M5) that allows for the final image correction. M4 is inclined at 7.75 degrees to the beam direction. M5 is a flat mirror, elliptical in contour, defines the altitude axis of the telescope and steers the beam towards the Nasmyth focus. The output beam at f/17.48 is very nearly diffraction limited over the entire 10-arcminute field of view. The total Nasmyth field of view is limited to 10 arcmin by the dimensions of the way-through hole in M4. The rather large Nasmyth focal ratio is constrained by the backfocal distance, and the location and size of mirrors M4 to M5.

2.4 Focal Plane Instrumentation

After the definition of the science case and the optical design of the telescope, it is important to talk about the instrument that will work on board of the telescope. In parallel to the telescope phase B, ten phase-A instrument studies were launched starting in September 2007 and lasting until March 2010. The plan identified six instrument concepts, two post-focal AO modules (MCAO and LTAO) of high priority.

CODEX As seen in the scientific case, many scientific problems require high-resolution instruments. The research of the exoplanets, the resolution of galaxies in stars, the determination of the acceleration of the Universe etc. and one of the major benefits that derive from the realization of an extremely large telescope, it is an incredible gain in resolution. *COsmic Dynamics and EXo-earth* experiment, is an optical, very stable, high spectral resolution instrument. CODEX is designed as a single-object fiber-fed spectrograph with a spectral coverage of 350-720 nm and with a wavelength resolution of R $\geq$ 120,000, working under natural seeing conditions, and capable of radial velocity measurements with an accuracy of

2 cm/s over decades. Key to reaching this ambitious stability goal is the laser frequency comb - a novel, nearly perfect calibration source that should become available in time for the CODEX and E-ELT. This instrument will be placed at the Coudè focus of the E-ELT, the light of the focal plane is transferred from the fiber into the spectrograph. A pupil slicer unit, splits the pupil in 6 parts, grouped in 2 slits creating two images of the fiber core (for more detail see [28]). A three mirror anastigmatic collimator, used in double pass, collimates light onto a 1.7m R4-echelle where it is dispersed. A transfer collimator creates a collimated beam for each dispersed image, where a dichroic is placed and splits the light into two arms, optimized for blue and red spectral ranges. Slanted VPHG acts as cross-disperser and beam compressor as well. Finally the cameras focus light on the detectors.

EAGLE EAGLE is a wide-field multi IFU near-infrared (NIR) (IZ, YJ, H and K) spectrograph, covering a field of view of 50 square arcminutes. It will be an instrument designed to study the physics and evolution of high-redshift galaxies, or for detection and characterization of first-light galaxies or even to study the stellar content, the mass functions and the dynamics of stellar clusters. In this context, its science case calls for improved angular resolution (75-100 mas) but not diffraction-limited performance. It is need high sensitivity and a more demanding adaptive optics unit. The instrument will be capable of observing twenty (20) science targets simultaneously and the atmospheric disturbances will be corrected for by making use of an Adaptive Optics system. The 20 science fields (1.65 x 1.65 arcseconds on sky) will be re-imaged and presented to 20 IFUs which will partition each into 44 identical slices. These slices will re-image the original science field at the input focal plane of the spectrograph entrance slit. Each slice will be dispersed along the spatial direction of each slit (2 pixels) and presented to one half of a 4 K x 4 K detector, generating a 44 x 44 spatial partitioning for each of the science fields (for more detail see [31]). Due to the large field-of-view, a multi-object adaptive optics (MOAO) system will control the GLAO corrected field of the ELT (M4 and M5) with an additional Deformable Mirror (DM) in each channel of EAGLE. Six Laser Guide Stars (LGS) and five Natural Guide Stars (NGS) shall be required to achieve the performance required.

EPICS The *Exo-Planet Imaging Camera and Spectrograph* is an instrument projected for the direct imaging and characterization of extra-solar planets, namely detection of young giant gas planets in star forming regions, detection and characterization of mature gas giants at orbital distances between 5 and 15 AU in the solar neighborhood ($<$ 20 pc) with the goal to determine frequency and mass distribution of giant planets not easily accessible to radial velocity, astrometric or photometric techniques. For this field of research, it is needed high-resolution, high-sensitivity and high contrast level. In particular:

1. The systematic intensity contrast of the instrument should be better than 10^{-8} at 30 mas and 10^{-9} beyond 100 mas angular separation.
2. Spectroscopic and polarimetric imaging, should have as well as medium resolution spectroscopy (R 3000) for the spectral characterization of Exo-planet chemistry.
3. The spectral range should be covers the optical to the NIR between 600 and 1650 nm.

If all the requirement will be achieved, EPICS will be able to detect about a several hundred exo-planets (this value have been evaluated by MonteCarlo simulation in [43]). The key to achieving highest imaging contrast and sensitivity from the ground is a superb correction of the dynamic and quasi-static wavefront aberrations introduced by Earth's atmosphere and the telescope/instrument, respectively. For this reason, an Extreme Adaptive Optics system will be implemented in EPICS.

HARMONI HARMONI is a visible and near-infrared (0.47 to 2.45 μm) integral field spectrograph. It provides a range of spatial pixel (spaxel) scales, which permit the user to optimally configure the instrument for a wide range of science programs, from ultra-sensitive to diffraction limited, spatially resolved, physical, chemical and kinematic studies of astrophysical sources.

METIS METIS is a mid-infrared imager and spectrograph. Covering the L, M and N bands, METIS will offer imaging and medium-resolution spectroscopy over the full wavelength range (3-14 μm), and high-resolution integral field spectroscopy in L and M bands (3-5.3 μm). The mid-IR wavelength range is extremely rich in spectral diagnostics, complementary to those found at other wavelengths: emission and absorption lines of virtually all molecules, numerous atoms and ions, and unique solid state features. Other important science cases are:

- Proto-planetary disks and the formation of planets
- Physical and chemical properties of exoplanets
- Formation and history of the solar system
- The growth of supermassive black holes
- Morphologies and dynamics of high-redshift galaxies.

All these science cases rise some characteristics and requirements of the instrument. For example, METIS should be diffraction-limited imaging in L, M and N bands with a field of view of approximately 18" x 18". The imager also includes coronagraphy in L and N bands, a low resolution slit spectrograph (R < 5000) and N-band polarimetry. The instrument consists of two separate units, one for the imager and another for the spectrograph, and is entirely encased in a cryostat to maintain the stable low temperatures required for good performance at mid-infrared wavelengths. To achieve diffraction limited performance, METIS will use adaptive optics correction to compensate for atmospheric turbulence. The instrument will be able to observe with both natural and laser guide stars.

MICADO The *Multi-AO Imaging Camera for Deep Observations* is an Imager and Slit Spectrograph. It has been designed for science cases that needed precision astrometry in order to measure stellar orbits around supermassive black holes in nearby galaxies. or the proper motions of globular clusters that can be used to derive their distance via parallax displacement, separate their stellar populations from field stars, and, by looking for kinematic families, probe the formation and evolution of the Galaxy, or more analyzing the internal kinematics of dwarf spheroidal to derive their anisotropy and mass density profiles. MICADO has been optimized for the external multi-conjugate adaptive optics module MAORY, it is able to image, through a large number of selected wide and narrow-band near infrared filters, a large 53 arcsec field of view at the diffraction limit of the E-ELT. The principal arm of MICADO is a high throughput imaging camera with a single 3mas pixel scale, but there are also another arm that provides a finer 1.5mas pixel scale over a smaller field, and a 4 mas pixel scale for a simple, medium resolution, long-slit spectroscopic capability.

OPTIMOS -DIORAMAS , -EVE OPTIMOS-DIORAMAS is a wide field imager and a low-medium resolution multi-slit spectrograph, it covers a wide 6.8 x 6.8 arcminute field, a large wavelength range of 0.37 to 1.6 μm, with up to about 500 slits observed simultaneously. The science cases that drove the requirements for this instrument have been:the history of galaxy mass assembly and star formation at 1 < z < 6; the detection and study of "first light" galaxies or AGN at z > 6 ; the tomography of the high-redshift Universe to understand the role played by the interplay between galaxies and the intergalactic medium in galaxy formation and evolution processes etc... The instrument layout is organized around four channels, two channels are optimized for the visible from 0.37 to 1 μm, the two other channels are optimized for the NIR from 0.6 to 1.6 μm, cutting off before the thermal background becomes dominant. In addition, high spatial and spectral resolution integral field spectroscopy in a field of $\sim$ 10 $arcsec^2$ could be easily added as the instrument is conceived in such a way that it can host a slicer-based integral field unit. OPTIMOS-EVE is a fiber-fed, optical-to-infrared multi-object spectrograph designed to explore the large field of view provided by the E-ELT at seeing limited conditions. EVE has been designed in order to be able to resolve stellar populations in nearby galaxies, to search for planets in the Galactic bulge and stellar clusters, and in external dwarf galaxies, to tracking the first galaxies and cosmic re-ionization from redshift 5 to 13 and mapping the ionized gas motions at large scales in distant galactic halos. For this reason OPTIMOS-EVE is an instrument designed for the E-ELT Nasmyth focus and provides low-, medium-, and high-resolution spectroscopy (R $\sim$ 5,000 - 30,000) from the ultraviolet to the near-infrared (0.37 to 1.7 mm) for multi-object studies of sources nearby and at cosmological distances.

SIMPLE SIMPLE is an high resolution Near-IR spectrograph. The combination of high spectral resolution and wide spectral coverage in the near-IR, makes SIMPLE an ideal instrument for detection and characterization of exo-planet atmospheres, the early nucleosynthesis and chemical enrichment in the inner Galaxy or to the chemical and dust enrichment of proto-galaxies in the early Universe at the reionization epoch. The concept of the instrument consist of a canonical cross-dispersed echelle spectrometer, whose entrance aperture is a few times the diffraction limit at the longer wavelengths (K band). It has a spectral range that cover from 0,8 to 2,50 μm. Different resolution can be obtained changing the slit width, R=100000 and R=150000 with a sampling respectively of 4 and 2.7 pixel.

ATLAS ATLAS is a generic laser tomographic adaptive optics system for the E-ELT. Based on modular, relatively simple, and yet innovative concepts, it aims at providing diffraction limited images in the near-infrared for close to 100 percent sky coverage. ATLAS uses the six laser guide stars (LGS) provided by the E-ELT laser launch telescope and two natural guide stars (NGS) to sense the wavefront error of the incoming beam by implementing six identical LGS wavefront sensor (WFS) channels and two identical NGS WFS channels. The LGS WFS channels are used to sense the high-order wavefront errors while the NGS WFS channels are used to measure the low order modes. ATLAS can deliver a clear central 30-arcsecond FoV free from optics to the Nasmyth focal stations. An extended FoV of 60 arcseconds, which may be partially vignetted (by the two NGS pick-off arms) is available.

MAORY MAORY is the multi-conjugate adaptive optics module of the European Extremely Large Telescope. It is based on Multi-Conjugate Adaptive Optics (MCAO) to achieve a uniform compensation of the atmospheric turbulence effects over an extended field of view. MCAO uses several deformable mirrors, optically conjugated to different turbulent layers, and several guide stars, to obtain a kind of 3-dimensional mapping of the turbulence. The wavefront correction is achieved by MAORY by means of two post-focal deformable mirrors complementing the ground-layer correction and field stabilization provided by the E-ELT mirrors M4 and M5. Wavefront sensing is based on the use of LGS and NGS, following the choice adopted in other MCAO systems for present and future telescopes. In particular MAORY is designed to compensate the atmospheric turbulence effects for the imaging camera MICADO and for other instruments as the infrared spectrograph SIMPLE. It works in the wavelength range 0.8 - 2.4 μm and provides a corrected image field corresponding to 120 arcsec on sky

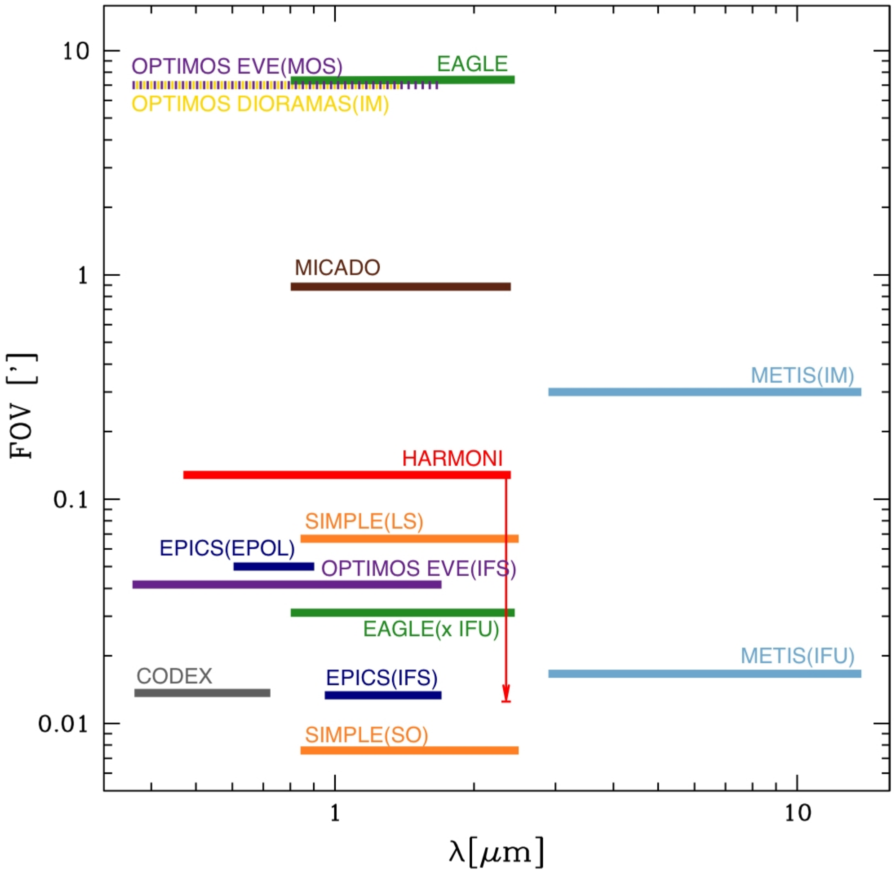

Figure 2.5: Field of view vs. wavelength coverage for the eight E-ELT proposed instruments currently under study

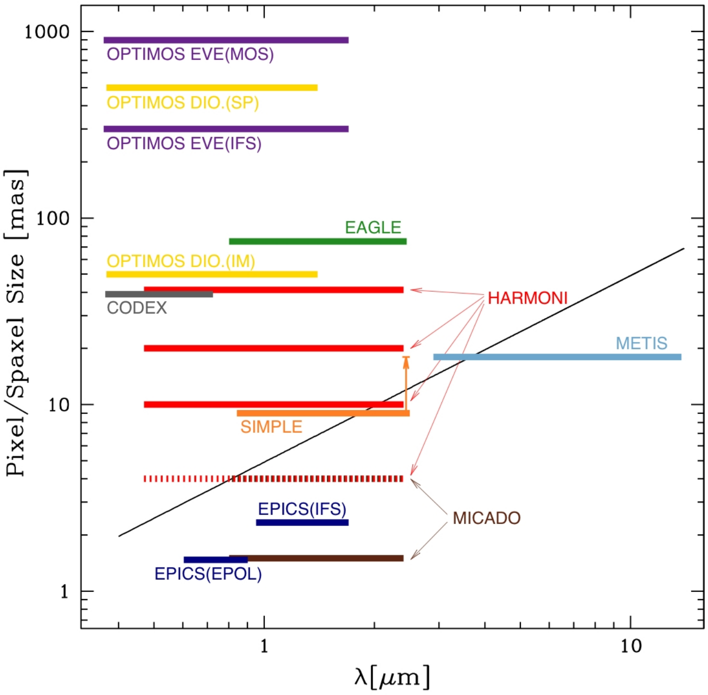

Figure 2.6: Pixel/spaxel size vs. wavelength coverage for the eight E-ELT proposed instruments currently under study. The diagonal black line shows the diffraction limit of the telescope as a function of wavelength.

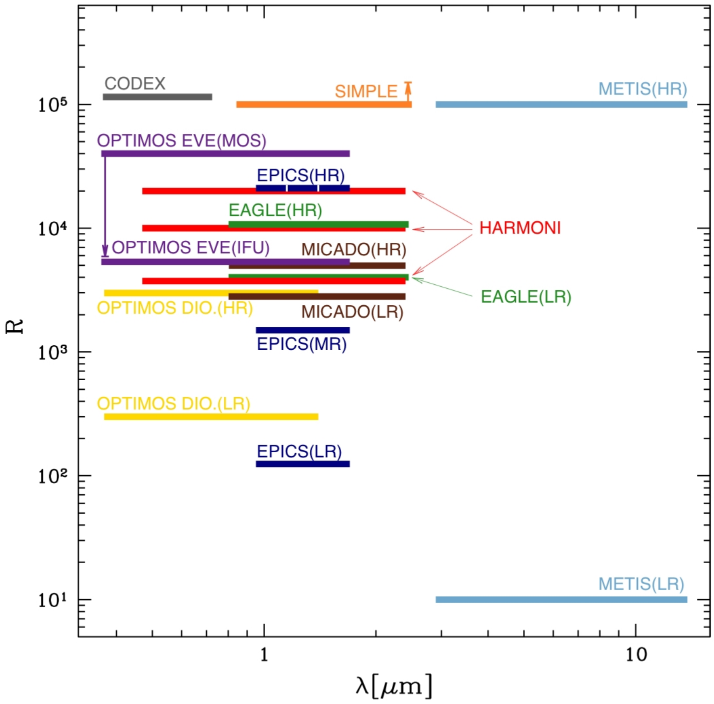

Figure 2.7: Spectral resolution vs. wavelength coverage for the eight E-ELT proposed instruments currently under study. High, medium and low resolution channels are included when available.

Chapter 3

The M4 Adaptive Unite and its Demonstration Prototype

In the preview chapter we have well understood that the E-ELT will be a completely adaptive telescope. Thus, the “core” of the telescope is situated in the Adaptive Relay Unit Tower (ARU - see fig. 3.1).

In the ARU tower are located M3, a 4 meter class active concave mirror, the flat adaptive mirror M4 and the flat (low temporal frequency, up to a few Hz) field stabilization mirror M5. This is the system that entirely corrects all the wavefront deformations. In this chapter we present an overall description of M4 Adaptive Unite (AU) system and of the Demonstration Prototype (DP) with all their sub systems. In figure 3.2 we can see the position of the M4 adaptive unit in the optical design of the telescope.

The main function of the M4 adaptive unit is to correct the aberrations of the wavefront due to: the atmospheric turbulences, the telescope vibrations and deformations and the wind.

In 2007 ESO commissioned two identical studies to industrial firms. The contract include also the production of prototyping parts of the M4 system [32].

The studies are focused on different technologies for the actuation of the mirror and also provide different densities of actuators. The first one use the piezostack actuators technology and the second one use the voice-coil technologies. Both studies are using well demonstrated technologies for adaptive mirrors, in particular the voice-coil actuators is a technologies already established and validated in previous cases like the MMT and the LBT.

This thesis work has been part of studies with voice coil actuators technologies. The principal innovative characteristics of this proposal are:

- *Huge dimension* of the mirror
- *Flat-shape* (easy to make, hardly to measure and test)
- A baseline design with a *segmented mirror*
- *Large number of actuator* to be managed

3.1 The Project Definition

In 2007 a technical proposal for the conceptual design, prototyping, preliminary design of M4 Adaptive Unite for the E-ELT was submitted to ESO. The consortium is

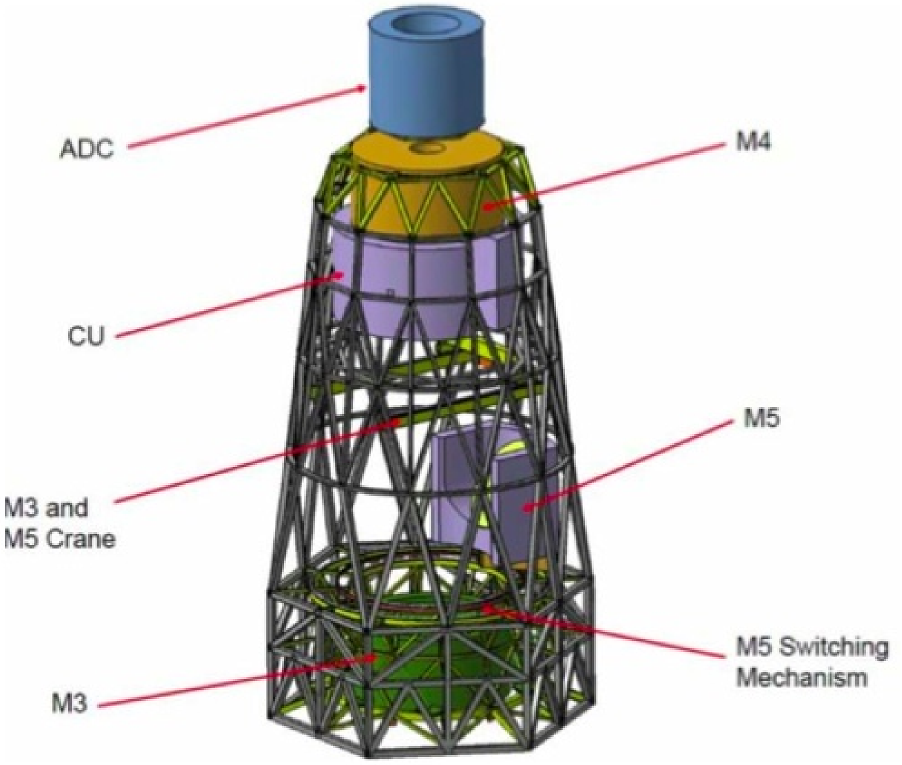

Figure 3.1: The ARU central tower of the E-ELT

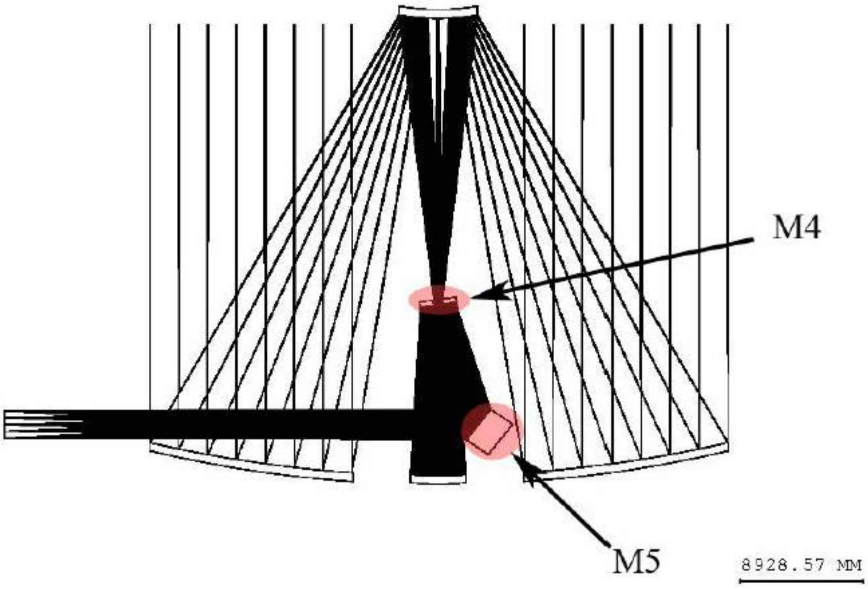

Figure 3.2: M4 AU and M5 evidence

composed by Microgate [11], A.D.S.International [2] and Sagem [15] for the industrial components and INAF - Osservatorio Astronomico di Brera (OAB-INAF) [3] as research institute.

Microgate and ADS companies have a wide experience in the studies of large deformable mirrors, while INAF-OAB has experience in interferometry and metrology sciences and gives his technical support for the design and implementation of the Demonstration Prototype optical testing activity. The work is organized under the control and direction of Microgate acting as prime contractor.

The project is subdivided in four principal classes:

- The Electronics and Control System SoftWare, managed by Microgate
- The Electro-Mechanical subsystem, covered by A.D.S. International
- The Optics design and manufacturing, care of Sagem
- **The Optical Test, managed by INAF-OAB**

The project was divided in four phases:

- Phase 1 (oct 2007 - may 2008) : Analysis of requirements, first concept of M4AU (Straw Man Design) and Detailed design of the Demonstration Prototype
- Phase 2 (may 2008 - jun 2009): M4AU Conceptual Design, Demonstration Prototype manufacturing and preliminary testing
- Phase 3 (jun 2009 - oct 2010): Full test of M4AU Demonstration Prototype
- Phase 4 (jun 2009 - may 2010): M4AU Preliminary Design

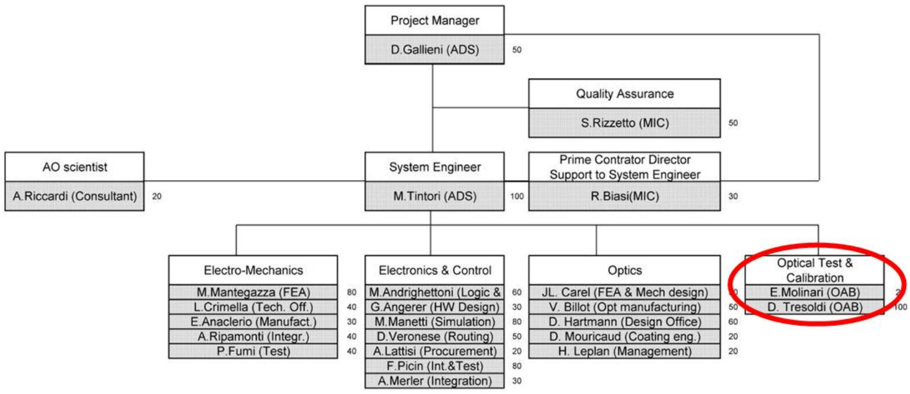

Figure 3.3: Team organization chart

During Phase 1 all the technical specifications and requirements provided by ESO have been analyzed and a *Strawman Design* of the M4 Adaptive Unit and the optical tests were produced. Moreover, all the potentials risks have been identified and alternative technologies and technical solutions have been studied for backup solutions. A detailed design of the Demonstration Prototype has been developed and all the electromechanical and optical tests have been projected, designed (as the design of the optical test bench etc.) and planned.

During Phase 2 the *Strawman Design* of the M4 Adaptive Unit was developed at Conceptual Design level with all the analyses and error budgeting necessary for demonstrating the feasibility of the system and the compliance with the technical specifications. The Test Optical Bench has been designed in detail and the procurement of all components (optical and mechanical) began. The Demonstration Prototype has been manufactured and the preliminary critical tests have been performed.

Phase 3 was the full test phase of the DP.

Phase 4 has led at the Preliminary Design of the M4 Adaptive Unite, thanks to the knowledges learned during the manufacturing and testing of the DP.

Each phase passed a review by ESO experts.

Figure 3.3 shows the Team Organization Chart where my role in the project is explained and the table 3.1 lists all the Work Packages (WP) on which I have dealt with.

Table 3.1: The Work Packages of the M4 Adaptive Unite Project under OAB responsibility

Ph.1	13140	STRAWMAN DESIGN OF M4AU CALIBRATION AND TESTING
	13270	FINAL DESIGN OF DP CALIBRATION AND TESTING
Ph.2	23140	CONCEPTUAL DESIGN OF M4AU CALIBRATION AND TESTING
	24070	DEMONSTRATION PROTOTYPE OPTICAL TEST BENCH PROCUREMENT
	24110	DEMONSTRATION PROTOTYPE OPTICAL TEST BENCH INTEGRATION
Ph.3	35030	DEMONSTRATION PROTOTYPE OPTICAL TEST

WP 13140 This Work Package concern the analysis of the technical specifications and determinations of the tests needed for the characterization and calibration of M4AU, the initial definition of the procedures to perform the tests and the identification of the critical items and definition of a possible pre-prototyping plans.

WP 13270 With more information about the Demonstration Prototype characteristics (shape, dimension etc.) and about the Demonstration Prototype shell (size, material and thickness), it is possible to prepare a detailed opto-mechanical design of the DP calibration and testing optical bench.

WP 23140 With the Phase 1 documentation we proceed to a Conceptual Optomechanical Design of the final M4AU calibration and testing unit.

WP 24070 This Work package concern the procurement and the acceptance (incoming inspection with preliminary test) of all the components (optics and mechanics) of the optical test bench for the Demonstration Prototype. The input is the studies completed during the WP13270.

WP 24110 is the integration and calibration of the optical test bench. At the end of this WP, the optical test bench must be ready to start the test on the DP.

WP 35030 This is the core of the project. The realization of the optical test and the analysis of the results in order to demonstrate that this technology works as simulated and designed.

We have reported an overall view of the project concern the realization of the Adaptive Optics Unit for the E-ELT. Currently all the results have been presented at ESO and accepted. Final decision on which technology will be used for the realization of the Adaptive Unite of the E-ELT, is expected within the end of this year (2011).

In the next section we present in detail the studies and works done.

3.2 Technical Requirements

The Technical Requirements prepared by ESO experts (the Adaptive Optics working group), are the starting point of all the design of M4AU. A document exists that defines and lists all the Technical Specifications of the M4AU [44]. These Technical Specifications establish directly or indirectly the performance, the design, the development and test requirements which apply to the M4, cover furthermore the integration, service and test equipments which are necessary for the optical alignment, the maintenance and testing of the M4 Unit. In this section we refer to the main technical requirements and to the optical performances of the adaptive system.

General Characteristics

1. The M4 Adaptive Mirror (AM) shall compensate in real-time all the high order wavefront distortions due to the atmospheric turbulences and shall compensate the residual tip/tilt due to the telescope vibrations, wind and wavefront errors generated by the atmosphere, remaining after the M5 correction.

2. The M4AU shall perform the addressing of the two Nasmyth foci and shall reflect the optical beam from M3 to M5.

3. The M4AU shall be thermally controlled to limit heat dissipation and thereby prevent turbulence to significantly affect the light beams propagated to the telescope focus.

4. The M4AU shall correct for lateral misalignments of the pupil with a range of $\pm 20mm$ at a bandwidth larger than 1 Hz with a resolution better than $50\mu m$

5. The mechanical tilt correction range shall be $\pm 2arcmin$ with a resolution better than $25arcsecond$

6. The cross coupling between lateral displacements and mechanical tilt shall be: the lateral displacement shall not introduce more than $0.025arcsec$ in tilt while the tilt displacement shall not induce more than $50\mu m$ of lateral displacement

7. The system shall include a Calibration mode.

8. The M4AU shall provid three operational modes:

    - Non Adaptive Optics mode (NAO-mode): the mirror shape shall be maintain the calibration data without any external feedback
    - Field Stabilization Non Adaptive Optics mode (FSNAO-mode): the mirror shall be able to tip and tilt continuously around two perpendicular axes while the shape of the mirror shall maintain the shape of the calibration data
    - Adaptive Optics mode (AO-mode): the M4AU shall be able to implement a set of actuators commands controlling the shape of the mirror surface with a rate up to 1.2 kHz

9. *In the case of segmented geometry, the M4AU shall be able to apply corrections to the segments phasing and guarantee the phasing without any external feedback.*

10. The M4AU shall be able to maintain its optical shape including tip-tilt command without any external real-time feedback and shall maintain the commanded position of the mirror actuators until the next command is received.

Optical Requirements

All the optical requirements are given with the tilt removed.

11. When the system is fully powered and in NAO-mode, the root mean square (rms) of the Wavefront Error (WFE) shall be $< 250nm$ with only the internal calibration.

12. When the system is fully powered and in FSNAO-mode, the root mean square (rms) of the Wavefront Error (WFE) shall be $< 250nm$ with only the internal calibration.

13. When the system is fully powered and in AO-mode, without atmospheric turbulences, the root mean square (rms) of the Wavefront Error (WFE) shall be $< 15nm$ for scales smaller than twice inter-actuator spacing and $< 20nm$ for scales larger than twice the inter-actuator spacing

14. The M4AM shall be able to correct for telescope optical errors with the following characteristics:

    - The lowest 20 Zernike modes (excluding piston, tip and tilt) in the Noll Classification shall be corrected
    - The M4AU shall be able to correct a maximum PV wavefront error of 10 micron
    - The M4AU shall be able to correct maximum WFE step amplitude (PTV) of 3 micron in a range of ±10 micron
    - In addition, the M4AU shall be able to correct for telescope motion/tracking errors and atmospheric image motion in tip and tilt described by the Power Spectral Density (PSD) provided in figure 3.4
    - In addition, the M4AU shall be able to correct for the telescope focus error due to wind effects which characteristics are described by the power spectral density provided in figure 3.5

15. The M4AU residual wavefront error with turbulence shall be <145 nm rms (goal: 110 nm rms) under the median atmospheric conditions.

16. The stroke requested to internally maintain the M4AM surface to the required shape due to environmental operational conditions and operational loads shall not be larger than 10% of the total actuator stroke (in force or in position).

3.3 System Overview

The principal innovative (and thus critical) characteristics for an Adaptive Optics System are:

- The huge dimension of M4AM: $\oslash 2.6m$.

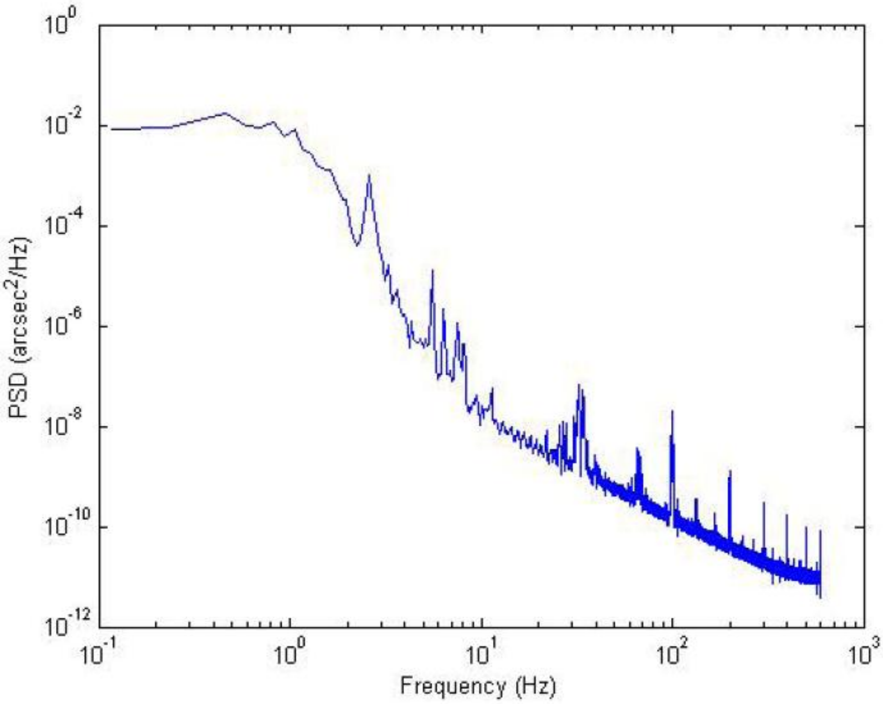

Figure 3.4: PSD of the tip/tilt due to the atmosphere with outer scale of turbulence $L_0 = 100m$, Seeing at 0.5 μm = 2.5 arcsec, Correlation Time τ_0 = 0.002 sec

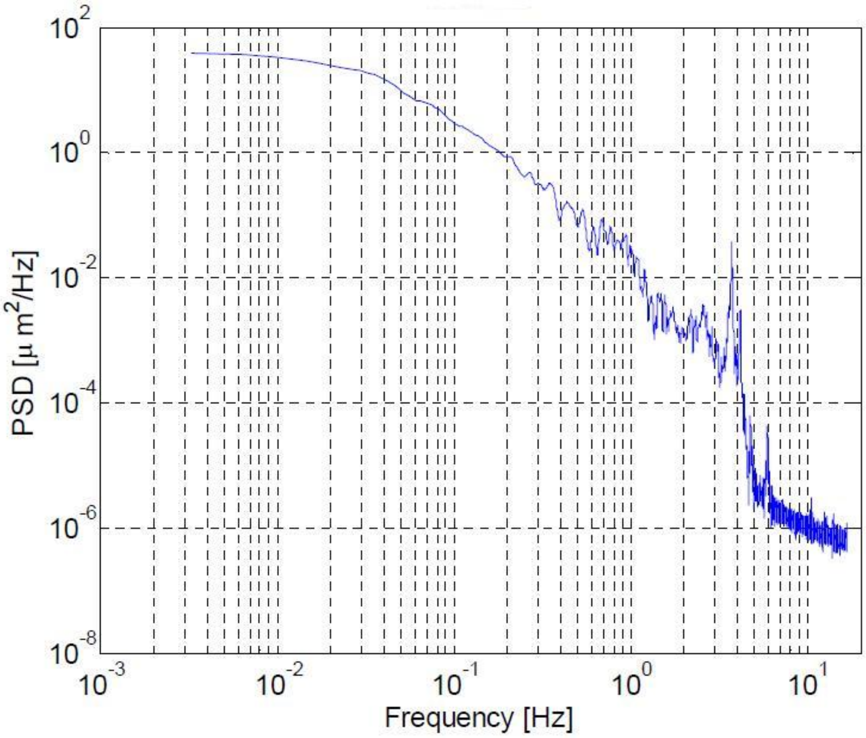

Figure 3.5: PSD of the defocus due to the wind effects

- M4 is the first adaptive mirror with a flat shape.
- M4 is a segmented mirror.

The M4 AU is composed by different subsystems: the M4 Adaptive Mirror (M4AM), the M4 Positioning System (M4PS), the M4 Mounting Structure (M4MS), the M4 Control System (M4CS).

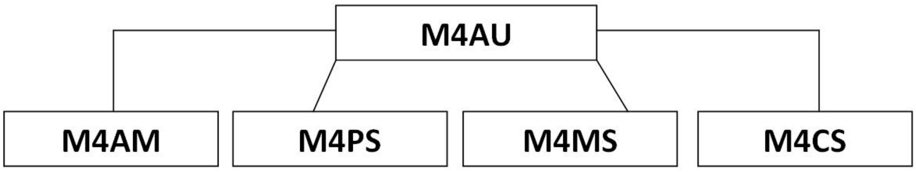

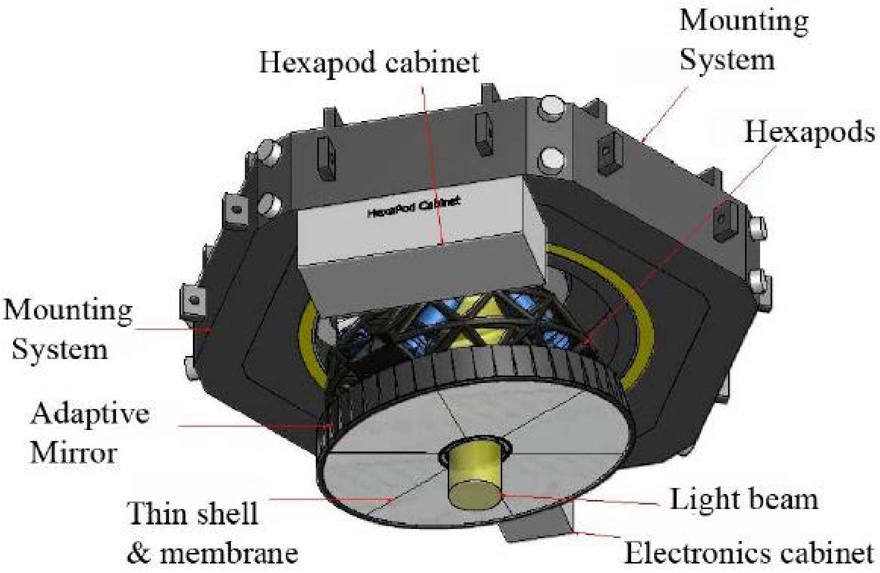

Figure 3.6: M4 Adaptive Unite Layout

The diameter of the deformable mirror is 2.6 meters. Due to the large dimension and the small thickness of the mirror ($< 2mm$), the baseline solution foreseen is a segmented solution. The mirror design is composed by six flat petals. In this way each segment has the size comparable to already produced thin shells for the deformable secondary mirrors for the Very Large Telescope [45]. The monolithic solution has been studied in parallel and a monolithic shell prototype 2mm thick is now under manufacturing at SAGEM.

The number of actuators is determined from different factors. Firstly from the requirement 13 of the previous section, with the PSD and the atmospheric model, we can determine the number of modes that must be corrected in order to meet the requirement. Moreover needs to take into account the minimum actuators spacing set by the interaction between adjacent permanent magnets and the specified max allowed power dissipation. The best compromise between these parameters was found in the number of about more than 6000 actuators.

The pattern of arrangement of the actuators selected, is a triangular pattern and the actuators separation is 31,5 mm.

M4AM consist of: • The flat mirror composed by six Zerodur thin shells. • The reference-body (or Back-plate), providing a stable reference surface for the mirrors and holding all the components of the Adaptive Optics system. • The actuators bricks holding the electronics components and the actuators for the Adaptive optics and keeping them in contact with the cooling system. • The external membrane holding the mirror in its plane.	**M4PS** consist of: • The Hexapod, a positioning system with six linear actuators connected to the reference body, that move the adaptive mirror in x-y direction and tilt it around *x* and *y* axis. • The Rotating flange holding the Hexapod and the optics, that give the rotation along *z*-axis. • The Nasmyth switching system
M4MS is a structure with the shape of a ring, with a set of adjustable flanges for its correct alignment which links the M4AU to the telescope interfaces.	**M4CS** is the control electronics dedicated to digital control of the M4AM, placed far away from the deformable unit in a range of 300-500m.

The actuator stroke is given as a sum of various terms such as the atmospheric turbulence contribution evaluated with numerical simulation, the telescope motion/tracking, the defocus due to the wind, environmental/operational loads and cophasing issues.

The required actuator stroke, accounting for all the terms, has been evaluated to be $110\mu m$.

At the moment the baseline design of the backplate is made in Carbon Fiber Composite. In front of the reference body there are glass inserts, metal coated, (the armatures of the capacitive sensors), and the back of the reference body is made a honeycomb design hosting the bricks which in turns host the actuators voice coil, the electronic boards and the cooling system.

Each bricks host 36 actuators.

The entire brick is considered as a Line Replaceable Unit(LRU) i.e. a subsystem which can be replaced directly on the telescope from the back side of the M4AM, without the need to remove the mirror shell. This concept improves significantly the maintenance aspects of the unit. In figure 3.7 we can see the layout of the brick and a prototype with only 21 actuators. The actuators voice coil are composed by a permanent magnet, glued on the back of the mirror shell, a coil motor winded up on an aluminum cold finger mounted on the backplate bricks and the capacitive sensors, glued on the backplate (see 3.8 for the layout of the voice coil actuator). The displacement of the actuator is proportional to the intensity of the magnetic field and the capacitive sensors measure the gap value with highest accuracy (accessible only after the optical calibration), providing the information about the mirror shape in real time.

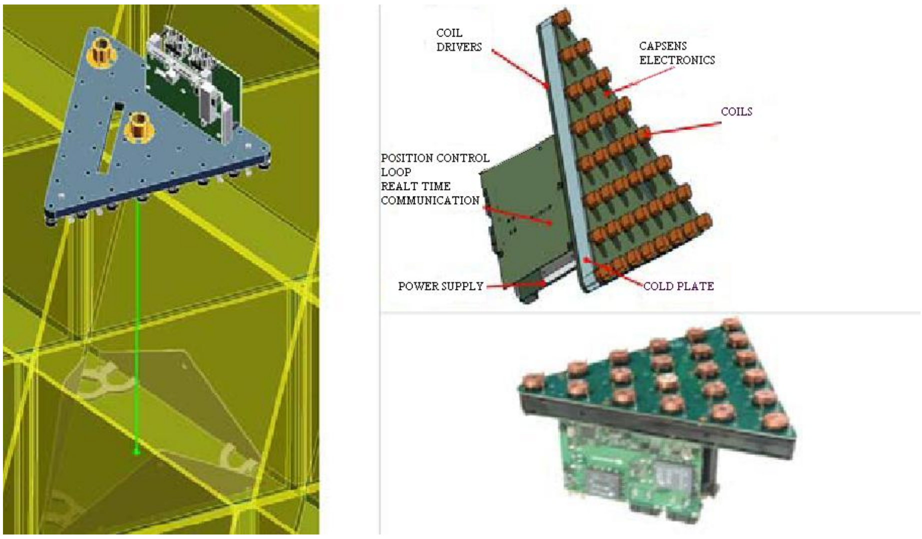

Figure 3.7: Actuators brick layout (top right) and its mounting concept into the reference body (left). Brick prototype with 21 actuators.

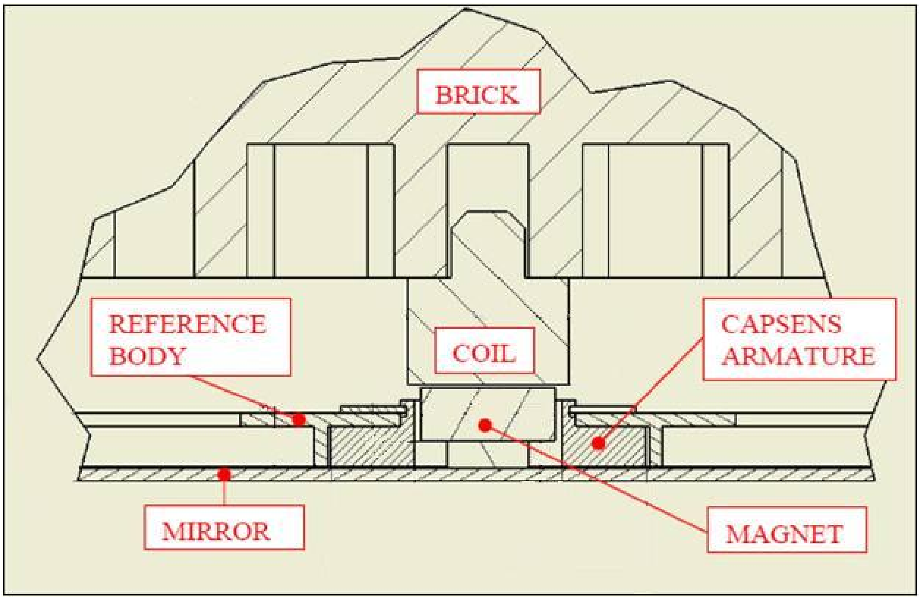

Figure 3.8: The voice coil actuators concept

M4 Positioning and Control System

The positioning system is composed by a hexapod (in fig 3.9 wee can see an example of hexapod produced by ADS International) with six linear actuators, twelve flexible frictionless joints and mobile flanges connecting the legs to the reference body that provides for lateral displacements and tilts, while the Nasmyth switching system is a contact ball bearing driven by a gear wheel and two brushless motors. In order to limit the hexapod stroke, in particular the rotation of the end joints of the actuators in order to achieve the requirements. For this reason just part of the possible motions are actuated by the hexapod.

The Control electronics of M4AU is divided in two subsystems, the electronics of

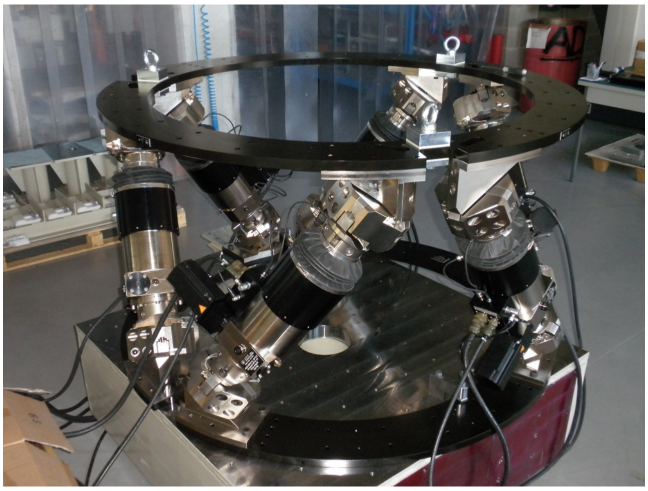

Figure 3.9: Hexapod

the brick, mount on board of M4AM and the Control System electronics placed away from M4AM. The electronics placed close to the M4 unit is limited to the minimum required for the local control and diagnostic, including the capacitive sensor signal conditioning and analog to digital conversion as well as the coil drives and the respective digital to analog conversion. This minimizes the dissipation at the level of the M4 unit; in particular power dissipation due to the parallel processing real time computer is located remotely.

The global control tasks are implemented on a separate unit placed in a control room away from the M4 unit location and communicating with it by means of just seven fiber optic pairs. Global signals are managed by the Distribution Box which also distributes the power lines and performs the hardware safety checks. All bricks are then connected to a unique digital processing electronics, the M4 Control System, based on a large cluster of Digital Signal Processor (DSP) boards.

The main task of such electronics is performing all real-time global computations necessary to guarantee the system dynamic performances and providing a suitable real time communication line to the M4AU. It also provides the high speed data interface to the Real Time Control unit and the Housekeeping interface to the telescope control system. In order to validate this design, a demonstration prototype with the same key sub-systems as the final mirror, as actuator geometry, bricks, cooling plant, backstructure design, was realized and tested. In the next section I present the demonstration prototype (DP).

3.4 The Demonstration Prototype

Demonstration Prototype (DP) has been designed and built to be fully representative of the M4AM. The DP mounts the technology of the voice coil actuators with the same design of the M4AM. The actuator bricks, with all the electronics and all opto-mechanics components are mounted inside the reference structure, as in the final unit.

The cooling plant has the same design of the final unit, the design of the bricks and of their interfaces are identical to the one of M4AU. In this way, the DP is a “test bench” for the M4 final unit.

Its objective is to experimentally demonstrate the performance of the M4 adaptive mirror design with voice coil actuators and 2mm thickness thin shell.

Testing the DP, in fact, the real perfomances of the system have been verified.

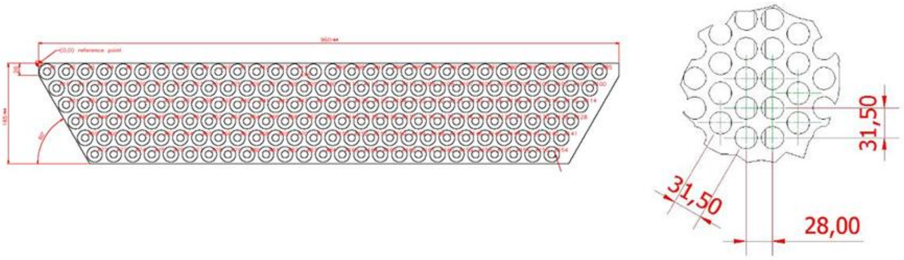

Figure 3.10: DP shell geometry and Actuators DP pattern

Furthermore, have been checked whether the specific requirements assigned has been reached and it was possible identifying eventual critical or risky points.

In particular, the DP is composed by two shells in order to validate the segmented solution proposed and to verify the ability to co-phase the shells and to maintain the phasing. It has been possible to test the edge effect on the fitting error and the control issues related to the edge actuators.

The only huge difference with the final unit is the dimension of the DP. While the diameter of the M4AM is of 2.6m, the long part of the DP measuring only about 96cm. This make it impossible to test the deformations due to their own dead weight or the eigen modes involving an overall bending. In fact, for example, the PtV of deformations under weight is in the order of some microns for the M4 reference body, while for the DP it is always below 0.2 micron.

The dimension of the DP has been chosen as compromise between cost and representativity of the system. With this dimension the DP wants to be a “cut” of the final M4AM unit taken along one of the radius separating two segments.

Technical Characteristics

The Demonstration Prototype is composed by the following subsystem:

- The Zerodur thin shells
- The backplate with the cooling plant
- The actuator bricks mounted on the backplate
- The electronics hosted on the cooled bricks just behind the backplate
- The control electronics dedicated to digital control, placed far away from the deformable unit in a range of 300-500m

Moreover the DP has the same triangular actuators pattern, as for the M4AM (see 3.10) The final dimensions of the DP are: 960x330x250mm. The inter-petal gap, i.e. the distance between two adjacent shells, is 1mm. The number of actuators is 165 for each shell (total number of actuators: 330)

A particularly delicate issue of the system is the membrane that holds the shell and prevents it from slipping horizontally. See the figure 3.12 for the layout of the shell interface.

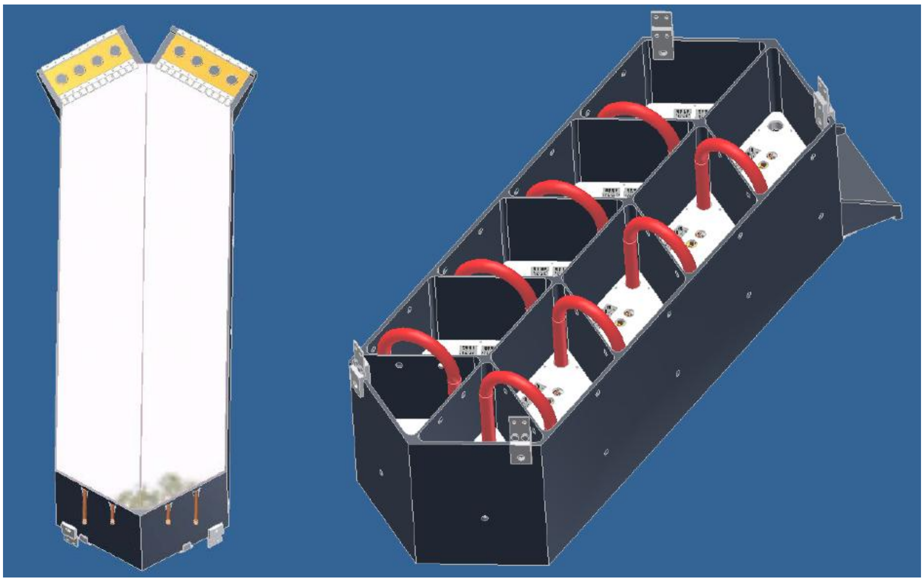

Figure 3.11: Demonstration Prototype layout

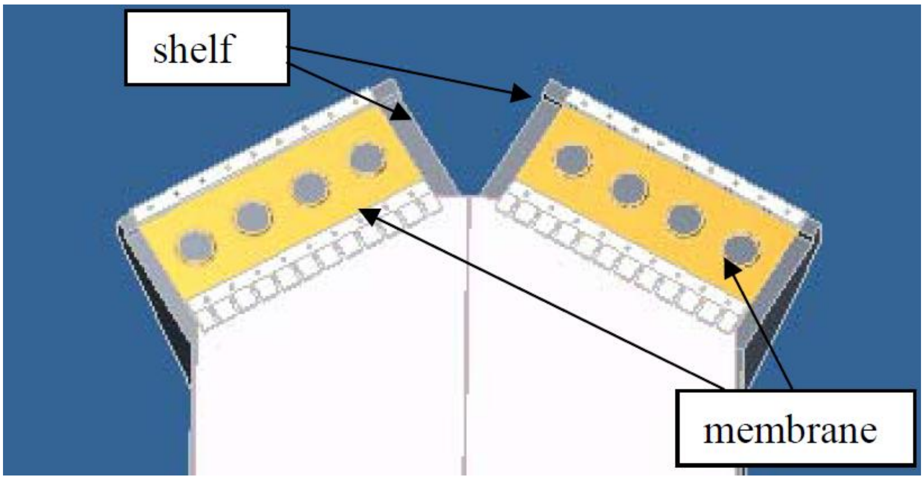

Figure 3.12: Shells interfaces

Chapter 4

Demonstration Prototype under Optical Tests

In order to validate the proposed design of the E-ELT Adaptive Unit, many different functional tests have been performed on the Demonstration Prototype, including mechanical, electro-mechanical and optical tests. In this chapter we describe only optical tests.

The optical tests have different goals.

- Optically calibrate the capacitive sensors in order to correlate the actuator stroke and the displacement effectively performed.
- Acquire Modal and Zonal Feed Forward Matrices (see section 5.1 for more detail).
- Check the ability to control and maintain the flattening of the shells.
- Measure differential piston and tilt between the two shells.
- Confirm the ability of the adaptive system to deform the shell in the desired way.
- Check the stability of calibrations in time and temperature.

All these tasks come from the requirements list in 3.2.

Summarizing this chapter:

Section 4.1 describes laboratory equipments installed at the INAF Astronomical Observatory of Brera and the required hardware and software tools developed for this activity.

Section 4.2 describes the development of the optical tests derived from requirement analysis. It explains the selection of the defined configurations. Three different approaches have been found: Stitching Interferometric System (SIS, **Section 4.2.2**), a system that scans the whole surface of the DP and reconstruct, by software, the full shape of the mirror shells; Piston Sensor Unit (PSU, **Section 4.2.3**), to measure and remove the differential piston between the two shells, by using the diffractive properties of light; Ritchey Common Test (RCT, **Section 4.2.4**), to test the full aperture. The map of the whole shell can be retrieved in a single shot, avoiding uncertainties due to thermal and mechanical drifts of the actuators or the optical bench, or linked to air turbulence.

Section 4.2.5 describes the procurement of the optical and mechanical components of the system, their preliminary acceptance in the lab, and their integration on the optical bench.

Section 4.2.6 reports the self-calibration of the three proposed configurations. The calibration of the SIS consists of the removal of the cavity errors, due to manufacturing of the flat mirrors and their misalignment. A spatial calibration has been performed in order to avoid mismatch between adjacent maps. The PSU has been tested with the help of a differential piston simulator. Finally, calibration of the RCT setup has been done by acquiring the wavefront error of the cavity. Moreover, stability tests have been carried out to check environmental drifts of the measuring system.

4.1 Laboratory Equipments

All optical tests have been performed in the Merate optical laboratories installed at the INAF- Astronomical Observatory of Brera. The OAB/Merate has provided the test laboratory equipped with a Fizeau interferometer (Zygo GPI XP, 102 mm beam, 640x480 detector). New tools have been acquired in order to be able to perform required measurements, as derived from requirements of the system under test.

This lab has been equipped with:

- a crane, in order to be able to move the DP structure and all the mechanical and optical heavy components
- a large (3x1,5) m optical bench provided with damping systems to isolate from ground vibrations

Figure 4.1: Optical table in the OAB/Merate laboratory.

- a new control software for the interferometer, to fully automate the SIS image acquisition.

4.2 The Design of the Optical Tests

The ability to test and measure the shape and accuracy of an optical component is of the utmost importance during the realization of the component itself.

Optical tests will be devoted to map the shape and flatness of the DP. The requirements to achieve are: WFE (rms) <15 nm for scales smaller than twice inter-actuator spacing and <20 nm for larger scales. Moreover, these tests will be used to calibrate the flattening commands of the actuators and their stability.

4.2.1 Fizeau interferometry

One of the most sensitive and accurate methods to investigate optical surfaces is by *interferometry* (see [42]). The Fizeau interferometer is based onto a *Phase Shifting* technique. Figure 4.2 shows a schematic drawing of the system.

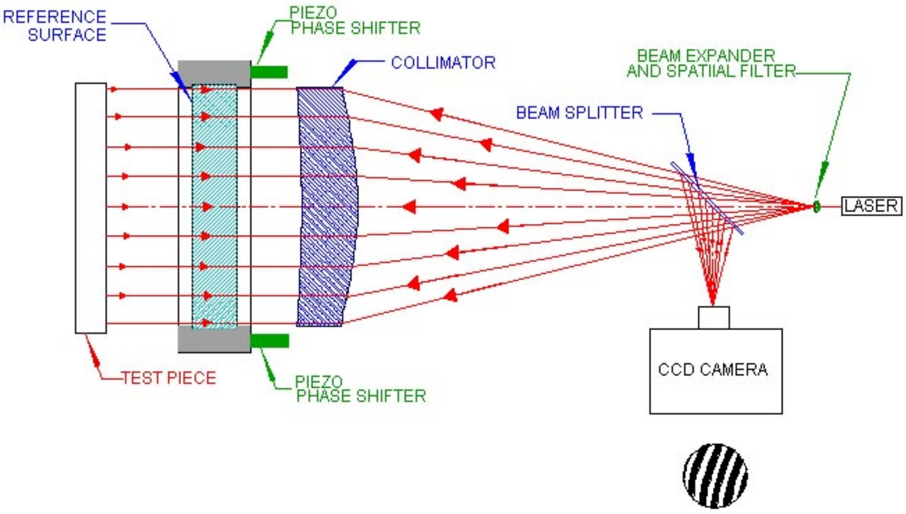

Figure 4.2: Fizeau Phase Shifting interferometer sketch.

The laser beam passes through a pinhole, acting as spatial filter. The diverging beam is then collimated by a lens, and it illuminates the flat high-quality window, acting as transmission reference surface. The reflected light is the*reference beam*, while the transmitted one is the *test beam*, that will illuminate the surface under test and come back into the instrument. These two beams interfere together creating interference fringes. The region between the reference surface and the surface of the test piece is called the *cavity*.

In phase shifting interferometry, a piezo-electric transducer tilt the reference surface by very small steps, introducing a phase difference between different measurements. A frame grabber records interferograms for following software analysis.

4.2.2 Stitching Interferometric Setup

The stitching interferometer samples the DP surface with smaller sub-apertures that will be stitched together, based onto analysis of the overlapping regions ([35], [18]).

Stitching technique has been applied on spherical and aspherical surfaces, asking for quite complex data handling. Being a *flat* mirror, the DP will required a much

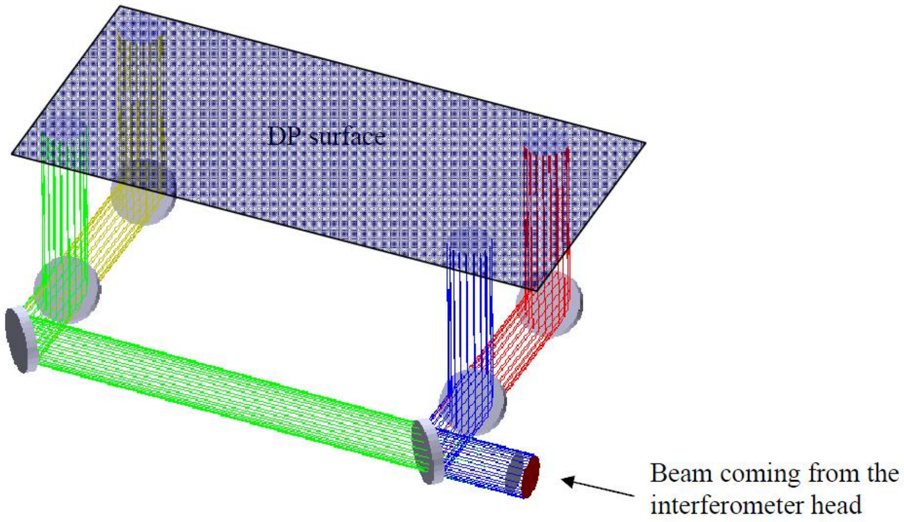

Figure 4.3: Optical layout of the SIS in four different positions of the beam.

simpler system, working with collimated beams. Misplacement along the optical axis can be neglected due to inherent insensitivity of the single measurement steps.

The system consists of flat mirrors mounted on XY rail stages that allows moving the test beam onto different positions over the DP area. The table 4.1 summarizes the performance of our SIS setup.

Table 4.1: SIS performance and characteristics

Area to be tested	1 x 0,4 m
Repeatability	3 nm (2σ)
Spatial Resolution	0,4 mm/pix
Capture Range	$25\mu m$
Sensitivity	<5 nm

Optical layout and mechanical components

The optical layout of this system is very simple: after the transmission reference flat window, mounted on the interferometer, with an accuracy higher than $1/20\lambda$ (PtV), a 10 cm collimated beam is deflected twice, each time at 90 degrees, by two flat precision mirrors, impinging onto the DP surface. Figure 4.3 shows the optical layout with four different positions of the scanning beam.

The first folding mirror (FM1) can be positioned with an angle of 45 deg with respect to the XY plane (see Figure 4.6). The second one will be at 45 deg in the YZ plane. Mirror FM1 is mounted on an optical cell assembly with fine kinematics movements. The second mirror (FM2) will be mounted onto a motorized tip/tilt stage to fine align the interferometric cavity in a remote mode.

The motion of the mirrors of the stitching configuration will be performed via two motorized linear stages. The first one is fixed to the optical bench and its sled runs (X direction) parallel to the main direction of the collimated Zygo beam. On the sled of this stage is fixed the other stage that runs orthogonal to the first one (Y direction).

The sampling beam will have a diameter of 102 mm. We must cover a surface of about $0.4m^2$. In the left-side of figure 4.4 the footprint on the DP is shown (blue filled

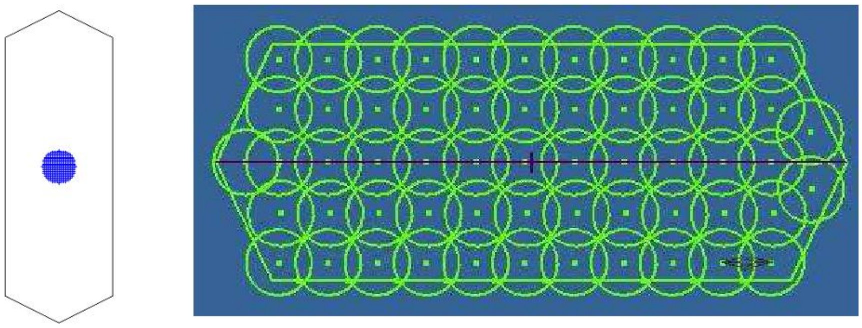

Figure 4.4: The footprint onto the DP surface (left) and the sub-aperture (right)

circle). To allow a proper reconstruction of the overall surface under test, each sub-aperture needs to be overlapped, giving about 60 interferometric maps as shown in the right-side of same figure.

DP surface must be measured with an accuracy of some tens nm rms. Then, the SIS must not introduce larger errors. Any misalignment in decentering of flat mirrors is quite forgiven, while wrong tilts can cause vignetting. Then, the main WFE sources will be surface errors of the flat mirrors. We built an error budget for these flat mirrors. We defined the overall budget to be about $1/50\lambda$, i.e. **12 nm rms**. The table 4.2 reports the error budget for this setup.

Table 4.2: SIS Error Budget

Contributor	**WFE RMS** nm
Transmission flat (measured)	3
First flat mirror	8
Second flat mirror	8
TOT (RSS)	12

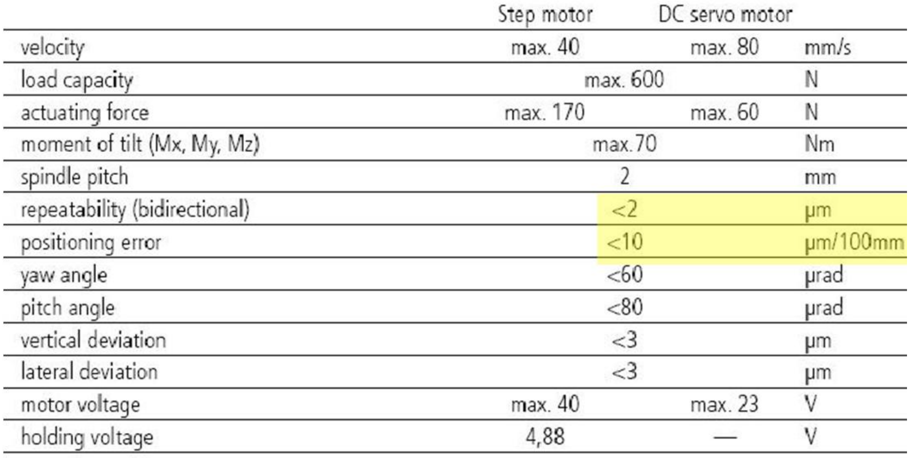

	Step motor	DC servo motor	
velocity	max. 40	max. 80	mm/s
load capacity	max. 600		N
actuating force	max. 170	max. 60	N
moment of tilt (Mx, My, Mz)	max.70		Nm
spindle pitch	2		mm
repeatability (bidirectional)	<2		µm
positioning error	<10		µm/100mm
yaw angle	<60		µrad
pitch angle	<80		µrad
vertical deviation	<3		µm
lateral deviation	<3		µm
motor voltage	max. 40	max. 23	V
holding voltage	4,88	—	V

Figure 4.5: Linear Stage Technical Data

Including the double pass and the 45 deg incidence angle onto the folding mirrors (projection factor = $cos(45°)$), they require a WFE of 8 nm, or about 4 nm of surface error (RMS). This means that we need flat mirrors with a surface accuracy of $1/150\lambda$(rms). Assuming a factor 1:5 (empirical) between RMS and PtV errors, typical for many standard flat surfaces, off the shelf optics having $1/30\lambda$ (PtV) accuracy have been selected.

Moreover, in interferometry it is always desirable to obtain fringes of the highest possible contrast in order to reduce noise. The contrast seen in an interferogram is dependent on the relative light intensity of the reflected reference and test beams. The reflection from the reference surface is dependent upon the reflective coating (or lack of a coating). Our transmission flat reflects about 4% of the light back into the interferometer. So the test beam should reflect between 1% and 40% of light in order to have an acceptable fringe contrast. The DP coating at $\lambda = 633nm$ reflects about the 90%. In the interferometric cavity the light is reflected from two mirrors in double–pass for a total of five reflections. So the two mirrors must been coated with a semi-reflective coating, i.e. with a reflectance between 40% and 60%.

Also important is the repeatability of the positioning system. We have selected a positioning system that allowed eliminating the need of fiducial targets placed onto the surface under test. The linear stages have been chosen with technical characteristic matching those requirements, as seen in figure 4.5. In the next figure we can see some layout and the final unit.

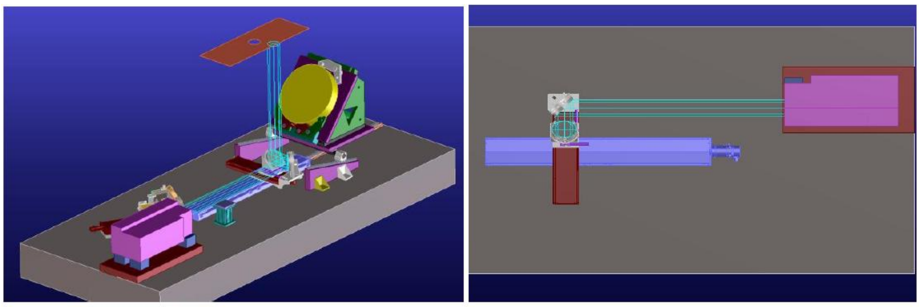

Figure 4.6: SIS optomechanical layout. The collimated beam hits two folding mirrors, mounted on linear stages, to scan the DP surface area. Left panel: 3D cad layout, Right panel: view from above, showing only interferometer, stages and light beams.

The Automation and the Stitching Software

In order to have the whole surface map of the DP, it is necessary to take about 60 sub images stitched a posteriori. The Automation Software is a sub package of the Stitching Software (SISw). The SISw is composed by two principal sub packages, the first concerns the automation of the acquisition, that allows us to take a complete scan of the whole DP surface by a single command, and the second part which processes each image and then stitches them together by returning the wavefront map of the entire surface of the DP. All the packages has been developed under IDL language.

Linear stages are controlled, via USB port, within the same PC that controls the interferometer. A custom IDL script allows to interface with the motorized control system. To interface with the interferometer, a new control and post-process SW has been acquired (ESDI IntelliWave), that can be controlled by a further script, under IDL. The full automation of the acquisition procedure has been codified as a command list of different positions, at which interferograms are stored.

The general SW architecture of the SIS software is shown in figure 4.8. In short, the software manages the movement of the stages, carrying the mirrors in specific positions. Then “order” to interferometer to capture a wavefront map.

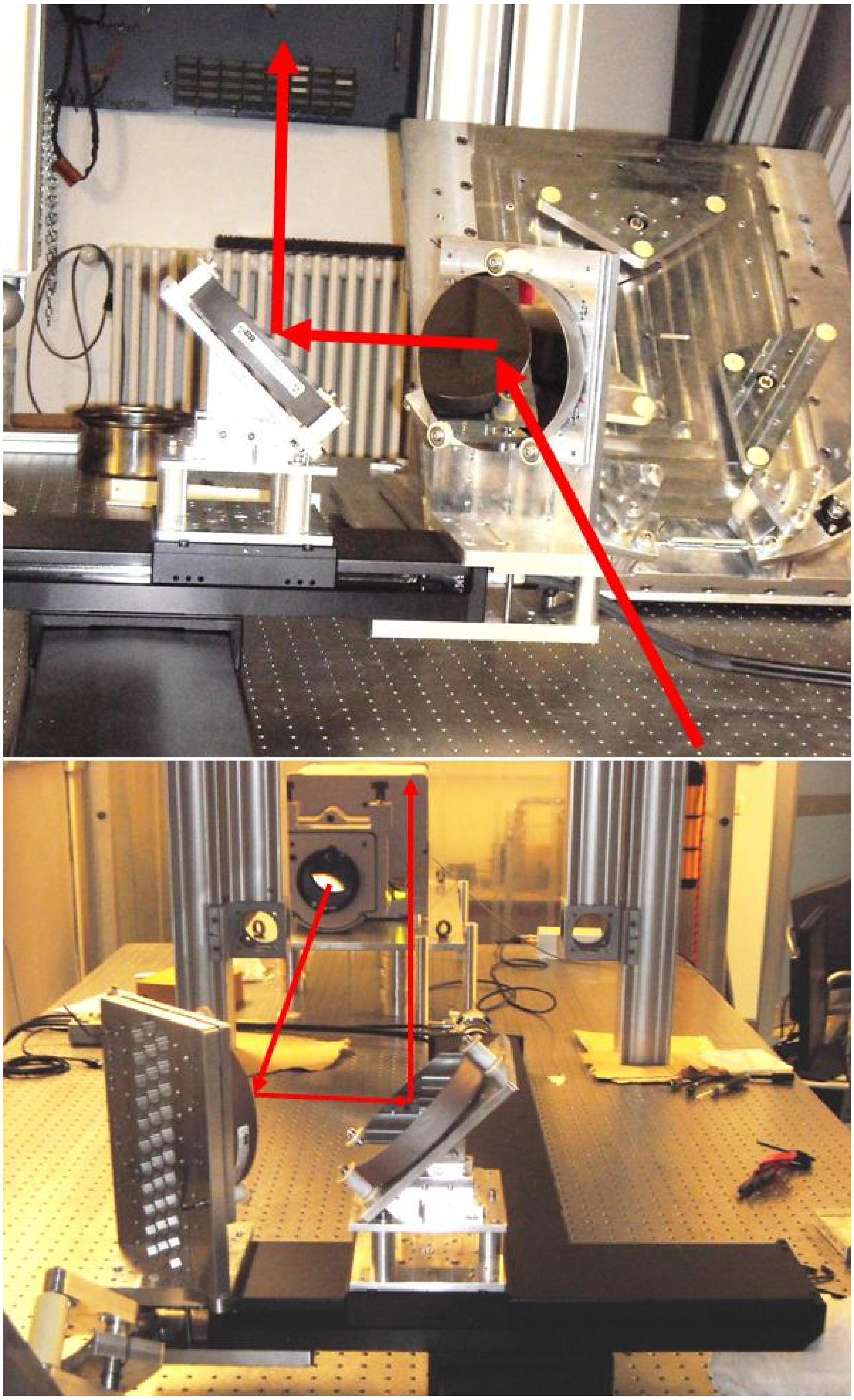

Figure 4.7: SIS integrated

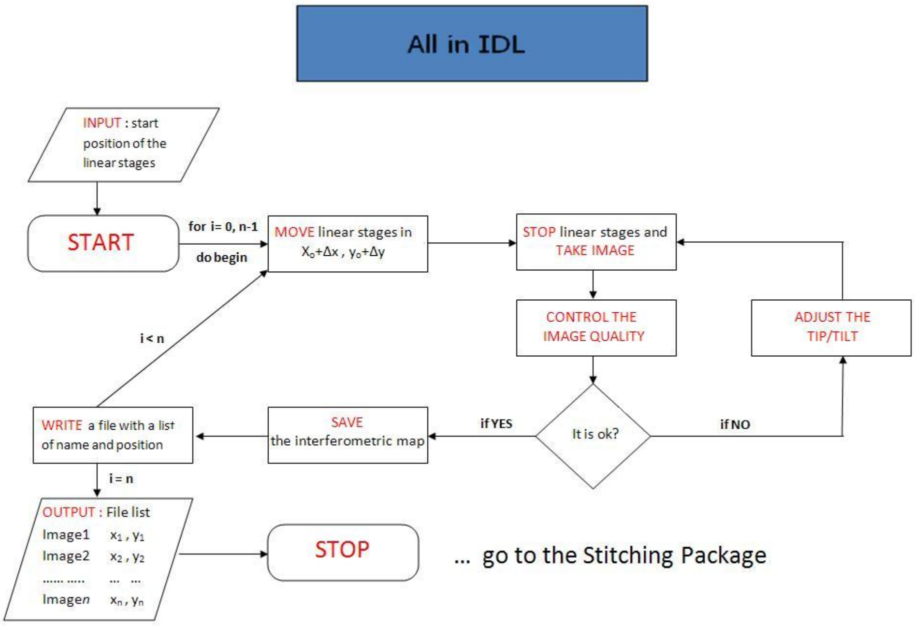

Figure 4.8: Flux diagram of the SIS automation software

When all the surface has been scanned, all the images are stored in a specific folder with together the list file, called `list.txt`. The SIS_SW draws on this folder and at first opens and reads the `list.txt` file.

After calibration of the positioning system, reference points of each image was taken from the encoder readout of the rail stages. A circular mask is applied by software to each image, in order to remove edge effects. The software builds a large array that can contain the whole area (i.e. all the image stitched) and begins to stick the pieces of the puzzle taking one by one, taking the coordinates of each image x_i, y_i in the list file. In the overlapped region, any differential tilt coming from small misalignments of the scanning system, is computed and removed from the second image. Then the two images are coadded, taking the average value in the overlapped region. The result is used in the next step of the stitching process. Some test and calibration for development of SIS_SW are described in section 4.2.6

4.2.3 Piston Sensing Unit

To demonstrate the ability of the system to phase different shells is one of the crucial points of our optical tests. Indeed, the design of the final system is strongly dependent on the co-phasing ability of the system.

Differential piston between adjacent segments of the optical shell mirror can be measured by mean of an multi-wavelength interferometer. In our current laboratory setup, based onto a single-wavelength interferometer, the differential piston cannot be retrieved. If the differential piston size is an exact multiple of $\lambda/2$, the interferometer will measure no differential piston at all. So, it is necessary to remove this ambiguity. To sense the differential piston between adjacent shells, a new device was developed based onto the analysis of the diffraction pattern produced by the differential piston itself, when illuminated by a collimated sample beam. The working principle of this devise is the following. A collimated beam of monochromatic light with wavelength λ, limited by a rectangular aperture of width *a*, produces a diffraction pattern described by the welll-known Fraunhofer diffraction formula:

$$I(\theta) = I_0 \frac{(sin\theta)^2}{(\theta)^2}$$

where θ is the angle in radians with respect to the aperture normal. If a phase difference α is introduced in half of the beam, the intensity profile is described by the following formula:

$$I(\theta, \alpha) = I_0 \frac{[sin(\theta + \alpha) - sin(\alpha)]^2}{\theta^2}$$

where α is the phase shift. The normalized diffraction patterns are plotted in the figure 4.9 in case of 4 different phase shifts: 0, λ/6, λ/3 and λ/2. As explained in [57], the expected accuracy of phasing is of the order of a few nm, under enough signal–to–noise ratio and good spatial sampling. To resolve the π phase ambiguity, also called *"linear range"*, two different techniques, one based on the coherence length and one on the multi-lambda analysis, can be applied.

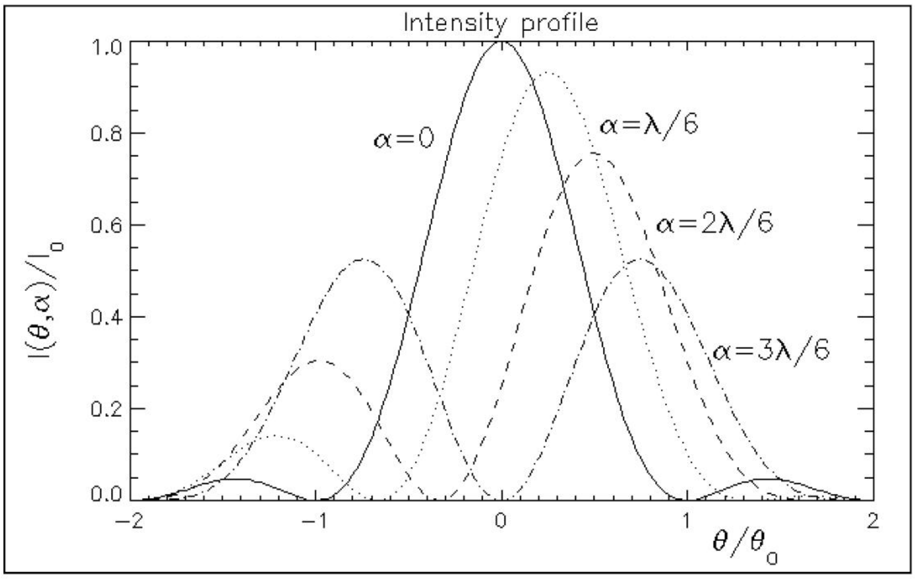

Figure 4.9: Diffraction patterns in presence of a phase difference α. The abscissa coordinate is normalized to $\theta_0 = \lambda/a$

Coherence Technique. The diffraction signal can be seen only if the phase difference introduced in the beam is less than the coherence length of the light used. If not, there is not anymore interference between the two sections of the beam and the resulting intensity pattern is a simple superposition of the intensity patterns produced by one single section. It is possible to define and compute a "coherence parameter" which indicates if and where the piston difference is within the coherence region. By means of this technique and using sources with different coherence lengths (e.g., different filter bandwidths), it has been possible to correct the piston error from an initial values in the order ot $\sim 10\mu m$ down to some 10 nm ([34], [14]).

Multi-Lambda Technique. In alternative or complementary to the coherence-length technique, it is possible to correct large piston error ($> \lambda/2$) using different (quasi) monochromatic wavelengths. This technique is described in [41]. The piston step p is measured at different wavelengths λ_1, λ_2, .. λ_n, giving the values

$p_1, p_2, .. \, p_n$ with some error $\epsilon_1, \epsilon_2, .. \, \epsilon_n$. At each wavelength λ_i the real piston step is then known apart from an ambiguity of λ_i:

$$p = p_i \pm \epsilon_i + k\lambda_i$$

with k ∈ Z, i=1, 2 .. n. If the wavelengths are properly chosen, the true piston can be computed from the measurements. As an example, lets take 3 wavelengths λ_1, λ_2, λ_3 and letś assume that the values measured are p_1, p_2, p_3 respectively. We can graphically represent the results in the plot in figure 4.10.

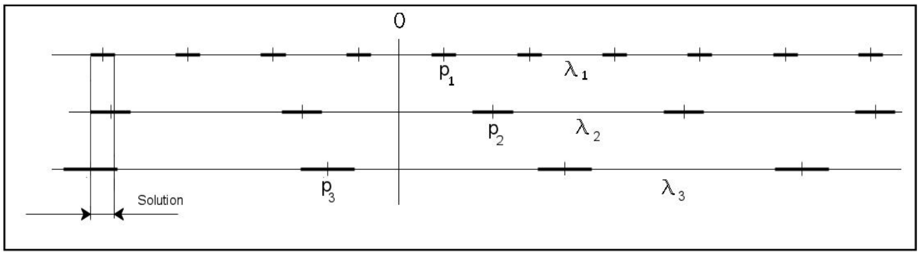

Figure 4.10: Finding the solution with the multi-lambda technique

Each horizontal line correspond to one wavelength and on each line the measured piston is indicated with its error. The measure is repeated with period equal to the wavelength due to the ambiguity described. By simply looking at the plot, it can be easily seen that the only possible simultaneous solution for the 3 wavelengths is the indicated interval in the left-bottom part of the plot. The capture-range, i.e. the interval within which it is possible to compute univocally the solution, depends on the chosen wavelength and on the uncertainty in the measurement at each wavelength. In general, if using just two wavelengths, the closer they are, the larger the capture-range is; on the other hand, if they are too much close, the ambiguity cannot be resolved completely in an interval close to the true zero.

Summarizing, we have designed a PSU able to sense the differential piston between adjacent shells in this way: the system project a collimated and diffraction-limited beam of 8-10 mm diameter onto the gap between the two shells. Then, working in autocollimation, the reflected beam is focused onto a detector. The projected image will be governed by diffraction laws. The intensity pattern will be the sum of all the different patterns, each one at a specified wavelength inside the selected bandwidth. Depending on the bandwidth and central wavelength, different coherence lengths will be obtained, modifying the sensitivity to differential pistons. Using more wavelengths, any ambiguity between repeated diffraction peaks can be removed.

Optical layout and mechanical components

In figure 4.11 is shown the proposed optical layout of the PSU. The system is illuminated by means of a point-like source(optical fiber), on the top-left of the scheme. A beam splitter is used to reflect half of the light towards the shells to be measured. The beam is collimated by means of an achromatic doublet, then it is reflected by the surface of the shells, focalized by means of the same doublet on the CCD indicated in the left side.

The dimensions sketched in the previous layout are indicative for a possible solution. Using a CCD with pixel pitch of $5\mu m$, the collimating achromatic doublet with a focal length of 250 mm, the sampling of θ_0 ranges between 3.0 pixels (at 600nm and with an aperture of 10mm) and 11.3 pixels (at 900nm with an aperture of 4mm). Different combinations are shown in table 4.3.

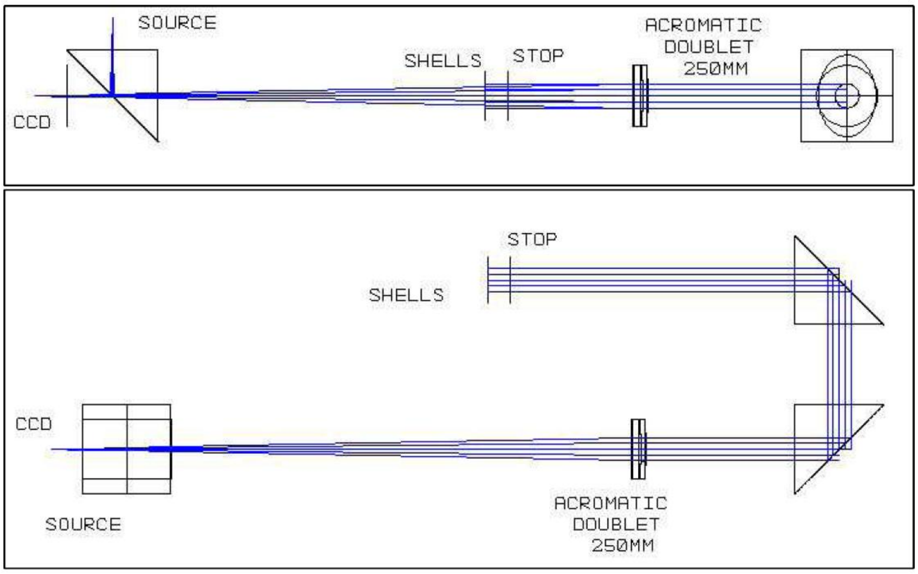

Figure 4.11: Optical layout (left and top views) of the Piston Sensing Unit

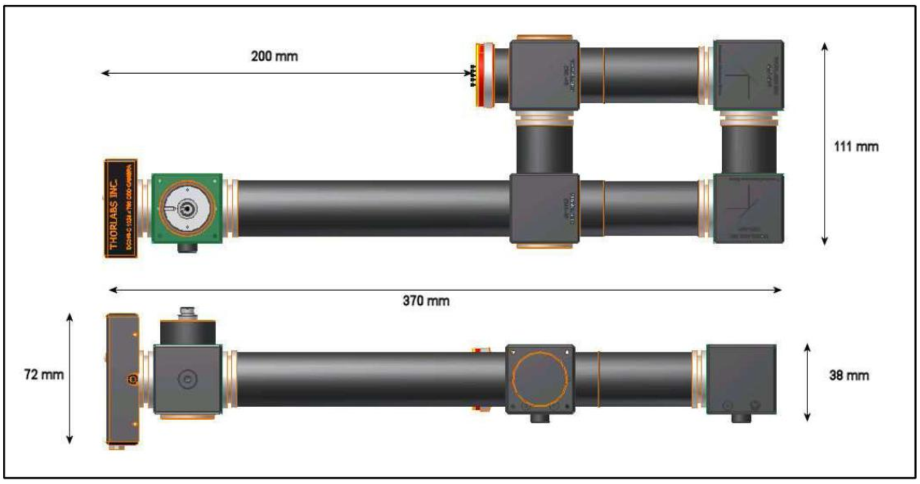

Figure 4.12: PSU mechanical layout

Table 4.3: Pixel sampling of the diffraction signal (θ_0) at the CCD plane for different sizes of the aperture on the shells.

Aperture (mm) Wavelength (nm)	10	8	6	4
600	3.0	3.8	5.0	7.5
700	3.5	4.4	5.8	8.8
800	4.0	5.0	6.7	10.0
900	4.5	5.6	7.5	11.3

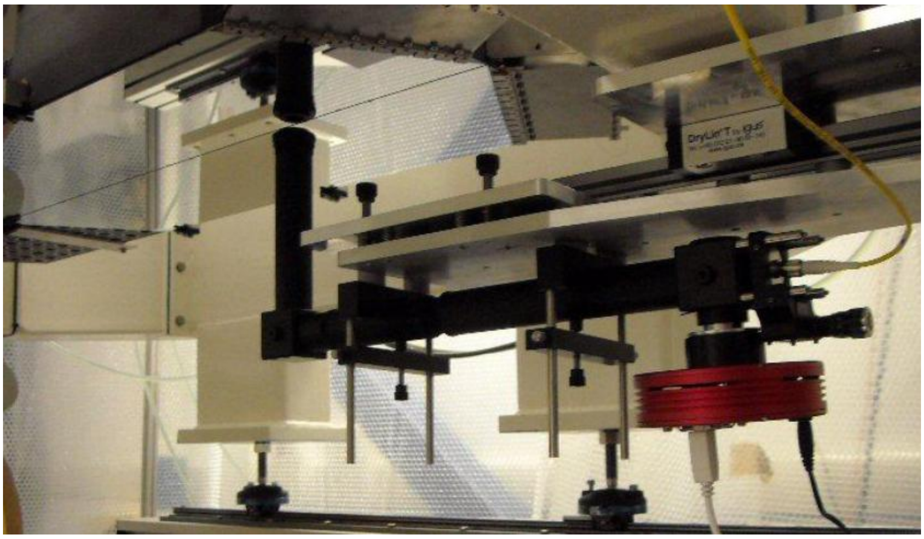

Figure 4.13: PSU mounted under the DP shells.

4.2.4 Ritchey Common Test

Our interferometer have a limited beam of 4 inches (10 cm), much smaller than the whole DP surface (96x40) cm. Then, a beam expander was required. Different solutions have been considered: the first one was a quite standard interferometric configuration, based on a paraboloidal mirror as large as the mirror under test. Figure 4.14 shows this layout. As a result, very large and expensive optical components, together with heavy mechanical mountings, were required, making this solution quite challenging.

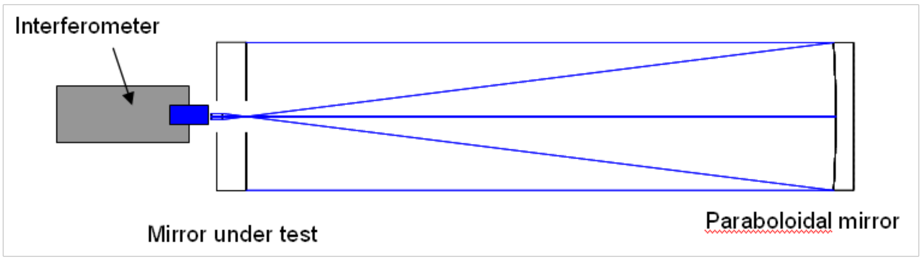

Figure 4.14: Paraboidal mirror configuration

As an alternative, an "all spherical surfaces" solution has been considered, by exchanging the paraboloidal mirror with a spherical one. A strong spherical aberration appears, and it is necessary to introduce a corrector, like a null lens or a computer-generated-hologram (CGH). However, a large and accurate $\sim$1m mirror is still required, together with a complex alignment system. So, also this configuration was discarded.

The almost rectangular aperture of the DP offered solutions based on relatively smaller optical elements.

We have designed an optical bench based onto *grazing* incidence angle configurations (see [26], [29], [37], [30]). At an angle α, a beam of diameter d covers a strip of length $d/cos\alpha$. With the help of an anamorphic collimator [49], forming an elliptical beam, it was possible to drastically reduce one of the dimensions of the optical elements. The anamorphic collimator consists of two paraboloidal cylindrical mirrors and one rectangular flat mirror. All these mirrors are in the order of 20-30 cm in size (this solution has been studied and reported in [23]).

However, such a configuration asks for quite complex optics (free-form optics), with increased risks, complexity, delivery time and cost, and it was discarded, too.

The final solution is the best compromise between the simple “all spherical” configuration and the grazing incidence one. We decided to adopt as starting configuration the so-called Ritchey-Common Test setup (see [48], [47], [17], [27]). For example, it was used in the past for large optical flats like the tertiary mirrors of the VLT. In this configuration the beam is not collimated but diverging, and its diameter increases linearly with distance. The surface under test is inserted into the optical path with an incident angle called Ritchey-Common angle (RCA), typically ranging between 30 to 60 degrees [17].

The only large optical element required by this test is a single spherical mirror, which closes the interferometric cavity sending back the beam to the interferometer. Concave spherical mirrors are the easiest shape to be polished, with the highest accuracy, and it can be tested in an absolute way. Figure 4.15 shows the optical layout of the standard Ritchey-Common test.

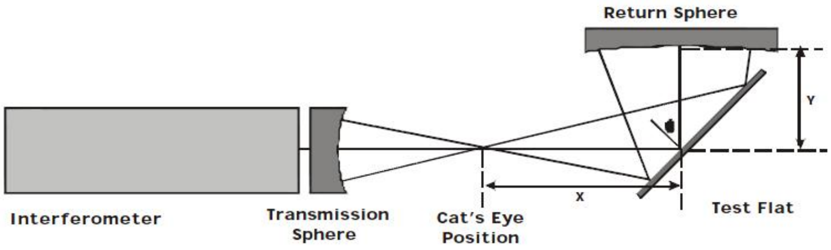

Figure 4.15: RCT standard configuration.

Optical layout

We start to describe in detail the optical layout. In our cases the mirror under test is the Demonstration Prototype, and one of the requirements is that the DP should be tested in a configuration, respect to the gravity vector, as similar as possible to M4AU orientation in the telescope layout. Many of the time, this mirror will look downward. In the adopted test layout the DP mirror is horizontal, looking downward.

The interferometer will launch a relatively fast $F/5$ beam. Two flat folding mirrors (50 mm and 150 mm diameters, respectively) direct the diverging beam onto the DP, making easier to align the whole cavity. With the help of the return spherical mirror ($50cm$ diameter), the test beam is reflected back on the DP, working in double pass configuration, and then to the interferometer.

In figure 4.16 some layouts of the optical configuration are shown. The RCA is slightly higher than $60\mathrm{deg}$ and it gives us the opportunity to measure the whole surface of the DP in "one shot".

Moreover, our set up is able to change the incidence angle, because this can help to better calibrate the absolute shape of the mirror under test. Figures 4.17 show the changing of the incidence angle.

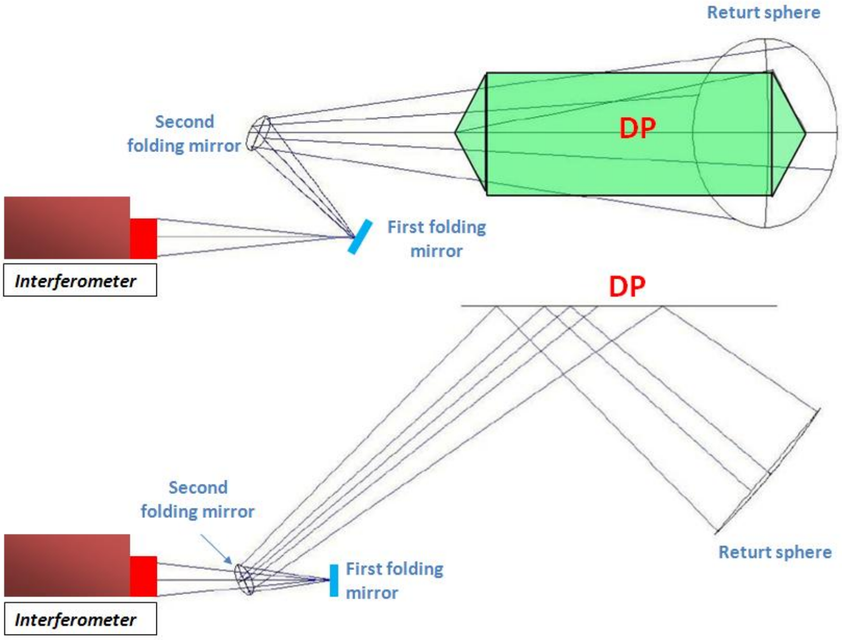

Figure 4.16: Optical layout of the R-C interferometric cavity. Top view (top) and side view (bottom)

There are two main effects related to the mapping of the surface shape: the first one is the variable anamorphic spatial sampling of the mirror surface, the second one is the variable sensitivity across the surface. Both effects are related to the varying incidence angle of the light beam on the DP surface. The first is just a projection effect (purely geometric terms) that can be analytically treated by ray-tracing analysis and corrected by software at a sub-mm accuracy. The spatial sampling varies according the following formula:

$$(X_s, Y_s) = \left(\frac{X_p/cos\theta}{1 - \frac{X_p tan\theta}{2F/\sharp}}, \frac{Y_p}{1 - \frac{X_p tan\theta}{2F/\sharp}} \right)$$

where θ is the angle of incidence of the chief ray (in the center of the pupil), $F/\sharp$ is the focal ratio of the incidence beam, (X_p, Y_p) are the normalized pupil coordinates and (X_s, Y_s) are the coordinates on the DP surface. This morphing effect can be visualized via ray-tracing, as shown in Figure 4.18 where a even spaced rectangular grid is projected onto the DP area. Also a rotation of the whole image can be seen, due to the skew optical layout of the RCT system (see Figure 4.16). The inverse transformation must be applied to images taken from the interferometer to get the undeformed DP surface. A SW routine was written to accomplish such a transformation.

The second effect, affecting how the surface shape Δ_s at the coordinates (X_s, Y_s) will be seen as a WFE (or OPD) at the normalized pupil coordinates (X_p, Y_p), is given by the following relation:

$$WFE_{(RCT)} = OPD(X_p, Y_p) = 2 \cdot \Delta_s(X_s, Y_s) \cdot cos(I)$$

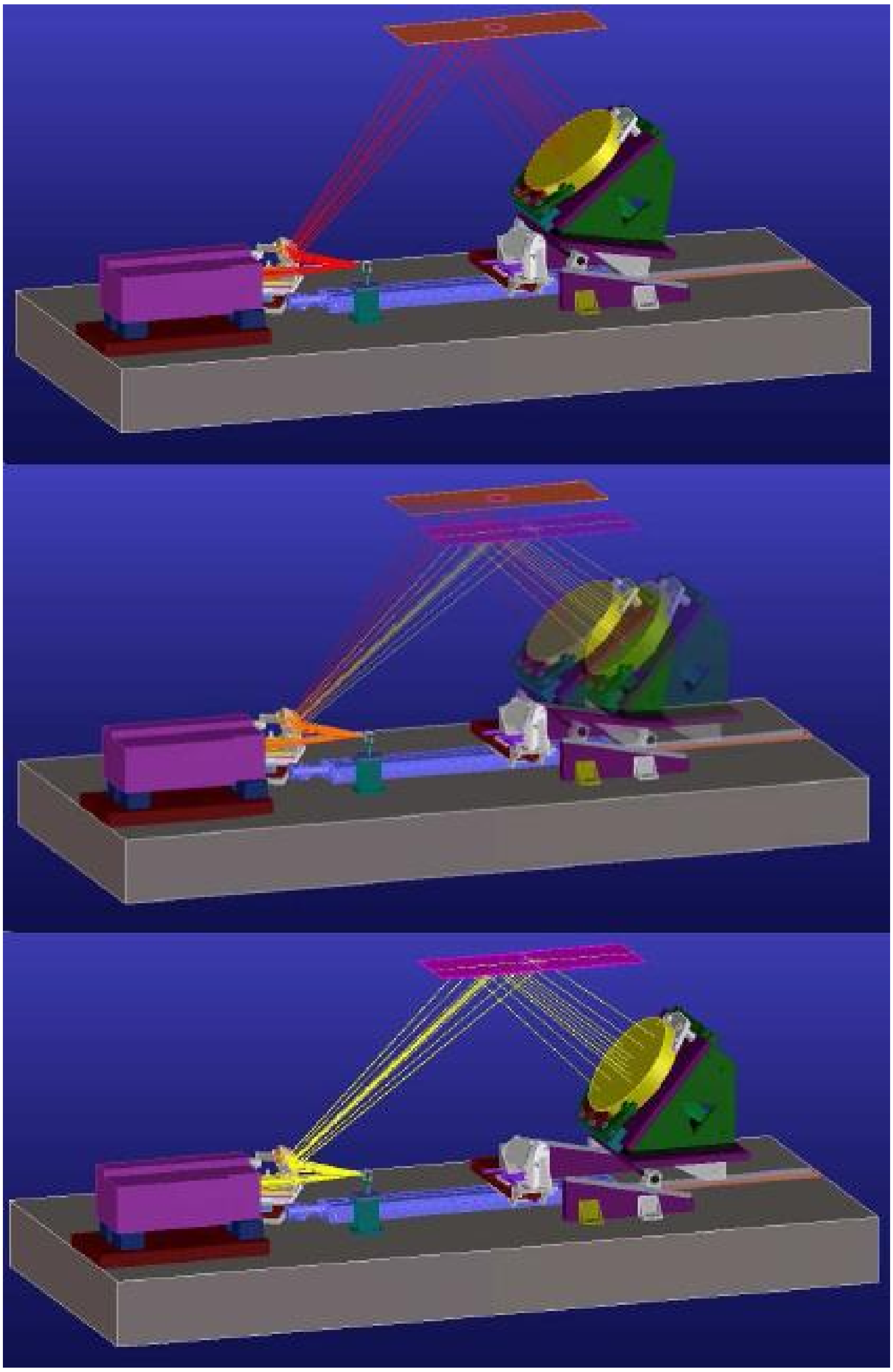

Figure 4.17: Changing of the RCA on the DP

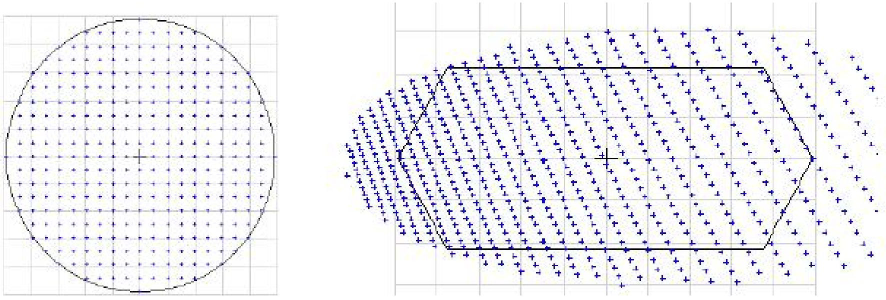

Figure 4.18: RCT spatial sampling over the DP surface. A regular rectangular grid at the exit pupil of the of the interferometer (left) is projected onto the DP (right).

where I is the incidence angle at the coordinates (X_s, Y_s). A further 2x factor must be taken into account for the double-pass over the same area, making it

$$OPD = 4 \cdot \Delta_s \cdot cos(I)$$

A conversion factor between WFE seen from RCT setup and the WFE as seen from EELT (or the DP, being a subsection of the M4AU area) can be derived. On EELT, a nearly collimated beam will be projected onto the M4AU surface (focal ratio >F/17), with a small incidence angle (8.5 deg), so we can approximate

$$WFE_{(EELT)} \approx 2 \cdot \Delta_s$$

Then:

$$\frac{WFE_{(EELT)}}{WFE_{(RCT)}} = \frac{1}{2cos(I)}$$

For example, when I=60 deg, the conversion factor is 1. For I=65 deg, its value is 1.18. The coordinate transformation depends mainly on the position of the DP with respect to the spherical mirror. It is possible to tune the parameters of the transformation (θ, $F/\sharp$, origin of the coordinates) by measuring the position of few actuators. Without applying the transformation law, an average conversion factor can be applied to get approximate information. At angle of incidence of 60 deg in the center of the DP area, the angle varies between 53 and 65, giving a conversion factor between 0.83 and 1.17 ($\pm$17%). The WFE is (on average) worse in one half of the DP area (up to 17$\%$ at the edges, or about 10$\%$ on average), and better in the other half (again, about 10$\%$ on average). Over the full DP area, average WFE will slightly differ from the real one, using the transformation law.

Tolerance Analysis and Error Budget

Sensitivities for alignment purpose are defined here as the image motion, as measured at the intermediate focal plane, when optical components are decentered or tilted. Image motion in the local focal plane coordinate system is defined as:

$$M = \left\{ \begin{array}{c} \Delta x(\mu m) \\ \Delta y(\mu m) \\ \Delta z(\mu m) \end{array} \right\}$$

where the X- and Y- axes lie in the focal plane, while Z- axis refers to defocusing.

Decenters and tilts of each optical component are defined with respect to the component local axes. We can define two matrices for each optical element, one defining image motion when the element is decentred (along local axes δX_i, δY_i, δZ_i), the other

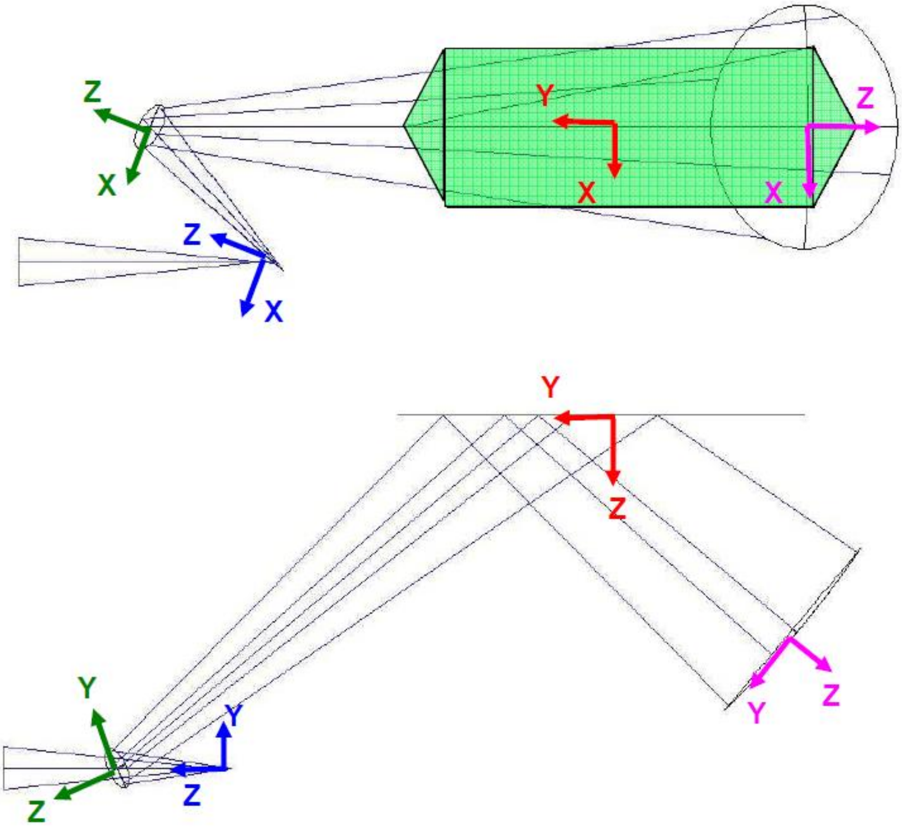

Figure 4.19: Coordinate local axes.

one when the element is tilted (around local axes of an angle $\delta\alpha_i$ around X_i, $\delta\beta_i$ around Y_i , $\delta\gamma_i$ around Z_i; all angles are positive according to the right-hand rule). Figure 4.19 shows the Local Axes for the optical components.

Table 4.4 gives the motion of the image that needs to be corrected to see the interferogram. This table gives information about the quality and precision that component mountings must achieve. We see that for this configuration the compensation is best done through fine control of the orientation of the FM2 folding mirror, mounted on a precision tip/tilt/decZ platform. Even the support of the spherical mirror must be designed in order to have a fine adjustment of the tip/tilt and a focus regulator.

Table 4.4: Image motion vs decentering or tilt of the different optical elements

ELEMENTS		δX 0.1mm	δY 0.1mm	δZ 0.1 mm	$\delta\alpha$ 1arcmin	$\delta\beta$ 1arcmin	$\delta\gamma$ 1arcmin
Folding Mirror1	Δx	-	-	-159	-	29	-
	Δy	-	-	-	-26	-	-
	Δz	-	-	366	-	-	-
Folding Mirror2	Δx	-	-	128	79	-421	-
	Δy	-	-	-146	414	138	-
	Δz	-	-	-348	-	-	-
DP Mirror	Δx	-	-	-95	-611	1196	-
	Δy	-	-	-288	-1861	-392	-
	Δz	-	-	-	-1	-	-
Spherical Mirror	Δx	188	62	-	449	-1368	-
	Δy	-62	-188	-	1368	449	-
	Δz	-	-	-200	-	-	-

A second sensitivity analysis is related to the residual wavefront errors (WFE) due to slight misalignments of the optical components. To obtain such a sensitivity, we simulated the way the measurement setup will be used, i.e. best alignment will be done acting on the folding mirror FM2 during closing the cavity. We defined this residual WFE as the sensitivity to Z-misalignments of the FM2. As a result, negligible WFE will be added from residual misalignments. A not negligible effect will be the vignetting of the beam onto the different optical surfaces, if large displacements (dec and tilts) are introduced. Some care must be applied to check vignetting.

This Ritchey-Common setup exhibits some interesting properties that should enhance final accuracy. All components can be fully tested in absolute sense. Plane mirrors can be checked with a very precise reference flat. Moreover, a three-flat test can be performed, if necessary. The spherical mirror can be tested again in absolute sense, if three measurements are done; so its surface can be known within an overall accuracy of 1/100 wave (RMS) or better.

From simulations, we know that during the calibration of the interferometric cavity, residual WFE can be subtracted increasing overall accuracy. However such a numerical calibration will be limited by mismatch between different wavefront maps. Maximum residual WFE must be below a reasonable level, e.g. 1/8 wave, i.e. 75 nm (rms). We can now build an error budget, both for manufacturing errors, and misalignments, shown in table 4.5.

Mirror specifications are defined in 4.6. They are within current manufacturing capabilities. About misalignments, as noticed above, they can be fully corrected with the folding mirror fine adjusting movements. In table 4.7, alignment and adjustment requirements for all optical elements are given.

In order to correctly place optical elements, some adjustment devices are needed.

Table 4.5: RCT Error Budget

CONTRIBUTORS	ΔWFE **(rms)** (nm)
Transmission Sphere (Interferometer)	10
FM1 folding mirror	20
FM2 folding mirror	40
Spherical mirror	60
Misalignment	-
TOT. (RSS)	75

Table 4.6: Mirrors Specifications

	FM1	**FM2**	**Spherical Mirror**
Material substrate	Zerodur	Zerodur	Zerodur
Radius of curvature	Infinity	Infinity	2500mm (± 1)
Clear area	50 mm diameter	150 mm diameter	500 mm diameter
Thickness	10 mm	25 mm	> 80 mm
Surface accuracy (at 633 nm)	PtV < $\lambda/20$ RMS < $\lambda/100$	PtV < $\lambda/20$ RMS < $\lambda/100$	PtV < $\lambda/10$ RMS < $\lambda/20$
Coating	Al (protected)	Al (protected)	none
Microroughness	Scratches/Digs 60-40	Scratches/Digs 60-40	Scratches/Digs 60-40

Resolutions on adjustments have been driven by the required alignment accuracies. Similarly, adjustment ranges depend on mechanical and manufacturing accuracies of optical elements and related mountings.

4.2.5 Procurement and Acceptance Test

After the design phase, a procurement phase followed. A list of main optical, mechanical, hardware and software components are listed in table 4.8.

The large spherical mirror was the first element to be ordered, because of the long delivery time and high cost.

Also the three (one for the RCT, the other two for the SIS setup) flat folding mirrors were ordered as off the shelf components. Then, a custom reflective coating was applied on the two flat folding mirrors of the SIS setup (see 4.2.2). All the mechanical components of the RCT has been designed and produced at INAF premises. All the requirements about the adjustment resolutions and ranges were fully achieved. We briefly describe only the more critical support, i.e. the spherical mirror support.

This support should hold the mirror without deforming it. A nine contact points support keeps the mirror in place. Three symmetrically located lever mechanisms are used (as in the classical Hindle mount) [58]. They are angularly equidistant on a circle of radius R1 (see the green circle of Fig.4.20). The support points will host the fine regulation for the optical alignment of the mirror. Each support point is connected by a triangular plate to other three contact points, resulting in a nine contact points on the back side of the spherical mirror. The location of the nine contact points is such that an even load is reached on the contact points (see the red and blue circle of the same figure).

Table 4.7: RCT Alignment requirement with range and resolution

	Alignment requirement			**Adjustment range**	**Resolution**	
Folding Mirror 1	δX	1	(mm)	-	-	(mm)
	δY	1		-	-	
	δZ	1		3 mm	0.1	
	$\delta\alpha$	5	(arcmin)	30 arcmin	1	(arcmin)
	$\delta\beta$	5		30 arcmin	1	
	$\delta\gamma$	-		-	-	
Folding Mirror 2	δX	1	(mm)	-	-	(μm)
	δY	1		-	-	
	δZ	-		20 mm	1	
	$\delta\alpha$	-	(arcmin)	45 arcmin	1	(arcsec)
	$\delta\beta$	-		45 arcmin	1	
	$\delta\gamma$	-		-	-	
DP Mirror	δX	2	(mm)	-	-	(mm)
	δY	2		-	-	
	δZ	1		5 mm	0.1	
	$\delta\alpha$	2	(arcmin)	15 arcmin	1	(arcmin)
	$\delta\beta$	2		-	-	
	$\delta\gamma$	3		-	-	
Spherical Mirror	δX	1	(mm)	-	-	(mm)
	δY	1		-	-	
	δZ	1		5 mm	0.1	
	$\delta\alpha$	1	(arcmin)	15 arcmin	1	(arcmin)
	$\delta\beta$	1		-	-	
	$\delta\gamma$	-		-	-	

The mirror is also supported on the edge on six points. This system is composed by two symmetrical pivots sustaining two arms. One side of each arm is connected to a cylindrical pad and the other is fixed to a pivot holding a triangular structure. On each of this triangular structures are fixed other two cylindrical pads. All cylindrical pads will be slightly curved as a barrel, in order to obtain a real point-like contact, instead of a line contact. The two external pads allow for self-centering of the mirror. A FEA analysis has been performed on the complete system, including mirror support. All the assembly composed by the spherical mirror and its support is modeled in Ansys via solid elements. With regard to the support of the mirror, all the parts are made of aluminum. The spherical mirror has a thickness of about 80mm and is composed by Zerodur. The load considered was a body gravitational field acting on a direction tilted of 45° respect to the optical axis. About the constraints, we have assumed the side end of the two cylindrical bars to be completely fixed (no degrees of freedom). Displacements of the optical surface has been post-processed by fitting with Zernike polynomials. Piston and tip-tilt has been removed, obtaining a **PtV=130** nm and **RMS=26** nm, well within our error budget. These values were compared with measurements made on the mounted mirror.

When the spherical mirror and its support have been delivered, different acceptance tests have been performed. The first one has been the absolute calibration of the return sphere, in order to check the surface quality of the mirror and also to calibrate our setup. To test the spherical mirror was necessary to design a specific setup. A concave

Table 4.8: Main component parts.

	RCT	SIS	PSU
OPTICS	Spherical Mirror Flat Folding Mirror	2 Flat folding mirror	Catalog Lenses
MECHANICS	Custom Support Home Made	Custom Support Home Made	Catalog Component
HARDWARE	none	Linear Stages Piezo tip/tilt Stage	CCD Camera
SOFTWARE	Intelliwave SW for Interferometer		

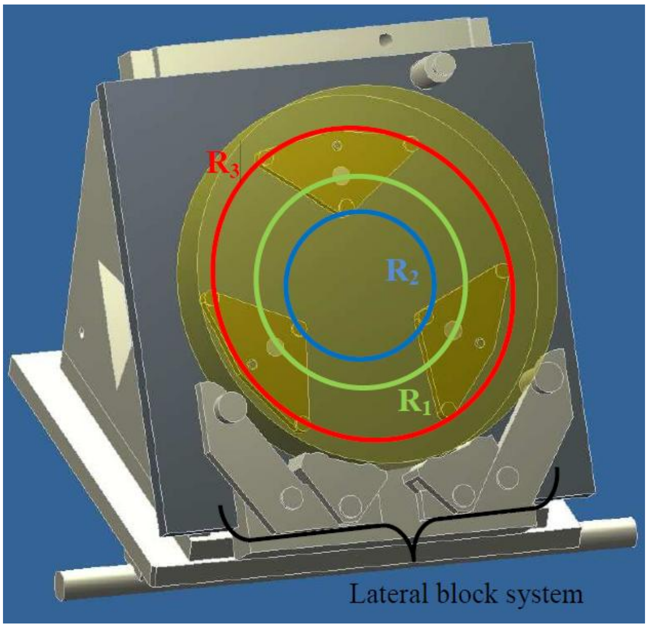

Figure 4.20: The Spherical Mirror Support

spherical surface is examined for surface figure and irregularity by placing its center of curvature coincident with the focus of the transmission sphere. The radius of curvature of our spherical mirror is 2540mm (i.e. 100 inch). We have tested the surface in his working angle of the RCT test. In order to measure the tilted surface of the spherical mirror, a flat folding mirror has been used to direct the light beam on the spherical mirror.

Figure 4.21 shows the optical layout of the configuration test.

It is possible to absolutely measure the entire surface of the spherical mirror as defined by the spherical surface certification (SSC) method [51], [42] . The absolute characterization asks for three different wavefronts maps, W_1, W_2 and W_3. The first is the wavefront map obtained with the test surface measured at its center of curvature at an azimuthal orientation of $0°$. W_2 is the wavefront obtained with the test surface measured at its center of curvature at an azimuthal orientation of $180°$. Finally W_3 is obtained when a flat mirror is placed at reference sphere focus, where odd errors in the interferometer cancel each other. Then:

$$W_1 = W_R + W_T + W_S$$

$$W_2 = W_R + W_T + W_S^{180°}$$

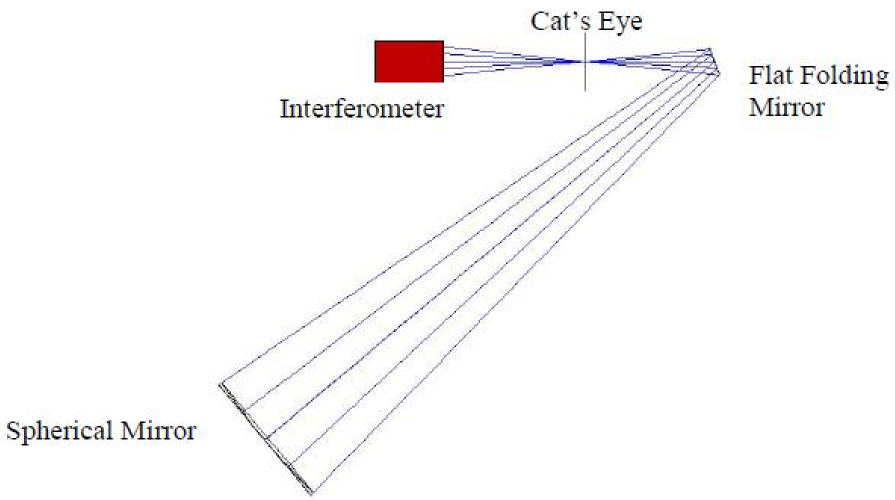

Figure 4.21: Optical layout of the measurement configuration

$$W_3 = W_R + 1/2(W_T + W_T^{180^\circ})$$

where W_R is the reference arm, W_T is the test arm and W_S is the surface wavefront. The desired surface is :

$$W_s = 1/2(W_1 + W_2^{180^\circ} - W_3 - W_3^{180^\circ})$$

The procedure followed for the measure of the spherical mirror was as follows:

1. The mirror was positioned on its support.
2. The transmission sphere was loaded into the interferometer.
3. With the help of the regulation system, the mirror was aligned till a residual defocus less than 100 nm was reached.
4. The first measurement was taken.
5. The spherical mirror was removed and replaced many times and different measurements have been taken, stored and compared.
6. The spherical mirror was rotated around its normal by 180 degrees.
7. A new set of measurements was taken and stored.
8. A small high quality retro-reflector was placed with its vertex in the catś eye position and in this position a new measurement was taken.

The absolute calibration of the surface of the spherical mirror was calculated by software (IDL) computation. The script creates the wavefront maps necessary to the absolute calibration formula, W_1, W_2^{180}, W_3, W_3^{180}, counter rotating the W^{180} images. Then, it computes the centroid (x_c, y_c) of each maps and shifts them in order to have the same x_c, y_c . Final subtraction is done onto these images.

As a result, a "blind" mounting of the mirror can be done, keeping surface deformation below specifications. The manufacturer of the mirror measured (in different conditions) a **RMS = 5 nm**, and a **PtV = 34 nm**, over 99% of the surface area. We have defined a requirement of 75 nm (RMS), for the RCT cavity wavefront error, and assigning a 60 nm (RMS) to the spherical mirror. According to our measurements, the

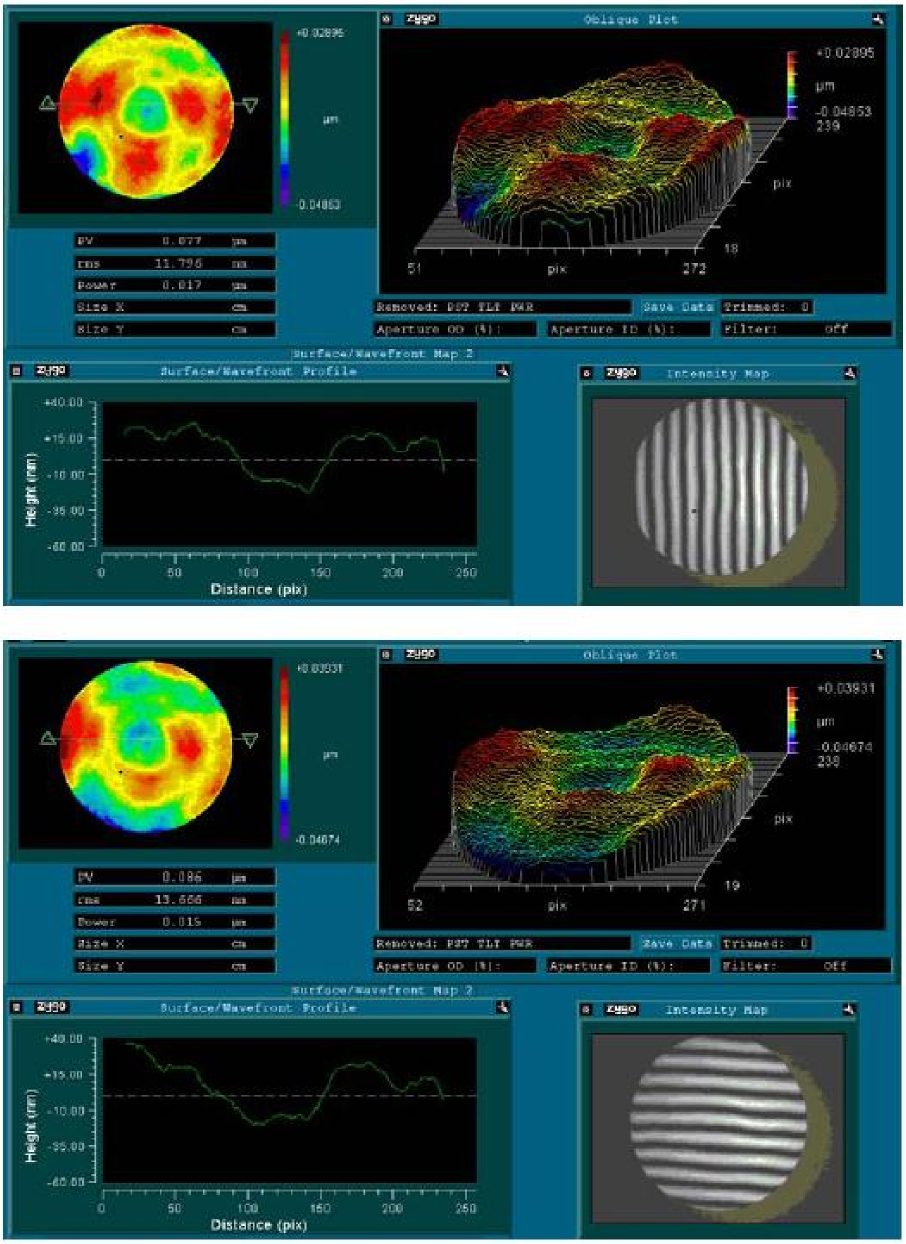

PV 0.077 µm
rms 11.796 nm
Power 0.017 µm
Size X cm
Size Y cm
Removed: PST TLT PWR
Trimmed: 0
Aperture OD (%):
Aperture ID (%):
Filter: Off

PV 0.086 µm
rms 13.666 nm
Power 0.015 µm
Size X cm
Size Y cm
Removed: PST TLT PWR
Trimmed: 0
Aperture OD (%):
Aperture ID (%):
Filter: Off

Figure 4.22: Wavefront maps of the spherical mirror, under different tilt conditions (see interferograms).

spherical mirror exhibits a WFE of <90 nm (PtV) and <15 nm (RMS), for the whole mirror surface, well within the stated value (see Figure 4.22).

The discrepancy between our measurements and those ones made by the mirror manufacturers are to be identified as residual shape errors due to the different gravity load, and the presence of a flat folding mirror used in double pass. According to FEA analysis, a perfect mirror should be bent by more than 26 nm (RMS).

Due to the very low error due to the spherical mirror (surface error <15 nm RMS), no attempt was done to subtract this error from the measurements of the final WFE, because this implies a careful match of the surface error map and the projected DP area on the spherical mirror itself. Fiducials were not put inside the spherical mirror. We consider such approximation quite reasonable, because noise should be introduced in the final measurements, more than correcting for a quite small error.

The procurement of the components of the SIS and PSU setups was simpler. Another important acquisition of our laboratory was the new software of the interferometer, IntelliWave, from ESDI (US). A new frame grabber has been installed and also the control of the piezo shift of the *phase–shifter* has been changed.

Other HardWare and SoftWare Interfaces

Once optical bench and DP were installed together, it was necessary to build a set of communication interfaces between the optical measurement system and the DP control system (DPCS).

Two PCs control the whole measurement system, via USB and RS232 connections, while the external interfaces and data exchange is routed via our network. Also the HW/SW interface with the DPCS is acted through a LAN connection. Exchange files have been defined on both sides of the system to control the DP status, send commands, and receive positions and forces from DP. The DP control system (DPCS) has been successfully integrated within our HW/SW systems in order to communicate each other. The DP is monitored by a dedicated PC under MatLab, to check safety and health of the DP system. Many parameters are kept under control, like temperatures, fluxes, currents, forces, positions. This system is also in charge to execute commands on the DP, sent from our Optical Tests Control System (OTCS) via network connection (LAN). Commands are checked before execution, to skip those ones not satisfying all requirements.

A second PC is responsible to run the RCT, SIS, and PSU measurements, move linear and tip-tilt stages when needed, process all the information under IDL, and send commands to the DPCS. It also reads the status of the DP shells (positions and forces), for further analysis.

In other words with all this architecture we were able to see the interferogram map of the DP surfaces, translate the wavefront map in position-vector of the actuators, calculate the new position of the actuator to flattening the wavefront and send the command to the actuators. All these procedures are described in detail in section A

4.2.6 The preliminary tests

The following pictures show some phase of the integration of the optical bench. In figure 4.23 a layout of the Optical Bench is drawn.

During the integration of the optical bench a first rough alignment of each subsystem has been performed.

The RCT cavity

The RCT cavity has been closed with a circular flat mirror placed in the same position of the DP. In this way we can position all the other components (spherical mirror,

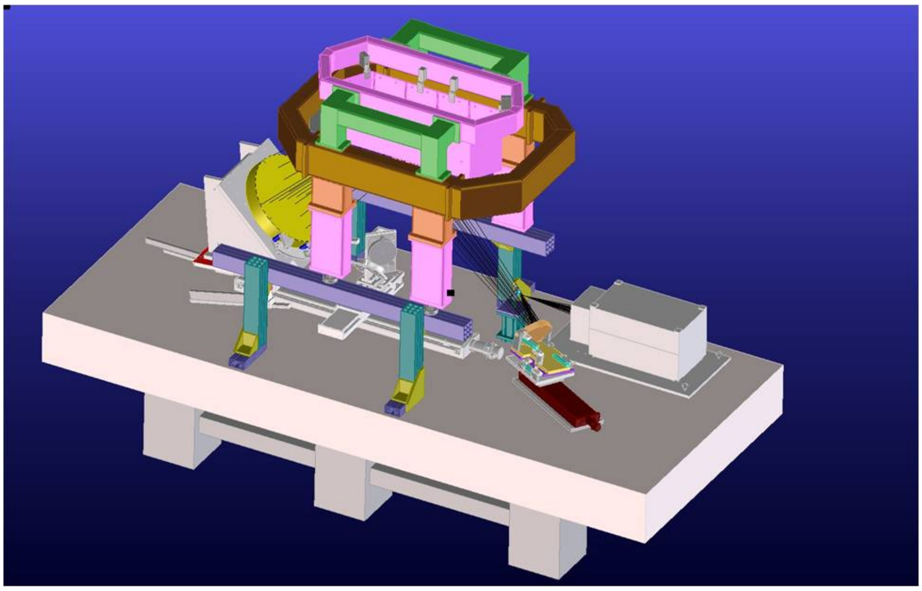

Figure 4.23: Mechanical layout of the Optical Bench.

flat folding mirror) near to their final position. With the installation of the DP, the alignment of the cavity can be done via fine adjustments on the folding mirrors (tip/tilt in the first one, tip/tilt and focus in the second one) and on the spherical mirror (tip/tilt and focus). The DP position can be controlled through two horizontal rails that provide a 40 cm range to cover different areas over the DP surface, and through four screws at the bottom of the legs of the DP support structure. They help to the first rough alignment of the cavity length and the tip/tilt.

The SIS cavity and SIS software

For the SIS cavity, the interferometer head and the folding mirrors have been aligned in order to have 90 degree deviations at each reflection. Moreover, the optical beam has been aligned in order to be parallel to one of the motorized stages (X-axis). Indeed, any misalignment between X-axis and the optical beam will shift beam footprints onto the folding mirror surfaces, and their surface errors will be applied on different pixels during the measurement process. To remove these errors, the WFE contributions due to surface errors of the folding mirrors must be the same at each position of the folding mirrors. This error has been measured in an absolute way and subtracted from each single WFE map before the stitching reconstruction. This operation is done by the SIS_SW. The cavity error has been measured in an absolute way and subtracted from each single WFE map before the stitching reconstruction. This calibration of the SIS cavity was done using a Fused Silica flat uncoated mirror of good quality (17 nm RMS). This mirror was put before and after the folding mirrors with fiducials. Subtraction of the two surface maps gave the cavity error, about 30 nm RMS. Even if small, this systematic error, if not properly subtracted, should give an overall low-frequency error on the stitched image. In figure 4.25 is shown the map of such surface error, averaged over > 20 images. Also repeatability has been checked, being smaller than 2 nm rms.

Another calibration was the spatial sampling of the interferometric camera, once in SIS mode. To enhance repeatability, we selected the un-zoomed mode of the acquisition camera (1X). Then, based onto the good linear absolute calibration of the linear stages (given within $< 10\mu m/100mm$, or 0.1 mm over the whole linear range in the X

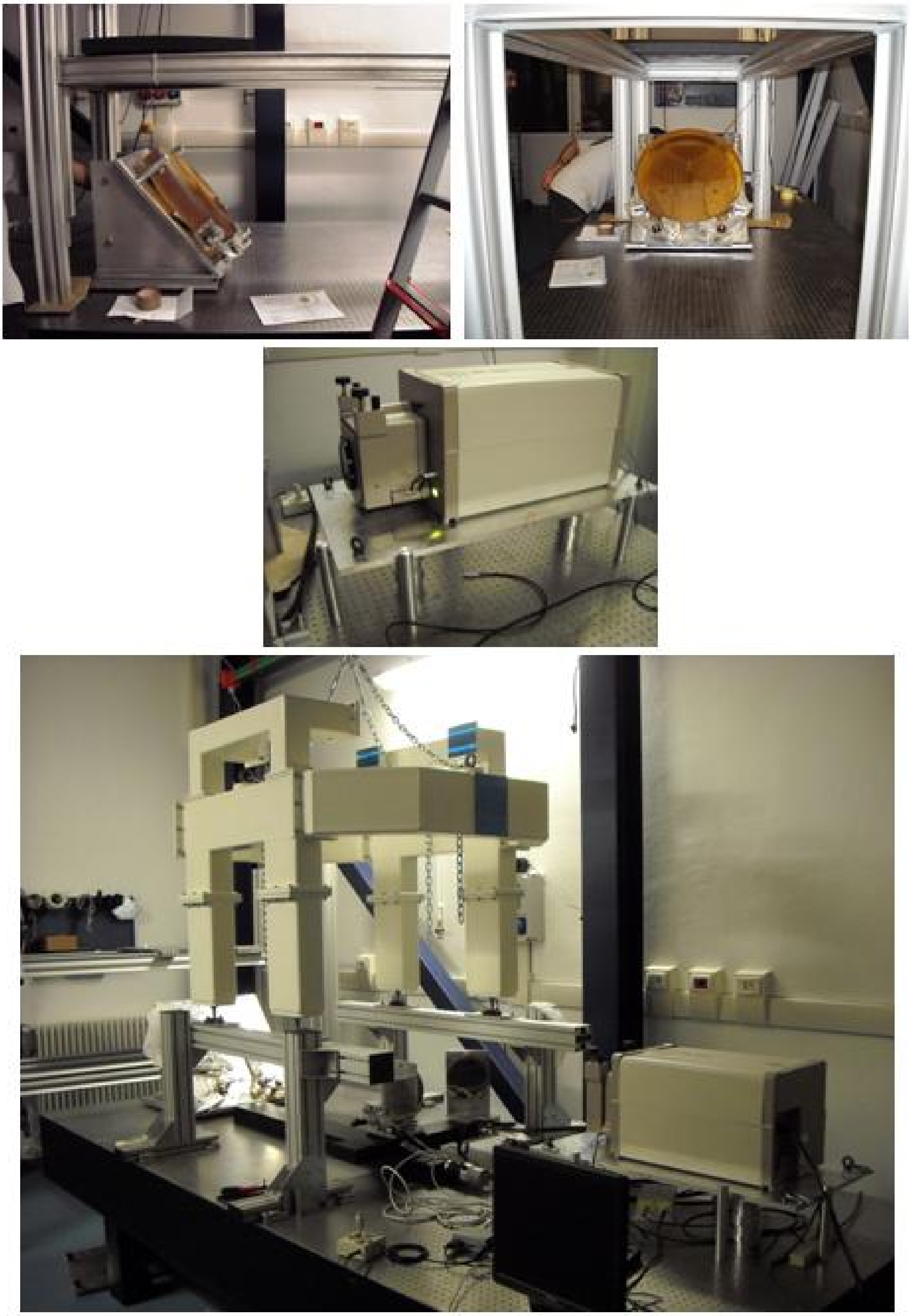

Figure 4.24: In the first two images we can see the final integration of the Spherical mirror with his support. In the central picture, the support of the Zygo interferometer. This support holds and raises the interferometer at the correct height. The last picture shows the Optical Bench integrated and ready to host the DP

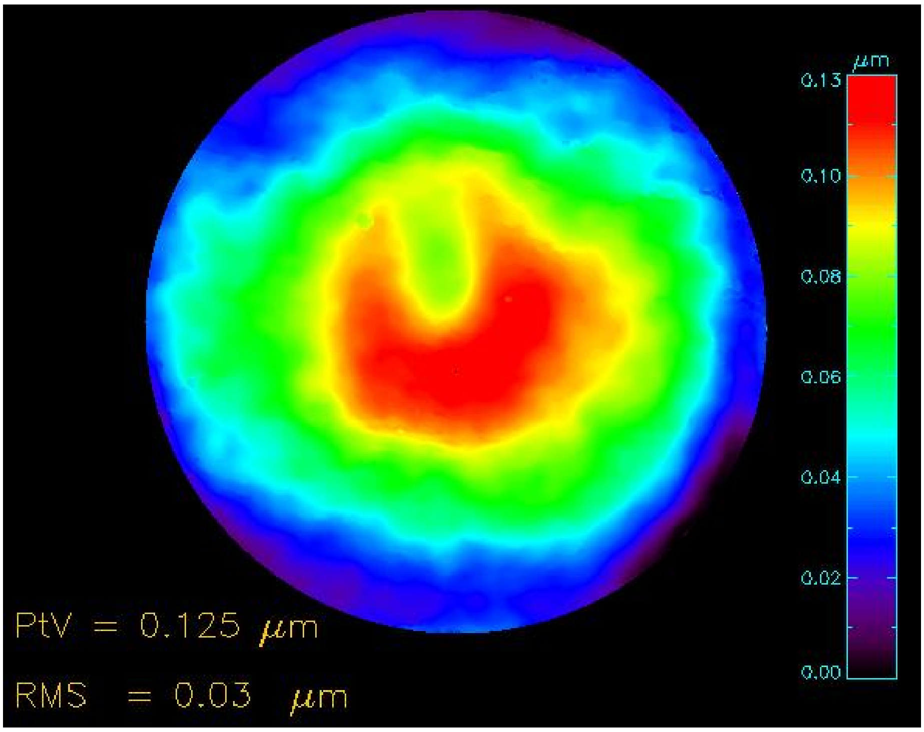

Figure 4.25: SIS cavity wavefront map

axis), two positions of a well defined fiducial was kept with the interferometer, moving the linear stage by about 90 mm. Measured pixel scale was $3.97 \pm 0.01 pixel/mm$.

Finally some preliminary tests were done on a 200mm flat mirror to test and fine tuning the reconstruction SIS_SW described before.

For this test the mirror was place on top of our linear stages, to move it horizontally. Due to the lack of a vertical stage and the horizontal setup of the interferometric cavity, the shift along the Y-coordinate has been done manually, using aluminum blocks. Some fiducial targets have been randomly sticked onto the surface of the mirror in order to check the accuracy of the data processing. The stitching process has been tested onto 18 images. As a check, the same mirror was sent to SAGEM in order to have an interferometric map of the whole surface. The same area was measured with a large interferometer at SAGEM. In figure 4.26 we can see the 200mm test mirror and some of the acquired SIS WFE maps. Figure 4.27 shows the coordinate system to locate the single maps and the mapping sequence.

The stitched image is shown in figure 4.28. The presence of the small spots proves that the images have been well aligned in XY. If not, spots should disappear, because of the averaging method. After the stitching, the whole image has been processed and analyzed applying the usual Zernike polynomial fit.

In figure 4.29 it is possible to see the wavefront map of the whole mirror stitched by our software and the same wavefront map taken by SAGEM. Both images were fitted using standard Zernike polynomials. The two maps look similar. A quantitative comparison shows that they differ by a 20% amount. Indeed, the stitched map has a WFE (RMS) = 44 nm, while the whole map gives WFE (RMS) = 55 nm.

The map of the residuals is shown in figure 4.30 and the residual error is of the order of 20 nm (RMS), as expected from RSS subtraction.

As a remark, SIS was considered well calibrated if large surface errors must be measured, due to its inherent better sensitivity to high frequency errors. These are the

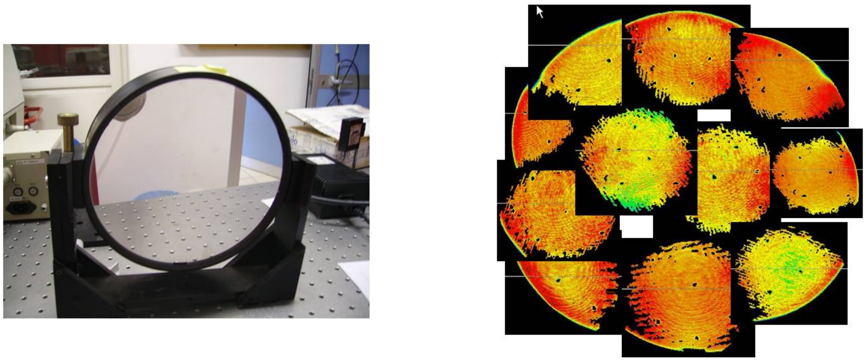

Figure 4.26: The mirror measured (left side) and some interferometric map (right side)

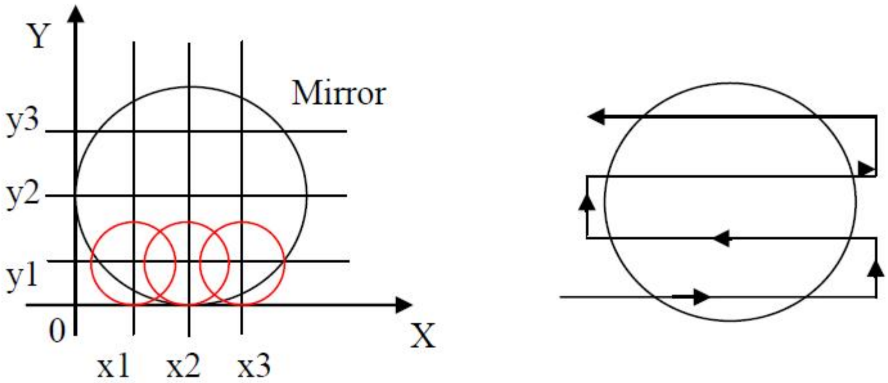

Figure 4.27: Coordinate system to locate single interferometric maps (left) and selected mapping sequence (right).

typical errors that can be expected after shell installation, because it has been performed without any optical feedback.

The PSU prototype

A prototype of the Piston Sensing Unit (PSU) has been integrated to check the working principle and to obtain measures for the optimization of the design of the final unit. The PSU prototype layout and a picture of the full system integrated on the optical bench are shown in figures 4.31 and 4.32.

As visible from figure 4.32 the PSU experiment consists of:

- a point source
- a collimating lens which collimates the beam coming from the point source
- a beam splitter which reflects light towards the segmented mirror mounted on the piston simulator
- an aperture stop just before the reflecting segmented mirror
- a focusing lens which focalizes the beam after reflection
- a CCD which records the image patterns.

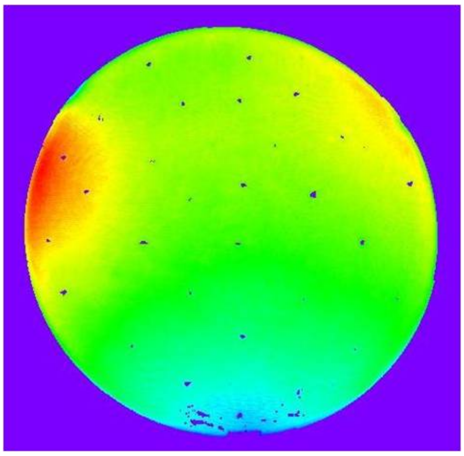

Figure 4.28: The stitched interferometric map of the 200mm diameter mirror. We note the presence of fiducials

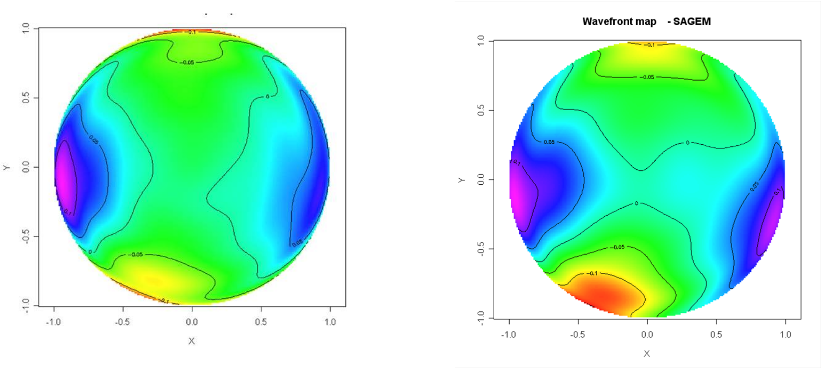

Figure 4.29: Interferometric map stitched and fitted with Zernike Polynomial(left side) and one shot interferometric map by SAGEM (right side). Contour maps are measured in micron.

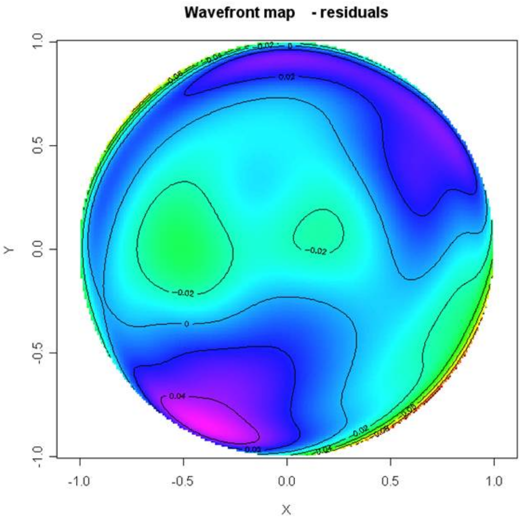

Figure 4.30: Wavefront maps of the residual

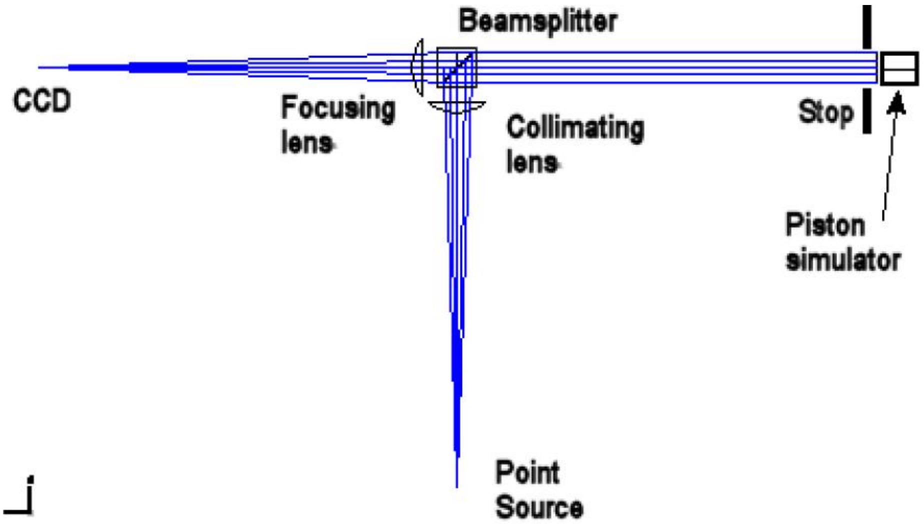

Figure 4.31: Optical layout of the PSU prototype.

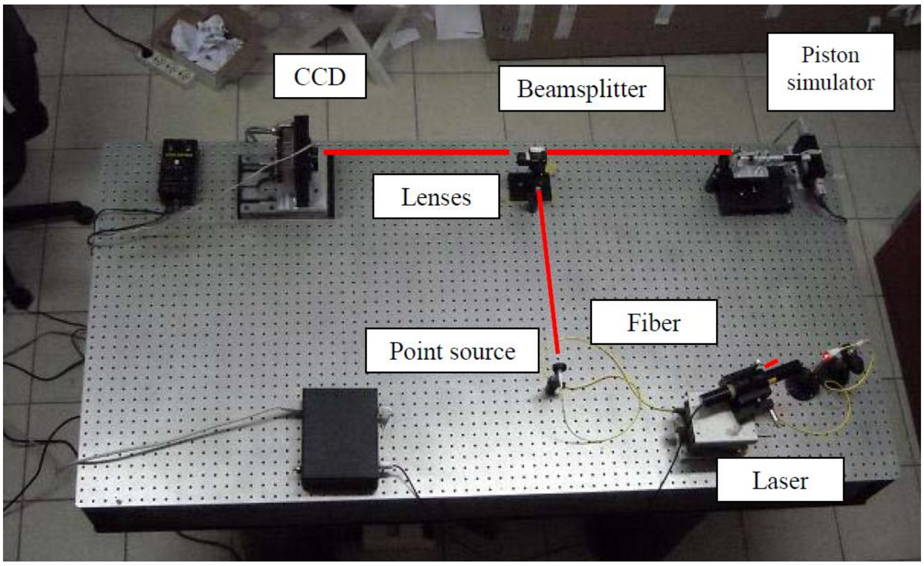

Figure 4.32: Picture of the layout of the PSU prototype with the indications of the light path (red line) and of the main components

The point source is realized with a mono–mode fiber (core 4 μm) fed by a He-Ne laser (632.8nm). The pixel size of the CCD (E2V 47-10) is of 13 μm. The collimating and focusing lenses have nominal focal distances of 500 mm. Note that for the final PSU a different CCD and different lenses have been selected to allow a much more compact layout. The *piston simulator* (for more detail see [24]) consists of a pair of cubes with the reflecting surface oriented towards the beam splitter. Each face of each cube has a flatness of $\lambda/10$ and the orthogonality between each faces is about $90° \pm 10''$ i.e. $\approx \lambda/10$. Both resting on a flat plane optically worked. In this way we are sure that the cubes have as a reference the same surface. One of the cubes is fixed, while the second can slide, pushed by means of a linear piezo–motor remotely controlled. The contact between the adjacent faces is imposed by a mechanical force (see figure 4.33) which assures parallelism of the vertical axes. Differential steps of the order of one nanometer can be applied.

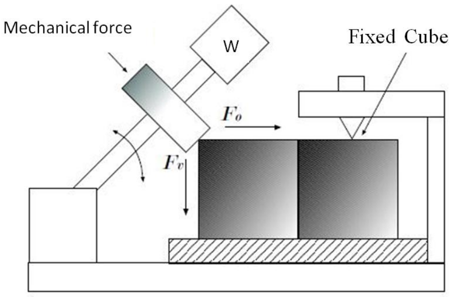

Figure 4.33: Vertical section of Piston Simulator

An image of the piston simulator (developed by the Arcetri Observatory in Florence) is reported in figure 4.34.

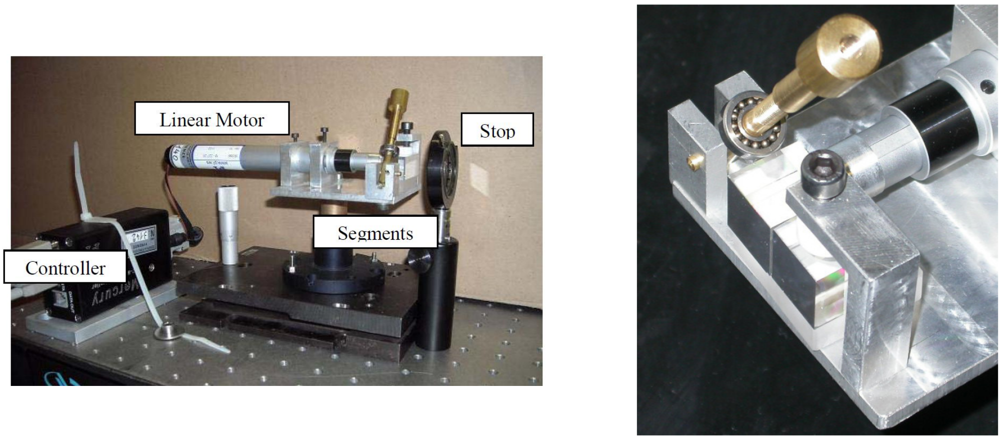

Figure 4.34: The Piston Simulator

A first set of image has been obtained with monochromatic light, with a circular aperture of 4 mm in diameter and with the piston which was moved by a few hundreds of nanometers. The recorder signal and the normalized intensity profile are reported in the plot in figure 4.35 for 4 different piston steps.

The complete variation of the intensity profile when the wavefront piston step changes between -$\lambda/2$ and $+\lambda/2$, with steps of $\lambda/12$ is shown in the plot in figure 4.36

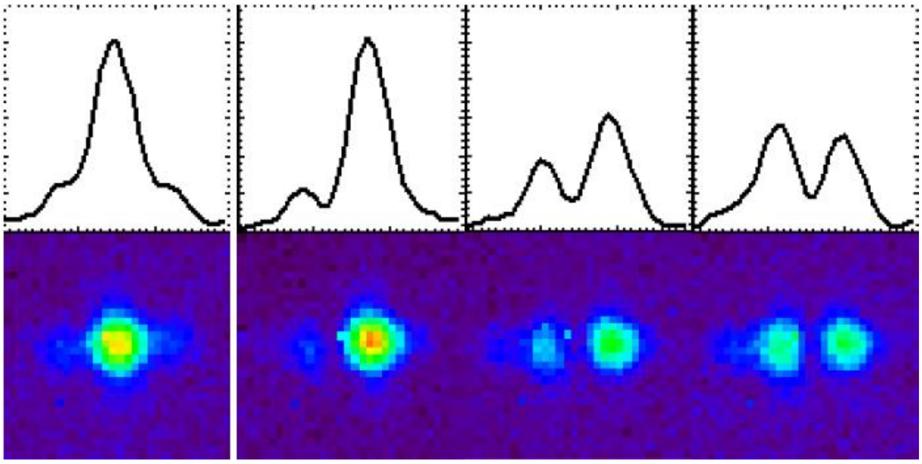

Figure 4.35: Signal recorder at four different steps.

A first analysis of the signals has been performed to compute roughly the piston steps. The results are reported in figure 4.37

The measures were qualitatively in agreement with the set values. A quantitative estimation is not easy because the effective resolution of the piston simulator is of 50nm and the current setup does not allow an absolute calibration of the system. Anyway those measurements allowed to check the basic principles of the PSU. The periodic behavior with period λ is clearly seen, which confirms that the pure monochromatic light can give only measures of the piston step with 1λ ambiguity. The measured repeatability of the order of few nanometers has been achieved.

The Optical Bench

In order to check the thermal stability of the Optical Bench, after final integration of both RCT and SIS systems onto the optical bench, some measurement runs were done closing the cavity with a 200mm flat mirror. Facility room was not thermally controlled, but due to its high thermal inertia very slow changes happen. Figure 4.38 gives the WFE (nm rms) variation of the cavity during a 16 hours test. Bold lines are the WFE (rms) and the delta-temperature (multiplied by a 100X factor to show variations). As shown, b Both WFE and temperature are very stable, in fact we have:

- $\Delta WFE < 5nm$
- $\Delta T < 0.5°C$

These pretty stable operational conditions inside the room helped to run calibration measurements. When temperature inside the room varies more than $0.5°C$, the main effect is change of the height of the mechanical structure where the DP is mounted. This will translate into a change into the cavity length, and additional tip-tilt and defocus aberrations will develop. From ray–tracing simulations we estimated this effect as large as **2.5 nm (rms) per micron of height change**. Considering typical sizes of the mechanical structure of the cavity (1 m of stainless steel, $CTE \approx 13e - 6/°C$), up to few 10 nm rms can be expected

The DP arrived in Merate on 25 November 2009. In figure we can see the thin shell with his 111 glued magnets. After a thorough cleaning with the help of a “elevator” designed expressly for the installation and dismantling of shell in the back-structure by ADS, the shells has been installed one by one. The whole DP structure has been placed on the Optical Bench (see figure 4.39) with the help of the crane and the measuring system was turned on.

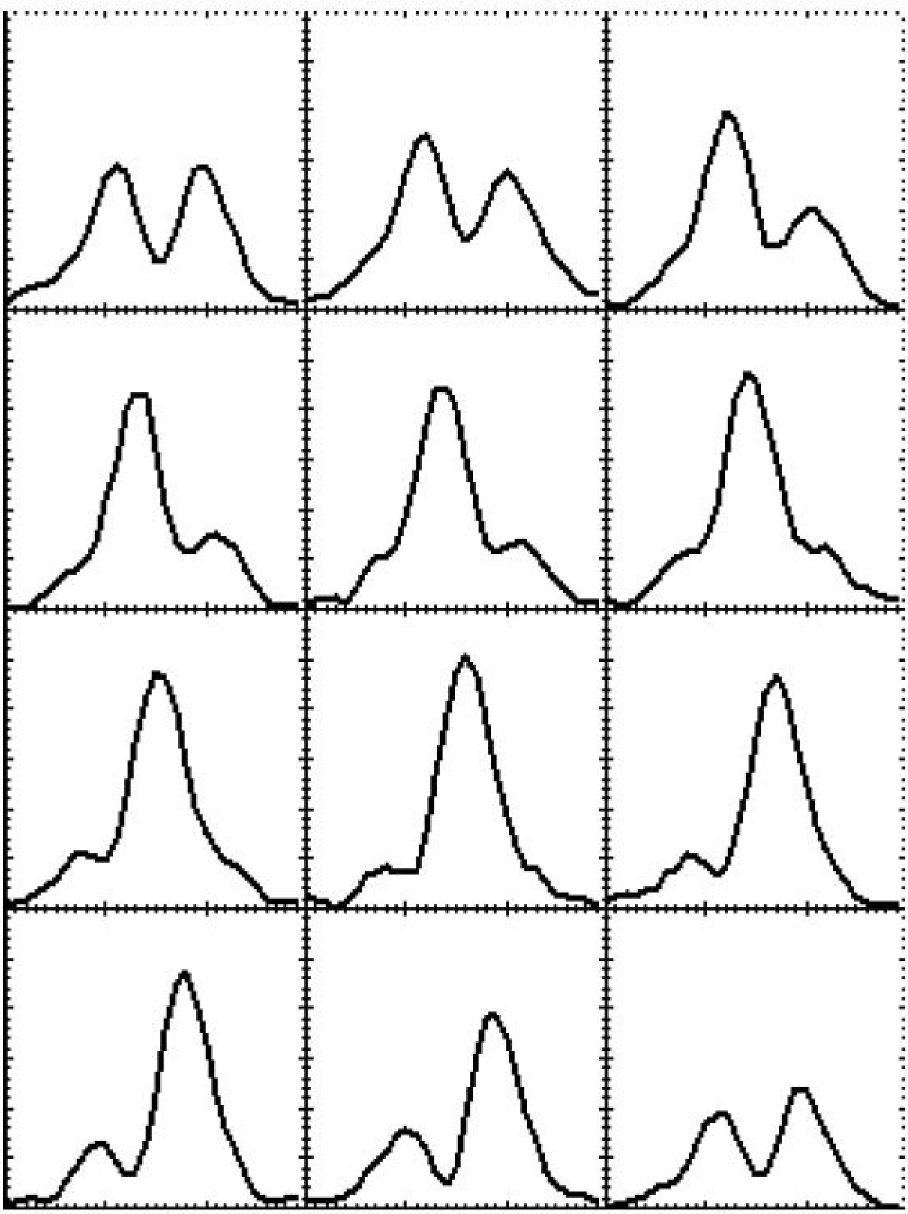

Figure 4.36: Intensity profiles for wavefront piston steps between [-$\lambda/2$, $+\lambda/2$].

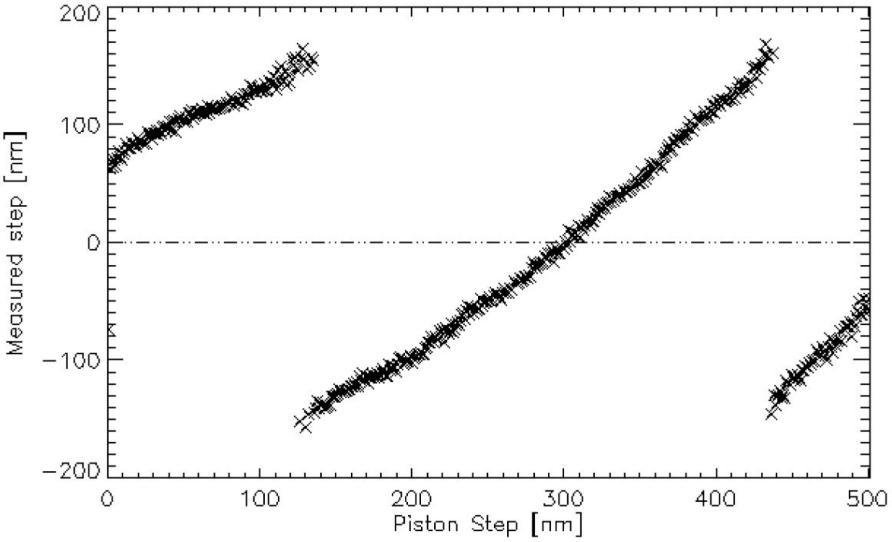

Figure 4.37: Piston step measured with monochromatic light and an aperture of 4 mm in diameter.

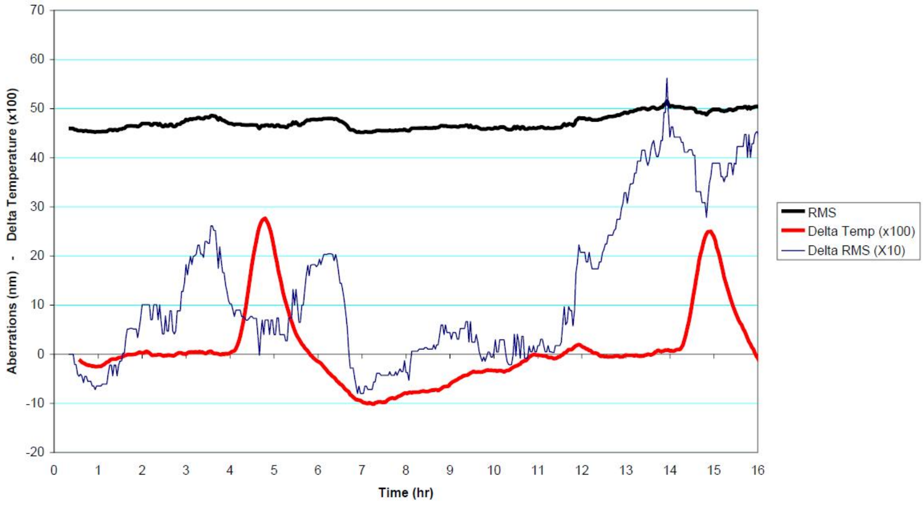

Figure 4.38: Stability of the cavity and laboratory room

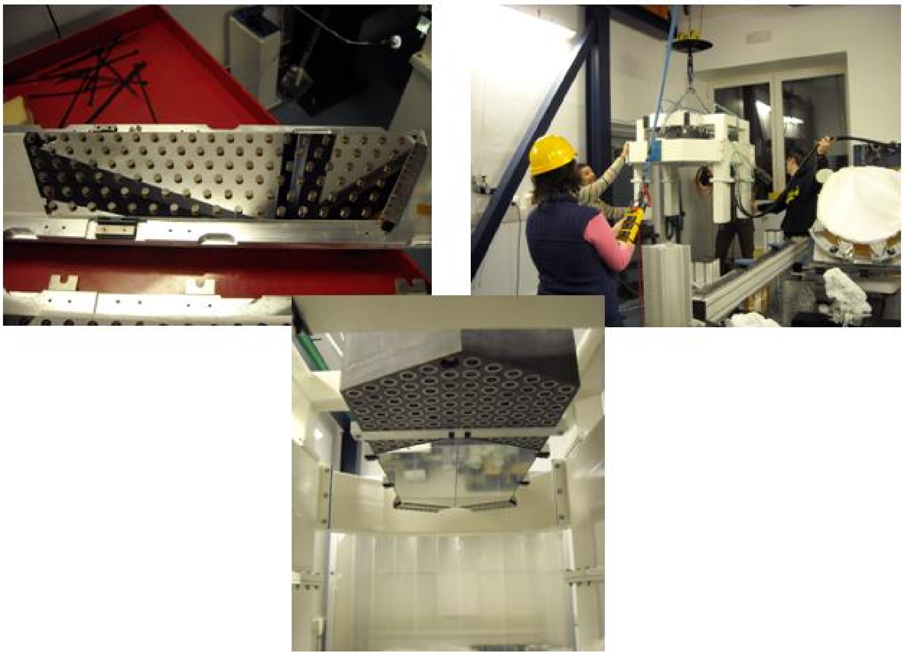

Figure 4.39: Some picture of the integration of the DP

Chapter 5

Test Report

This section describes the tests performed on the DP by mean of the optical test systems described in the previous chapter.

The procedures related the alignment and calibration of the optical bench have already been described.

Schematically, a step by step series of procedure have been applied:

- the pre-flattening of the shells
- flattening
- cophasing (included tip/tilt and piston) of the two shells
- optical calibration of actuators strokes
- application of first 20 Zernike modes
- temporal stability of calibrations

5.1 Definition

The ***feed-forward matrix*** **F** is a matrix obtained from pure electronic measurement and relates the differential forces Δf applied by the actuators and the capacitive sensor outputs Δp:

$$\Delta\vec{f} = F \cdot \Delta\vec{p}.$$

It is measured setting the system (DP) in the configuration where the forces are minimized and then commanding a set of linearly independent deformations. The feed-forward (FF) matrix can be used to compute the corresponding feed-forward (FF) modes through a Singular Value Decomposition (SVD); the singular values associated with the FF modes provide an ordering based on the rms current required per unit rms displacement. Since there is a linear relationship between actuator current and actuator force these modes are also ordered according to rms force.

In general, given a linear system with a number of actuators equal to *n_act* and *n_sens* sensors, the *interaction matrix* **I** is defined as the operator which transforms the actuator positions ***a*** in the values read by the sensors ***s***:

$$\vec{s} = I\vec{a}$$

where **s** is column vector with dimension *n_sens*, **a** is an *n_act*-dimensional column vector and **I** is an $n\_sens \times n\_act$ matrix. The *reconstruction matrix* **R** is defined as

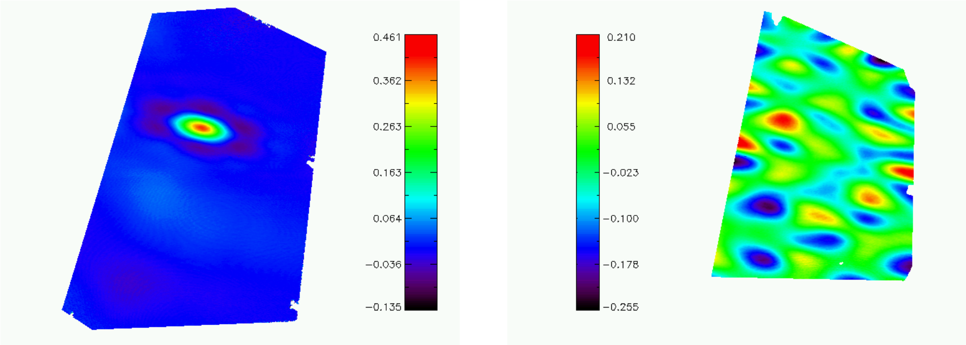

Figure 5.1: Zonal influence function example (actuator num. 49) (left) and modal influence function example (with 76 modes) (right). Units are in μm

the pseudo-inverse of the interaction matrix **I**. It is an $n\_act \times n\_sens$ matrix and it can be used to compute the actuator positions from the values measured by the sensors:

$$\vec{a} = R\vec{s}$$

If the actuator position **a** can be expressed as a linear combination of modes, the modal matrix **D** can be defined according to the following relation:

$$\vec{a} = D\vec{k}$$

where ***k*** is the vector of the mode coefficients. The *modal interaction matrix* **M** is:

$$M = I \times D \Longrightarrow \vec{s} = M\vec{k}$$

The pseudo-inverse of M is the modal reconstruction matrix

The ***zonal influence function*** is the function that links the area affected by the motion of a single actuator to move the actuator. Figure 5.1 left, shows an example of zonal influence function. The actuator *n* has been moved 100nm and this is the typical figure of the influence function. We note the presence of the neighbors actuators.

The ***modal influence function*** is conceptually the same as the zonal influence function, but in this case, instead of moving a single actuator, we use a vector-command corrisponding to orthonormal mechanical modes. To the right of figure 5.1 we can see an example of modal influence function.

5.2 Pre-flattening of the DP shells

At first, shells were set in their most relaxed mechanical mode, as measured through purely electro-mechanical (EM) measurements. Due to relatively large uncertainties (few microns), especially on low modes, after the EM relaxing procedure, large residual shape errors can be expected on the shell surface. Moreover the chosen design for the shell clamping system with its membrane (however not representative of the final one) induced large residual stresses near the membrane area. Such initial surface shape saturated the capture range of the interferometer in RCT setup, as shown in figure 5.2 on the left. After the flattening procedure, shell WFE was put within the capture range of the RCT setup (right side of figure 5.2).

First attempts to flatten the shell were based onto an iterative procedure, with the acquisition of the zonal influence functions (see the next subsection for more detail) over the visible area, and the application of the correction. After each step, a slight larger area begun to be visible by the interferometer, and the procedure started again.

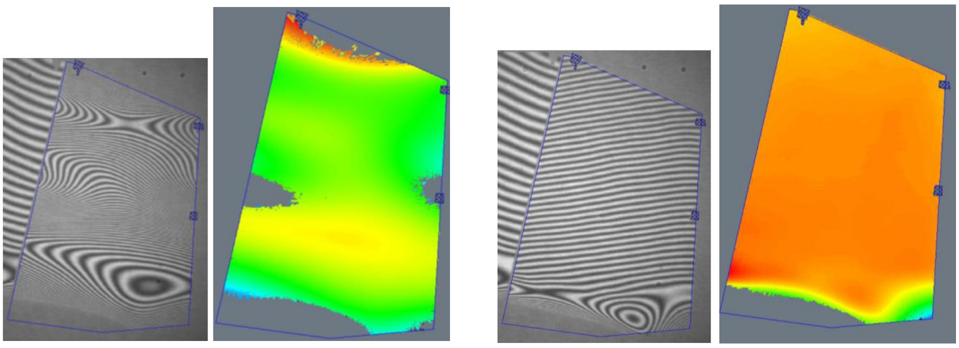

Figure 5.2: Fringes and reconstructed OPD before (left) and after flattening (right).

However, the iterative process converged very slowly. This led us to setup a new procedure to remove these large surface aberrations.

Due to its larger capture range, a stitching setup was used to get full maps of the shell surface.

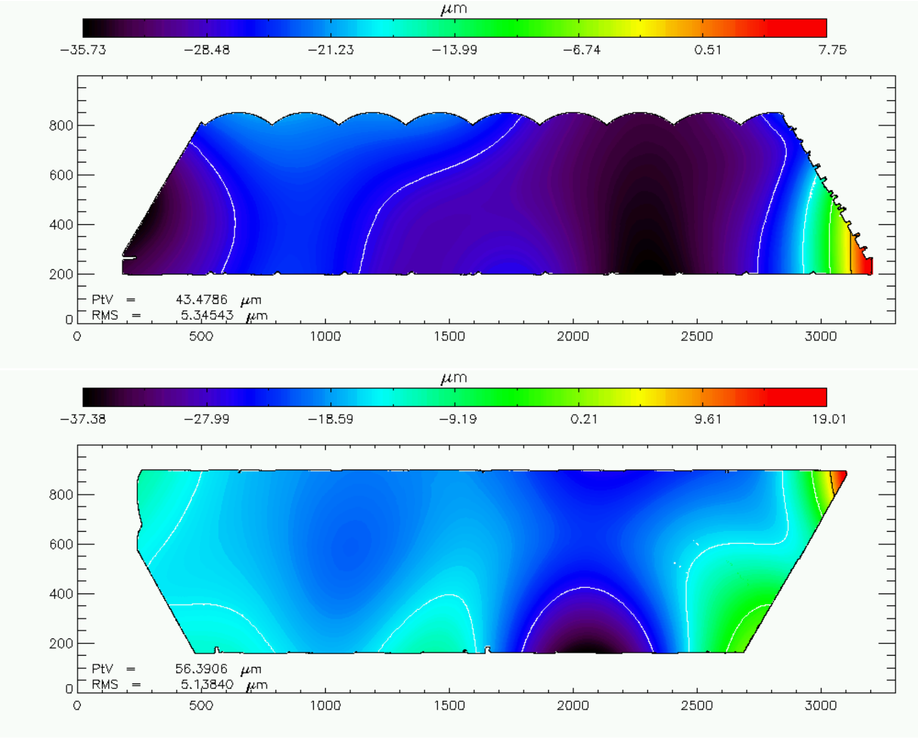

Figure 5.3: Surface maps of the two shells (DX on top, SX on bottom) after E.M. flattening. The right side is near the membranes.

Figure 5.3 shows the reconstructed surface maps of the two shells after EM flattening (i.e. the flat command calculated without optical feedback). The measured surface error ($SE = 0.5 \cdot WFE$ because the surface under test is a mirror) was about $5 \mu m$ (rms), and only areas near the membranes were strongly curved. From these maps, a correction command was applied on each actuator, filtered via electro-mechanical (EM) modes. This filter was particularly useful to keep actuator forces below a given threshold, because the membrane areas were quite stiff and a full correction was not possible there.

Few iteration loops (i.e., measurement of surface map via SIS, followed by the correction command computed on the measured map) were required to converge below 100 nm (rms) over the whole area (excluding the area near the membrane).

Figure 5.4 gives the surface map over the whole shell area. The greatest contribution of rms is given by the areas close to the membrane. If we mask these areas, both shells were quite flat, as seen in figure 5.5.

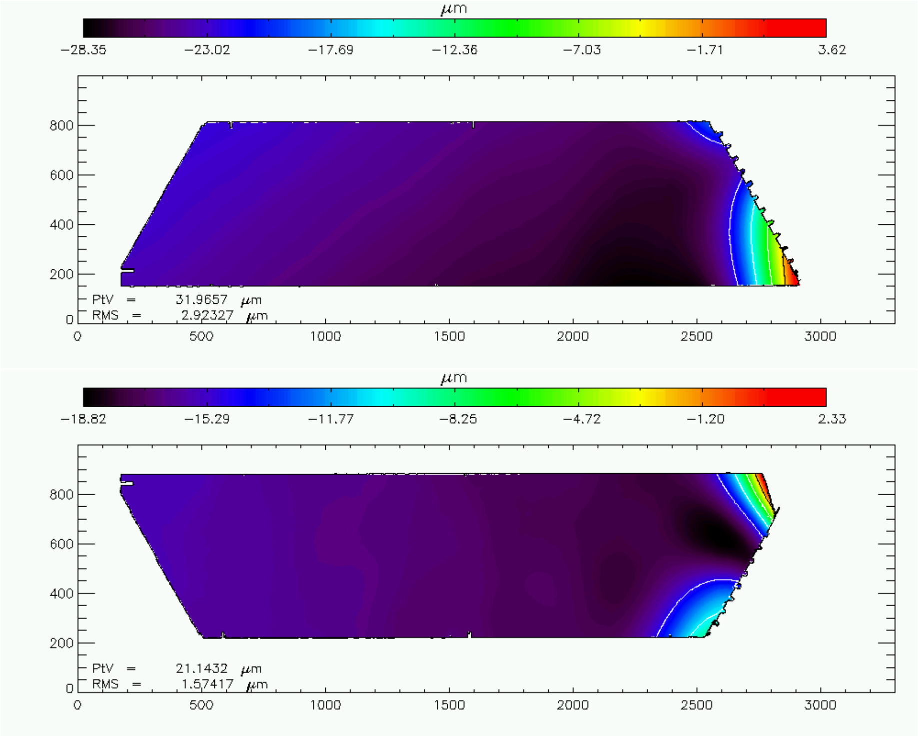

Figure 5.4: Surface maps of the two shells (DX on top, SX on bottom) after pre-flattening.

Below 100 nm rms, SIS uncertainties (due to miscalibration of the cavity error, spatial scale, and misplacement of the different sub images) started to become not negligible. However, such flatness level was well within the RCT capture range. Then, modal influence functions were measured and the initially foreseen flattening procedure started, now working over the full shell area, making it very reliable.

As it can be seen from figures 5.3 and 5.4, the area located near the membranes was relatively highly distorted, and even after a flattening attempt, it was not possible to completely restore the flat shape. This can be easily explained, due to the particular design and implementation of this retaining system. Glass shells were glued without any optical feedback of the real surface shape.

Then, due to the mechanical design of the clamping system, the area near this metallic clamp was stiffened quite a lot, reducing the ability of the actuators to correct for such effect. However, this clamping system is not representative of the final one (on board M4), and no special concerns must be extrapolated about this particular issue.

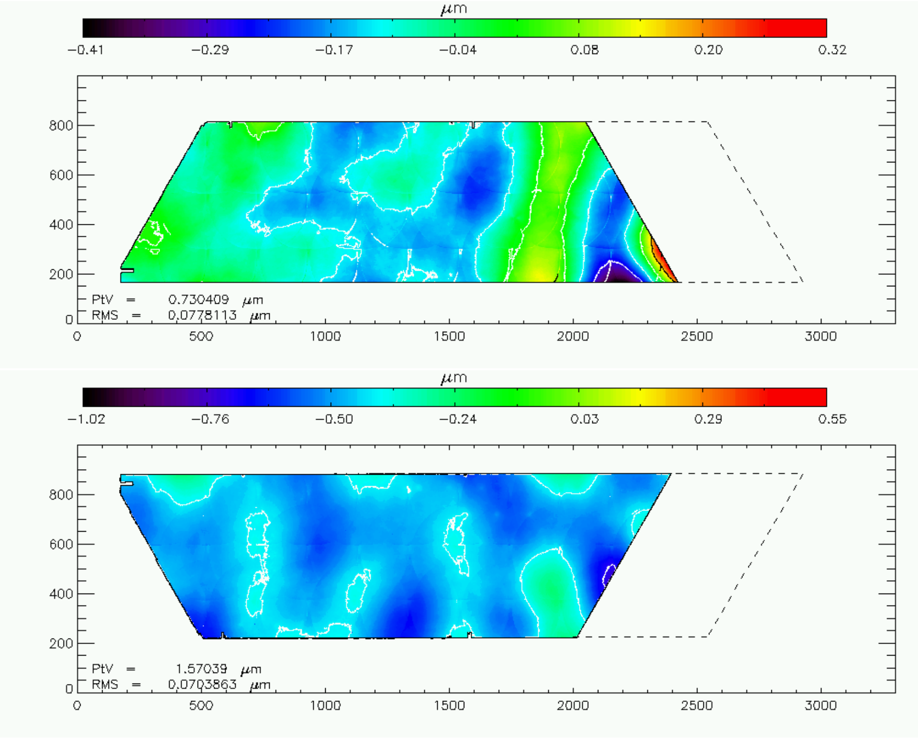

Figure 5.5: Surface maps of the two shells (DX on top, SX on bottom) after pre-flattening, excluding the area near the membranes.

5.3 Influence functions

Both zonal and modal influence functions were measured, being the main setup towards the flattening of the shells. To make full area measurements, RCT was preferred. However, as explained RCT added additional disturbing effects onto the measured DP surface shape (or WFE), like the distortion of the surface map and the differential optical gain between WFE_{RCT} and WFE_{EELT}.

We deliberately decided to not remove these effects from the flattening computation pipeline, because such steps should add noise and spurious effects along the measurement process. As long as the optical setup is fixed, no changes happen to these effects, and they are effectively removed during the computation steps. This is true because at each shell position both distortion and the gain factor are fixed and will be easily factored out. Some examples are shown in the following sections of the measured influence functions. Please note that no real flattening is required during such process, because it is a differential measurement.

In the case of zonal (modal) functions, two identical delta-commands are applied on each actuator (EM mode), with opposite signs, in order to compute the effect of that actuator (mode).

If A is the $-\Delta$ command and B is the $+\Delta command$, the influence function is:

$$IF = \frac{B - A}{2}$$

5.3.1 Zonal Influence Function

Zonal influence functions were measured just after the pre-flattening procedure. They were measured on one shell only, because they are very time-consuming, and possible drifts both on the DP system or in the optical setup could impinge on the accuracy of the influence functions. Figure 5.6 shows few selected zonal influence functions, both at the edges or in the center of the shell area.

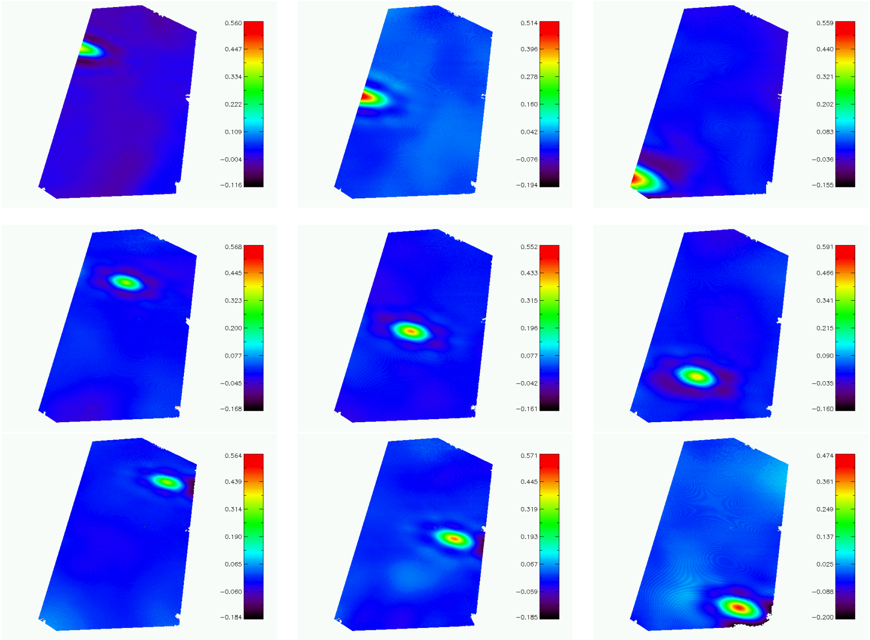

Figure 5.6: OPD maps of selected zonal influence functions for different actuators. The same delta-command was applied on each actuator. Units are wavelengths. Distortion and gain factors vary along the DP surface.

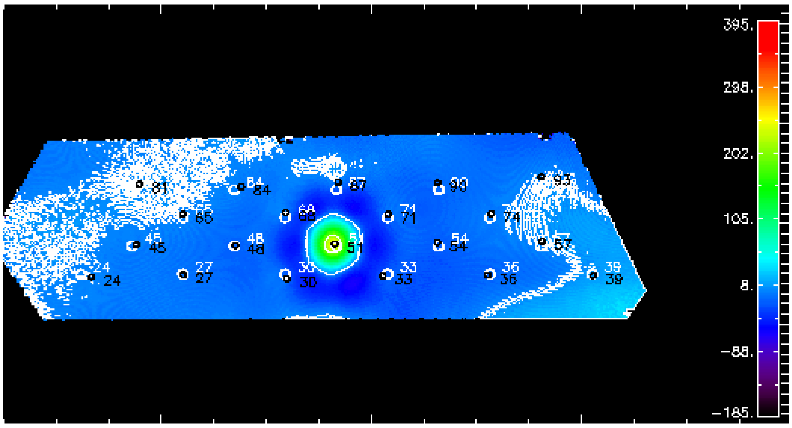

Figure 5.7: Undistorted WFE map of the zonal influence function. Units are nm.

Zonal influence functions extend over an area as large as the first ring of actuators around that actuator. Sometimes, noise far away from the selected actuator is present, and this led to further noise in the interaction matrix computation. A small mask was applied near the membrane area, to maximize the number of visible actuators.

After RCT transformation laws (see Figure 5.7), we extracted stiffness at the peak of the measured influence functions, to be compared with those ones measured via FEA models. Only internal actuators were taken into account. For them, FEA model gave a peak value of $2.86N/\mu m$. Table 5.1 summarize results. Values of the both optical and electrical motions are given in the table (CapSens and Optical). Stiffness was computed as the ratio between measured differential stroke (in motion) over the measured differential force.

On average, measured influence functions were only 6% lower than computed. Moreover, there is a systematic negative difference between the stiffness computed through optical (i.e., the interferometer) measurements and electrical (i.e. capsens) ones. Indeed, capsens measures shifts over a circular ring centered onto a single actuator, far from the peak, thus being smaller.

A large scatter was observed in the data, partially due to uncertainties in the transformation law or in the calibration of the force reading (electrical measurements). Forces were not calibrated for all the actuators, but only on a small subset, and then applied on all the others. However, even if high uncertainties can be present on single actuators, this is not true anymore on average.

Table 5.1: Measured Influence Functions vs. electrical and model values.

NAct	**CapSens**	**Opt**	**F**	$Stiff_{EM}$	$Stiff_{OPT}$	**Relative stiffness variation (OPT/EM)**	**Relative variation (OPT/FEA)**
	m	m	N	N/μm	N/μm		
24	1,94E-07	1,99E-07	0,6481	3,35E+00	3,26E+00	-3%	14%
27	1,95E-07	1,95E-07	0,6021	3,08E+00	3,09E+00	0%	8%
30	1,99E-07	2,55E-07	0,6964	3,50E+00	2,73E+00	-22%	-4%
33	2,02E-07	2,47E-07	0,6265	3,11E+00	2,54E+00	-18%	-11%
36	2,06E-07	2,50E-07	0,5866	2,85E+00	2,34E+00	-18%	-18%
39	1,99E-07	2,75E-07	0,9325	4,69E+00	3,39E+00	-28%	19%
45	1,78E-07	2,10E-07	0,7423	4,17E+00	3,53E+00	-15%	23%
48	1,98E-07	2,44E-07	0,6899	3,48E+00	2,82E+00	-19%	-1%
51	2,04E-07	2,36E-07	0,8276	4,06E+00	3,51E+00	-13%	23%
54	2,11E-07	2,60E-07	0,6682	3,17E+00	2,57E+00	-19%	-10%
57	1,98E-07	2,71E-07	0,6488	3,28E+00	2,40E+00	-27%	-16%
65	2,01E-07	1,87E-07	0,6573	3,27E+00	3,51E+00	7%	23%
68	2,02E-07	2,35E-07	0,7752	3,84E+00	3,30E+00	-14%	15%
71	2,00E-07	2,35E-07	0,6466	3,24E+00	2,76E+00	-15%	-4%
74	1,99E-07	2,45E-07	0,7509	3,77E+00	3,07E+00	-19%	7%
81	1,97E-07	1,61E-07	0,5899	2,99E+00	3,68E+00	23%	28%
84	2,00E-07	1,75E-07	0,6240	3,12E+00	3,57E+00	14%	25%
87	2,02E-07	2,32E-07	0,6281	3,12E+00	2,70E+00	-13%	-5%
90	1,99E-07	2,26E-07	0,6786	3,41E+00	3,00E+00	-12%	5%
93	1,99E-07	2,14E-07	0,5876	2,95E+00	2,75E+00	-7%	-4%
			Average	**3,42E+00**	**3,03E+00**	**-12%**	**-5,8%**

5.3.2 Modal Influence function

Modal functions were measured on both shells, being the preliminary step towards final flattening of the shells. Due to the quite stiff area near the membrane, where flattening was not considered feasible, a relatively large optical mask was applied to cover the first three columns of actuators near the membrane. Some preliminary attempts were done to flat that area, but larger forces were required, exceeding the given threshold of 0.1 N per actuator (i.e. the 10% of the total actuator stroke).

Figure 5.8 and Figure 5.9 show the modal influence functions of the shell SX, for the first 18 modes and for higher modes, respectively. Modes in Figure 5.9 range from 18 to 107 with steps of about 5.

Figure 5.10 and Figure 5.11 show the same on the shell DX. Measurements of the lower modes on this shell suffered from increased noise levels, still within a quite low value (<20-30 nm rms on the WFE).

With all the Influence Function (zonal OR modal) we are able to construct the interaction matrix (zonal OR modal) and bind the signal read by the sensors to the actual position of the actuator, in other words we can move from the wavefront map to the vommand vector of actuators.

5.3.3 Flattening of the shell

Once the modal influence functions were acquired, together with the capacitive sensor measurements, the interaction matrix (I or M) of the system was computed. This takes into account the differential reading of capsens and wavefront maps, together with the geometric distortion and the gain factor.

All the SW routine was debugged on the shell SX. In order to enhance the capture range and sensitivity of the RCT system, we aligned the RCT cavity in order to fully illuminate the shell SX. This translated into a quite large incidence angle. Typical values range from 60 to 65 deg when measured in the center of the shell. As result, the average conversion factor between the measured WFE and the DP surface shape (i.e. DP_{WFE}) was 1.0 and 1.2 for the two given angles, respectively. Figure 5.12 shows the fringes as captured through the RCT cavity at the first successful flattening and after some refinements.

The residual DP_{WFE} (average AoI 60 deg, conversion factor 1.0) were ***21 and 14 nm rms***, respectively. Masks are used to get out the area near the membrane (highly distorted) and small areas along the edges where safety fingers were placed. Some iteration loops of modal influence function measurements and the flattening procedure were required for such a refinement.

Figures 5.13 and 5.14 show the wavefront maps of the two shells after the first flattening. The rms of shell SX is 21 nm, shell DX is 23 nm. Figure 5.15 and 5.16 show the DP WFE map (average AoI 60 deg, conversion factor 1.0) and the force map as measured on the actuators of the flat area on shell SX and DX, respectively, after the refinement of the flattening process.

Figure 5.17 shows the convergence process of PtV and RMS WFE as function of the iteration loop. As it can be noticed, WFE rms cannot be reduced below the threshold of 10-15 nm rms. The main reasons are the residual errors during the acquisition process (turbulence and vibration bumps due to the refrigerating chiller), and to the poor control gain of the DP Control System.

5.4 Flattening over small sub-apertures

One of the requirements was to reach an even better flattening on sub-apertures smaller than twice the inter-actuator pitch. Figure 5.18 gives the WFE maps (units: nm rms)

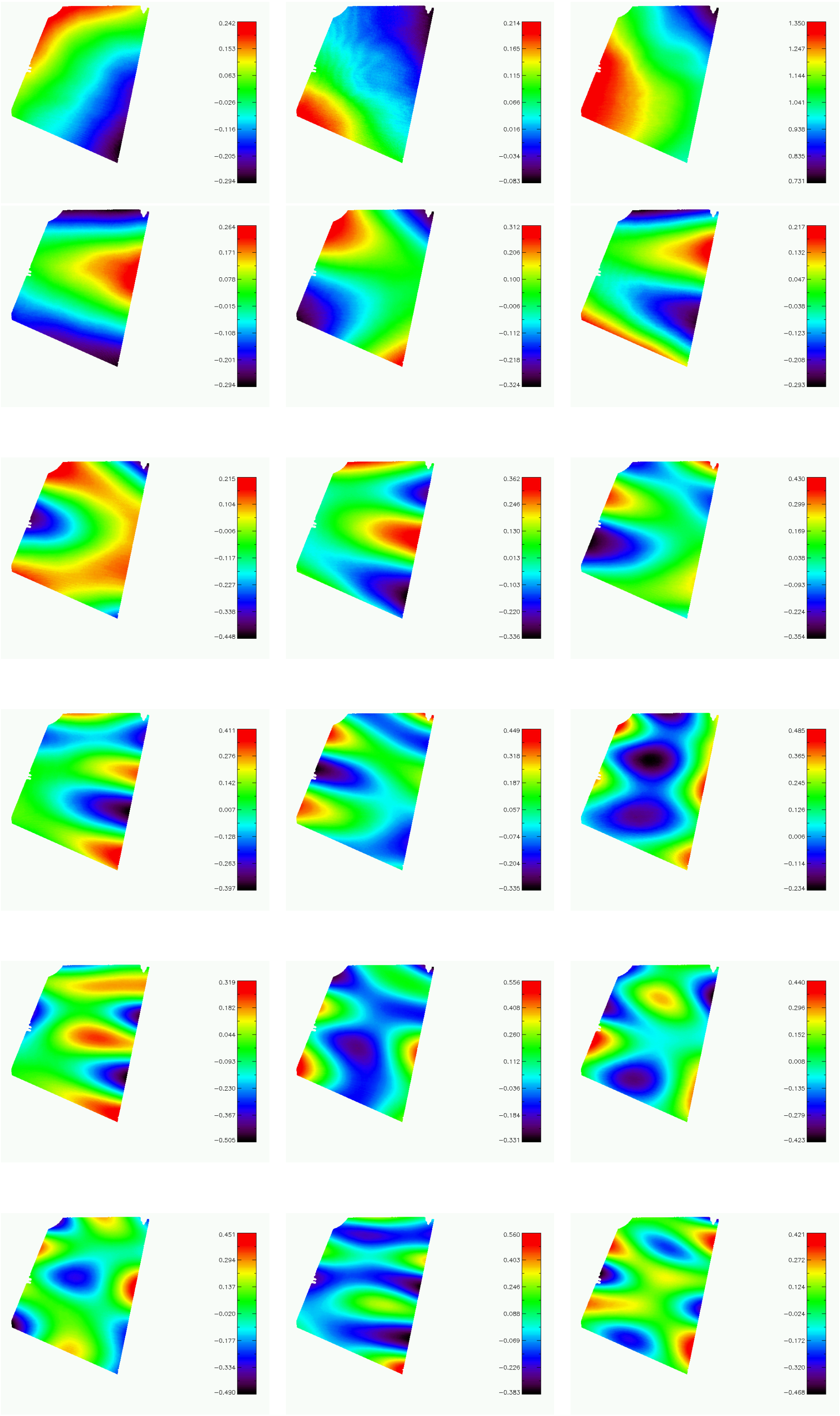

Figure 5.8: OPD maps of first modal influence functions on the SX shell. Units are wavelengths.

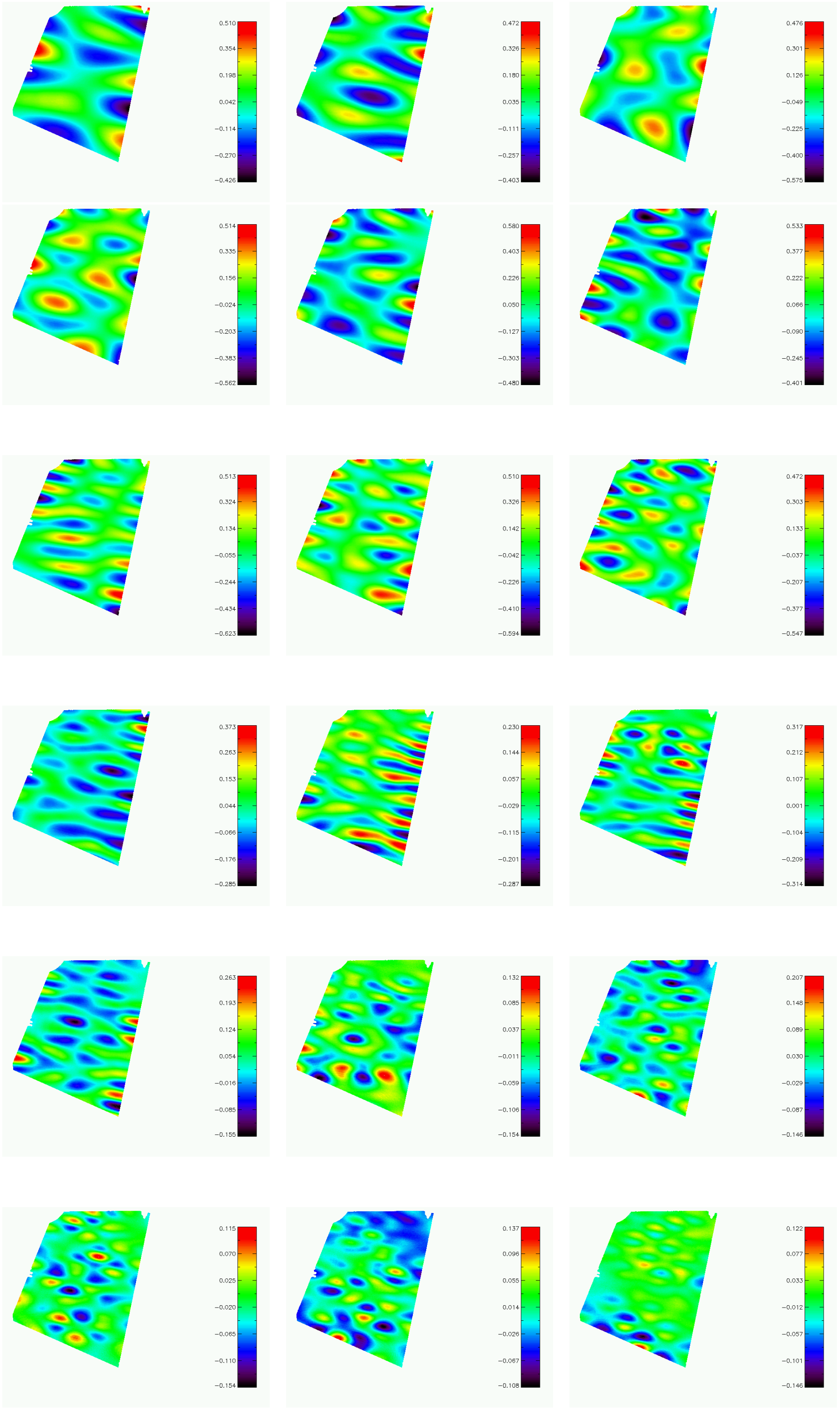

Figure 5.9: OPD maps of mid-high (18-107) modal influence functions on the SX shell. Units are wavelengths

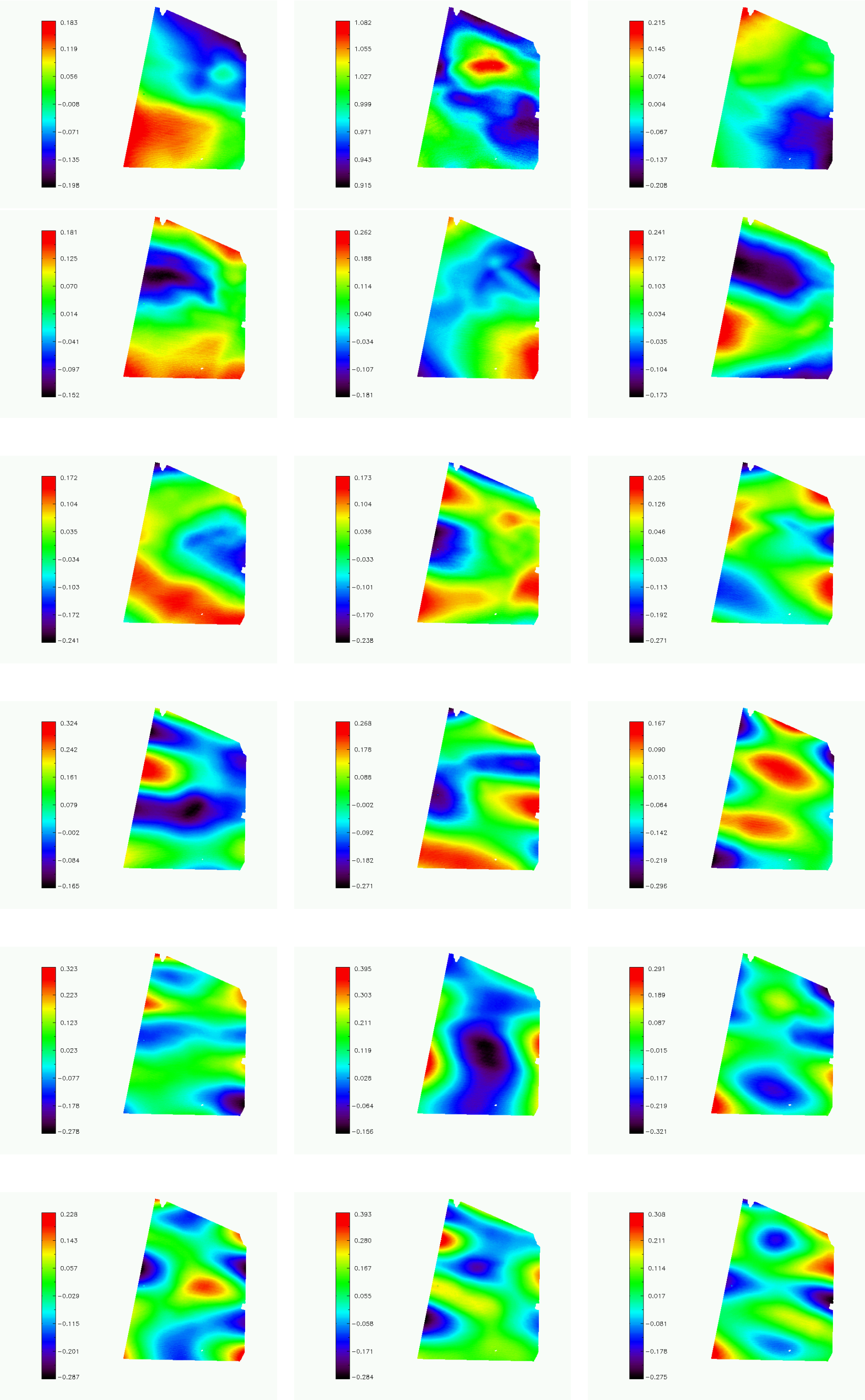

Figure 5.10: OPD maps of first modal influence functions on the DX shell. Units are wavelengths.

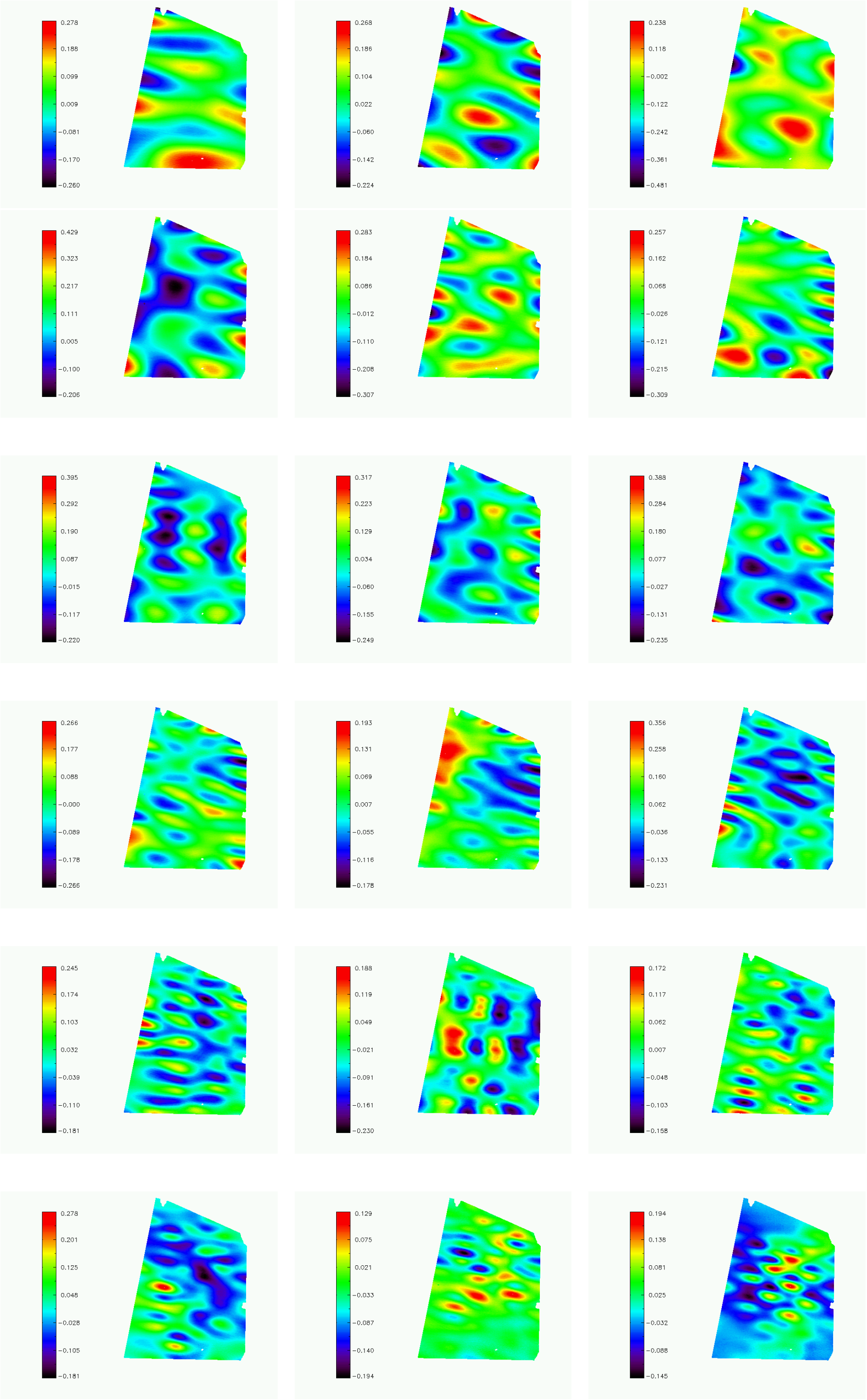

Figure 5.11: OPD maps of mid-high (18-107) modal influence functions on the DX shell. Units are wavelengths.

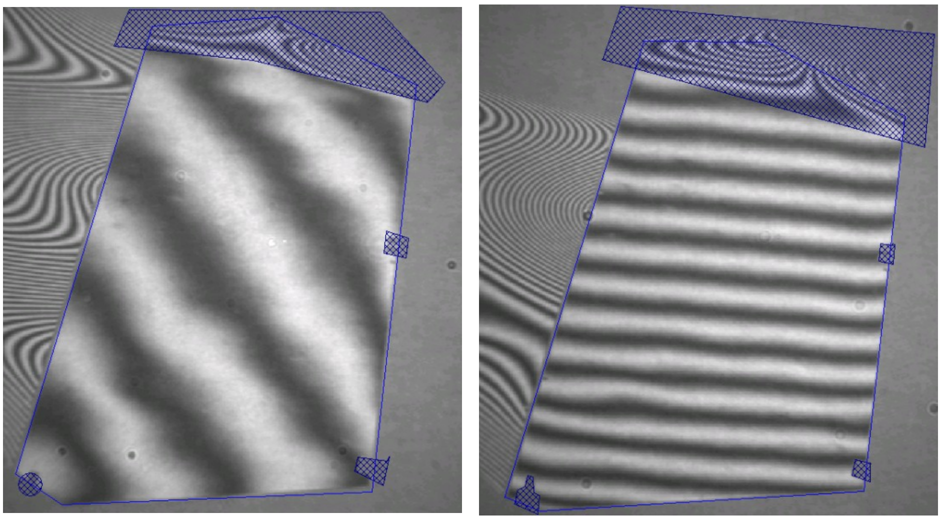

Figure 5.12: Fringes of the shell SX after first successful flattening (left) and some refinements (right).

computed on 60x60 mm sub apertures, scanning over the shell area. Measurements were done under RCT setup (average conversion factor = 1). Specifications are met over $> 90\%$ of the shell area. As seen from the two maps in figure 5.19, only few areas near the membrane are out-of-spec (WFE >15 nm rms). The standard deviation of the WFE (rms) is 9 nm ± 7 (1σ).

5.5 Optical calibration of actuator stroke

Before final flattening and removal of differential piston and tip/tilt, we performed the ***optical*** calibration of the actuator strokes. All the preliminary steps (pre-flattening, influence function measurements, flattening of individual shells) were done based onto the preliminary EM calibration of the actuator strokes. Once flat, an optical calibration of actuator strokes was possible.

We looked at two different approaches. Measurements were done with the SIS setup, avoiding complexity due to the variable gain of the RCT.

The first is based onto a method developed in Arcetri (see [56]). Small delta-piston commands (<50 nm) are sent to the shell, while acquiring fringes. When calibrated, for a piston equal to $\lambda/2$, fringes will shift on the interferogram by one fringe spacing. These data are used to calibrate the look-up table of the capacitive sensors. Indeed, we realized very soon that two conditions were really essential to perform such a calibration in the proper way: acquire fringes at fast frame rates (>50 Hz), while keeping drifts and noise sources (like air turbulence and vibrations) at a very low or negligible level. This was not possible in our setup due to the low frame rate of the frame grabber.

A new method was developed. A series of delta-piston commands of $\lambda/2$ were sent to the shell. When calibrated, no drifts of the local fringes are expected between two consecutive steps. Small drifts will be a measure of the actuator stroke mis-calibration and can be used at each step to correct for such a miscalibration. After some trials, the routine was robust enough to provide good calibration curves. This method was 10X faster then the original one, reducing the effects of noise, drifts, and turbulence. This procedure was repeated on each visible actuator between -10 and +10 μm, starting from the flattening command of each shell. Comparing optical and EM calibrations curves we observed that the main effect was a simple gain factor between the two calibrations.

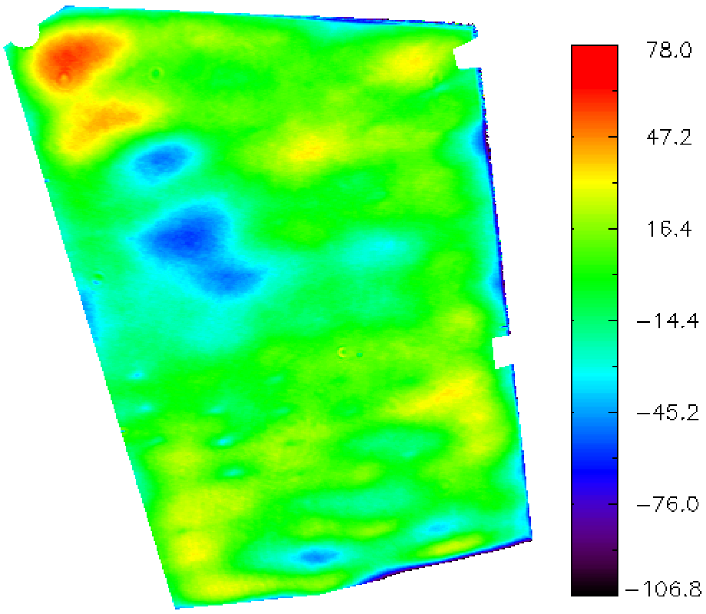

Figure 5.13: WFE maps (average conversion factor = 1) of the shell SX after first successful flattening. Units are in nm

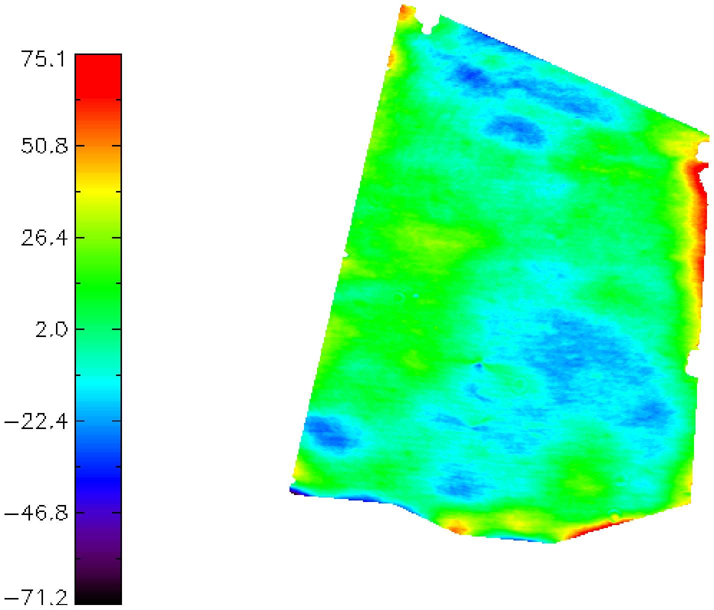

Figure 5.14: WFE maps (average conversion factor = 1) of the shell DX after first successful flattening. Units are in nm

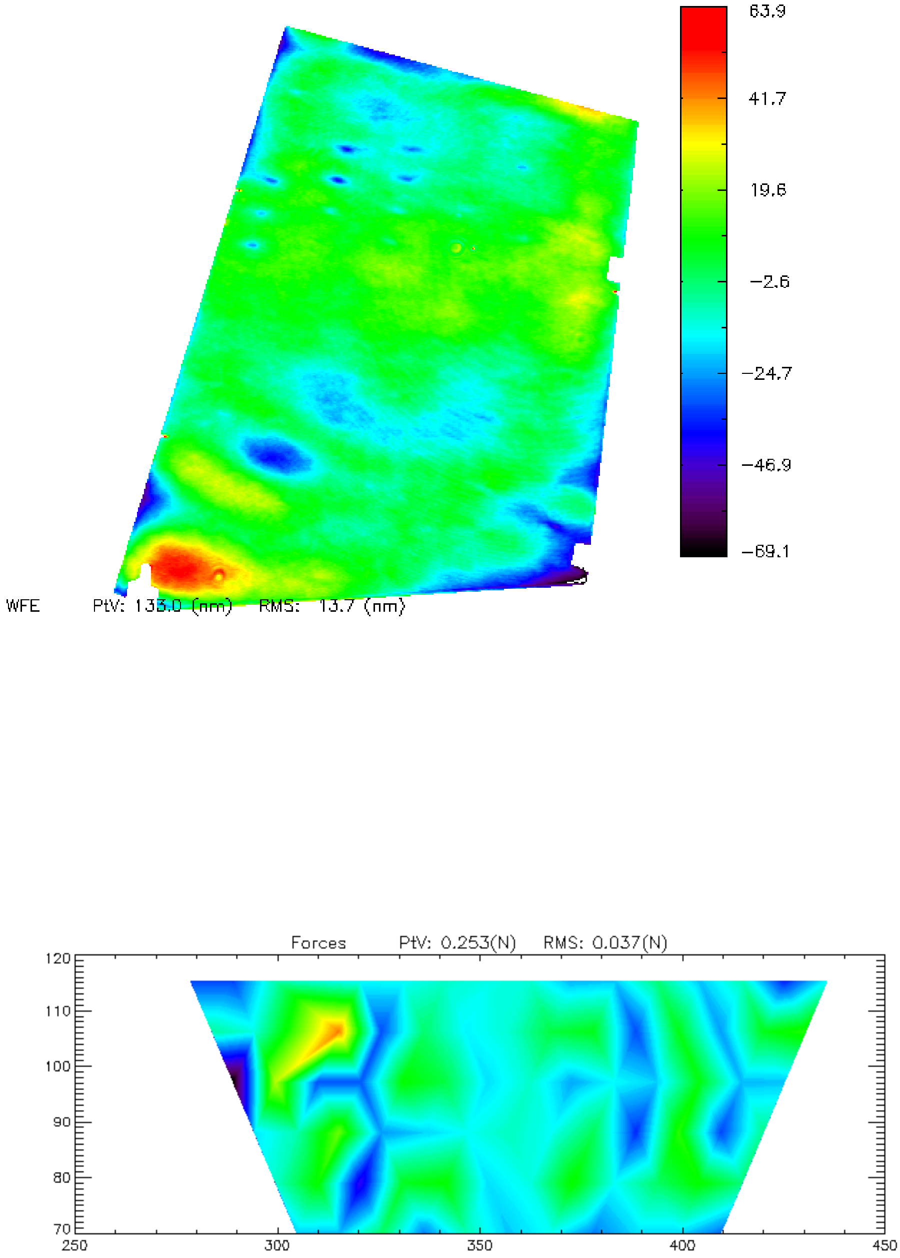

Figure 5.15: WFE map (top, units are nm) and force map (bottom) of the shell SX after refined flattening.

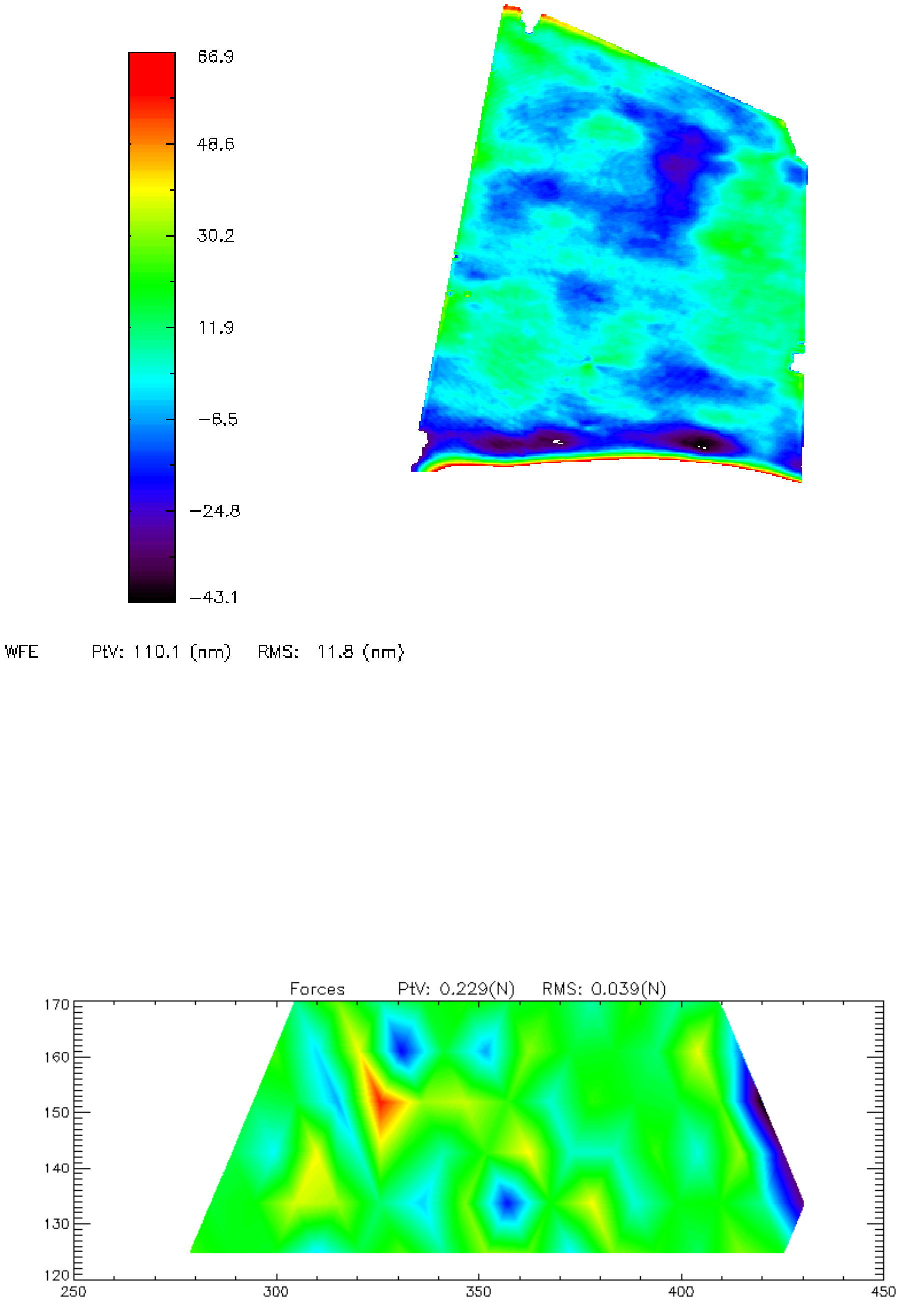

Figure 5.16: WFE map (top, units are nm) and force map (bottom) of the shell DX after refined flattening.

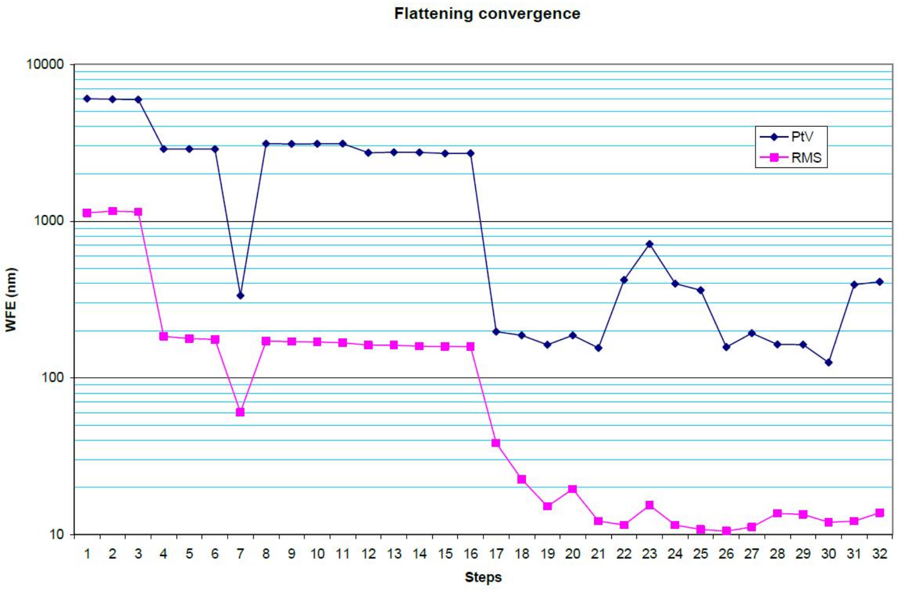

Figure 5.17: Convergence process during flattening of one shell (average conversion factor = 1).

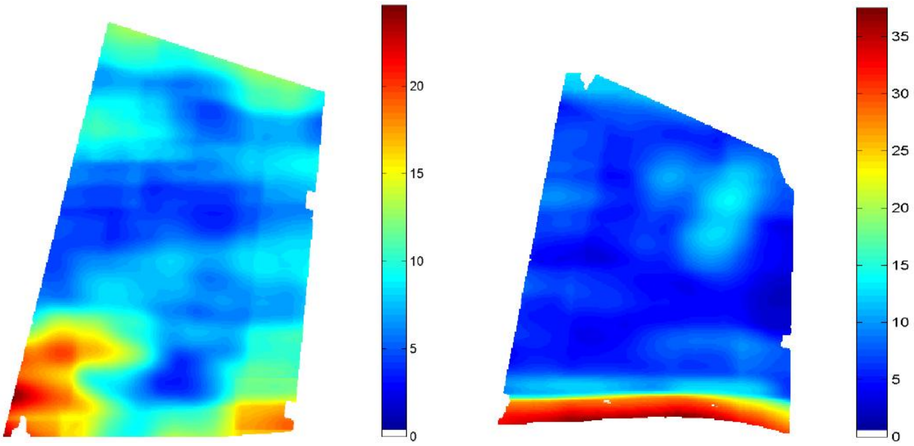

Figure 5.18: WFE maps on 60x60 mm sub-apertures scanning the shell area. Left: SX shell, right: DX.

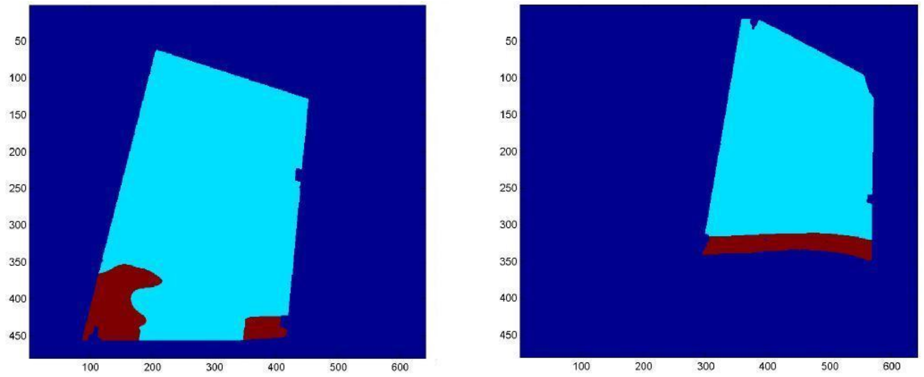

Figure 5.19: Same image as before, but showing the area below (or above) 15nm WFE in blue (or red). For both shell 90.6% of the sampled are is within the given limit.

Such factor differs per each actuator within $\pm 15\%$ with respect the preliminary EM calibration. Figure 5.20 shows the value of the calibration coefficients. Also maps are given, showing that such a wrong calibrations seems to be correlated to low-order modes.

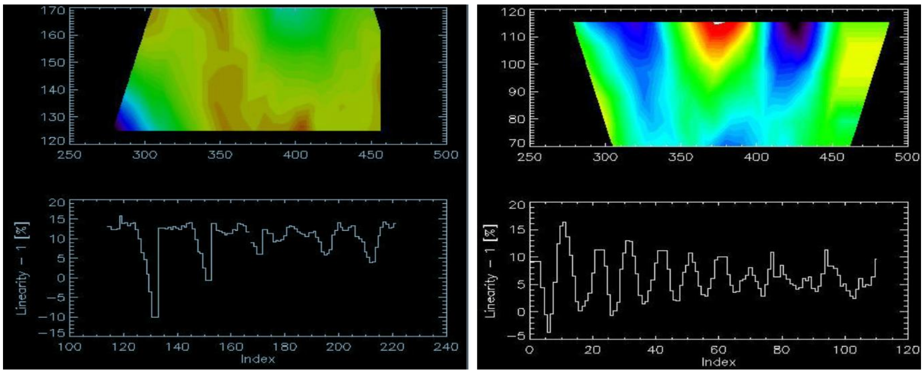

Figure 5.20: Calibration coefficients of the shell actuators.

After recalibration, we checked that even relatively large piston commands ($\pm 10 \mu m$) led to almost flat shape, introducing WFE <100 nm rms. More iterations of the calibration procedure, to be performed after correction for the differential piston and tip/tilt, can enhance this result, but time constraints led us to skip this step.

5.6 Co-phasing the shells

Co-phasing the two shells was achieved through the Piston Sensor Unit (PSU), looking onto the shell gap. Two preliminary steps were done: quality check of the edges near the gap, and removal of the differential tilt between the two shells.

5.6.1 Check of the edge quality

Shell edge quality was measured by SAGEM just after the cut from the monolithic circular shell, and checked again with our SIS setup with a high resolution spatial scale. Figure 5.21 shows two interferograms of the gap located near and far from the membrane. Fringe contrast is very high (i.e., fringes clearly seen) down to the edge.

Due to the selected high spatial scale (using the zoom capability of the interferometric head), with a pixel scale <0.1 mm/pixel, we can estimate no edge defects for spatial scales larger then 0.1 mm.

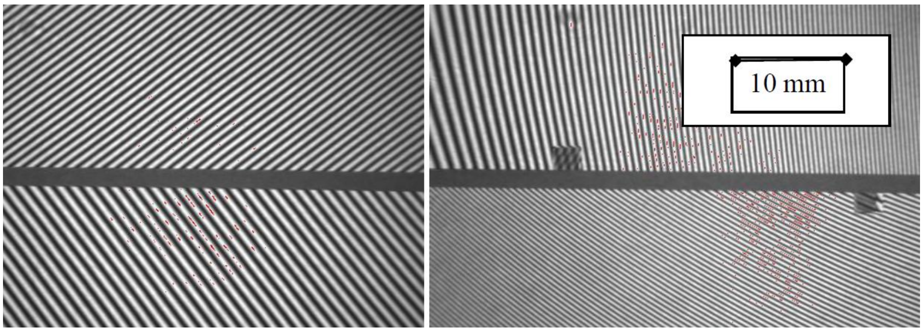

Figure 5.21: Interferograms of the gap between the two shells, far (left) and near (right) the membrane, after the flattening procedure.

5.6.2 Differential tilt subtraction

As it can be easily recognized from interferograms (Figure 5.21), a quite large residual differential tilt was present between the two shells. Such a large differential tilt was measured with both RCT and SIS setups. Both RCT and SIS are sensitive enough to remove this effect. A first attempt was done using the SIS setup. An iterative procedure was drawn, able to measure this differential tilt, and applying a correction to both shells in order to remove it. However such a procedure is able to see only local differential tilts. RCT is much more effective to remove the overall differential tilt over the whole DP area. Then, a second iterative procedure was run, using the RCT setup. As result, we succeeded to remove the differential tilt below a given threshold of **10 nm rms**. Figure 5.22 and5.23 show the interferogram and the OPD map over the two shells after removal of both differential tilt and differential piston (see following section). The measured WFE(EELT) was **19 nm** rms (including the conversion factor).

5.6.3 Differential piston subtraction

An innovative differential piston sensor has been developed as described in the previous chapter section 4.2.3 where also the basic principles of this measurement are fully described. We mounted and aligned the PSU under the DP shell on its support, and few trials were required to reach the best focus and alignment condition, as learned with the piston simulator.

Moving only one of the two shells with delta-piston commands, few scans were done using different filters. A first scan with a broadband (BB) filter, peaked at 650 nm, gave a preliminary rough measurement of the differential piston.

The plot of the peak intensity vs. uncalibrated differential piston position is shown in Figure 5.24. Even on a pretty high bias light level, due to unwanted light, the intensity peak is clearly visible. Differential piston has been estimated at $-3.5 \pm 0.1\mu m$. This is the uncertainty of the first estimate of the differential piston.

A second scan with smaller delta-command steps was done using a narrow-band (NB) filter (600-610 nm), centered around the first estimate of the null-piston position. Figure 5.25 shows only a small selection of measured intensity profiles (intensity vs. position onto the CCD detector of the PSU). Each plot has been recorded at a fixed differential piston position, labeled on top of each plot (units: nm). These plots are the well known diffraction patterns produced by a circular aperture illuminated by a

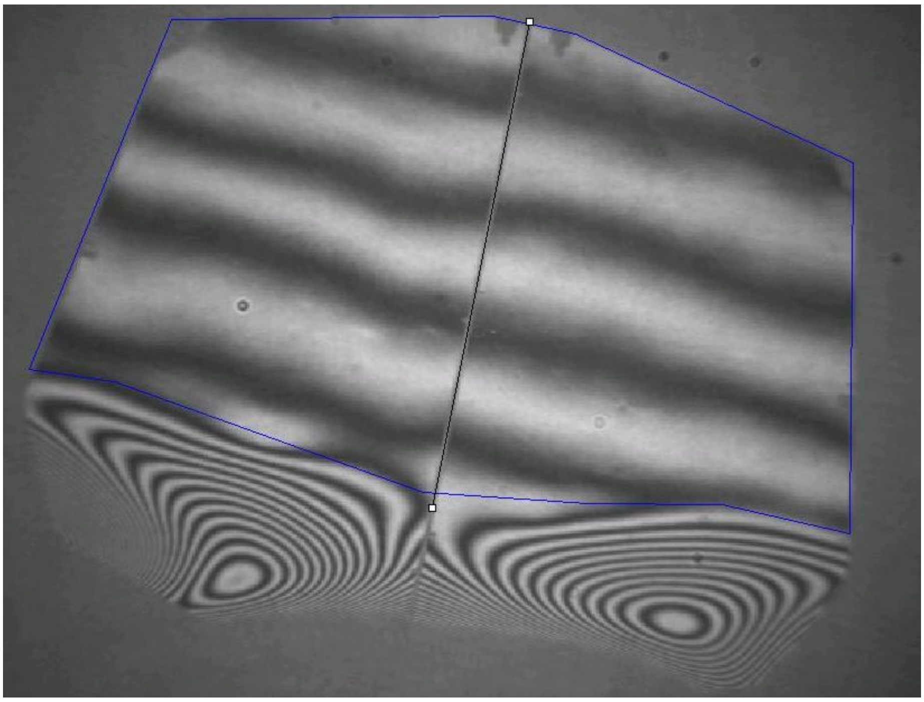

Figure 5.22: Interferogram over the two shell after removal of differential tilt and piston.

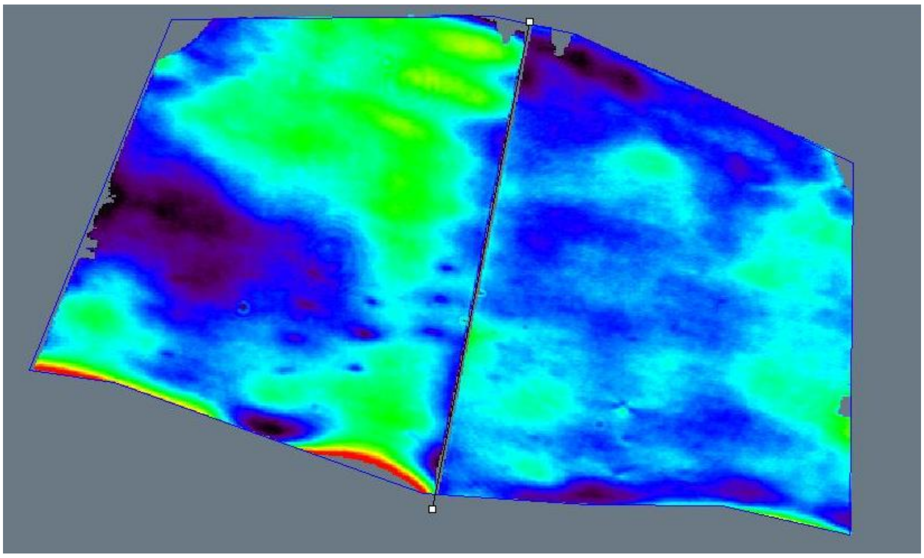

Figure 5.23: OPD map over the two shell after removal of differential tilt and piston.

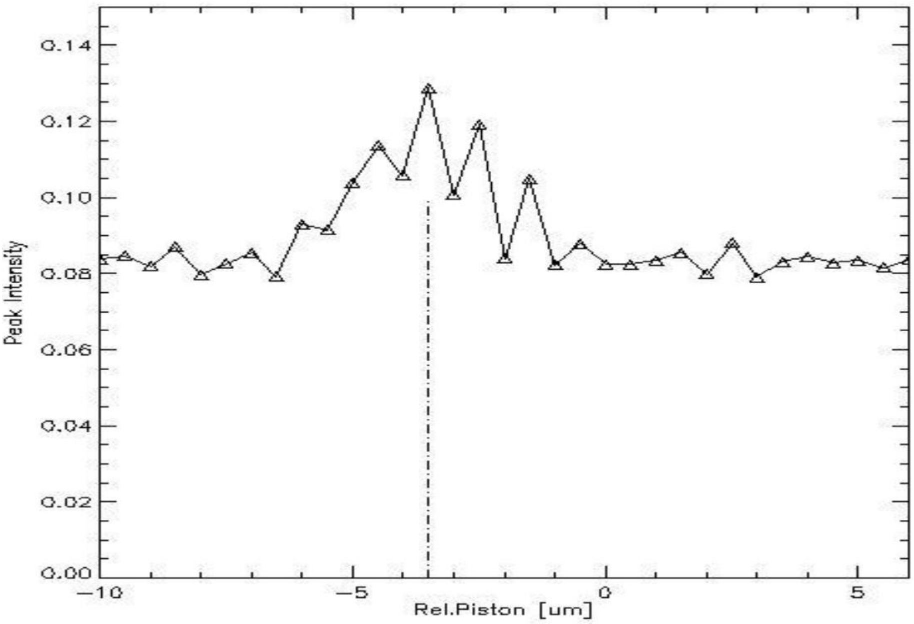

Figure 5.24: Intensity plot of the broadband scan.

collimated monochromatic light. Asymmetries in the secondary peaks are sensitive to the differential piston at a level of few nm. The most symmetrical pattern can be identified as the best condition of null-differential piston. This updated measure of the differential piston was $3515 \pm 15nm$.

Finally, after subtracting the measured differential piston, light of different wavelengths observations was sent to the PSU, making a final scan centered on the best estimate of the null-piston condition. Intensity profiles were recorded.

Figure 5.26 shows intensity profiles at the best null-piston condition. Labels on top of each plot define the kind of filter and its central wavelength: BB=broadband, NB=narrow band, WhiteL = white light, NB_600 means narrow band filter center at 600 nm.

Looking at peak intensity vs. differential piston, all maxima overlap at the same differential piston position (3515 nm), thus proving that this position is not ambiguously determined.

All these steps were performed onto a given position between the gap of the two shells. Then, we can say that the two shells are only locally co-phased. To extend co-phasing to the full shell area, we illuminated the full DP area with the RCT setup. Once within half wavelength (313 nm), the interferometer is sensitive to the differential piston. Then, an iterative process has been applied correcting for the residual differential piston (as measured over the full DP area).

Figure 5.22 shows the interferogram over the two shells after removal of differential piston. As it can be seen, fringes across the gap are continuous, as expected from well co-phased shells. No edge effects can be noticed near the gap. The measured WFE(EELT) was **19 nm rms** (including the conversion factor), thus within given requirements.

5.7 Tip-tilt and Zernike mode commands

These tests were conceived to check the ability of the AO mirror to simulate any shape in open-loop, within a given accuracy threshold, including a tip-tilt mode.

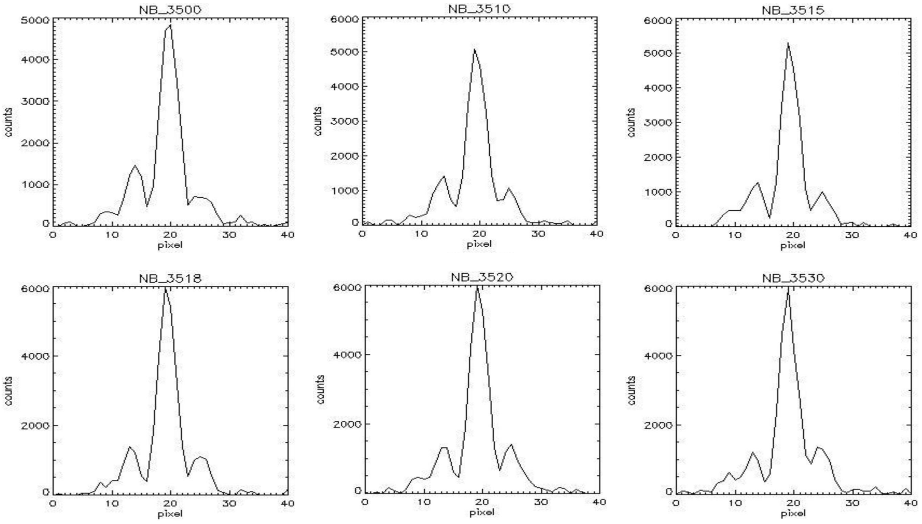

Figure 5.25: Intensity plot of the narrow-band scans, at different differential pistons (labels on top, units: nm)

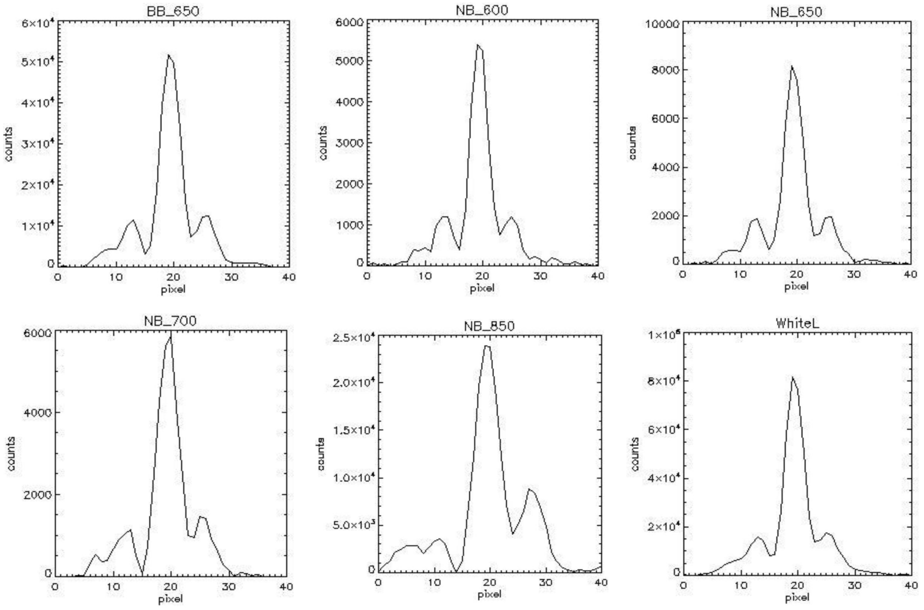

Figure 5.26: Intensity plot of the narrow-band scans, at different differential pistons (labels on top, units: nm)

After flattening and cophasing of the two shells, optical calibration of the actuator strokes, the ability to deliver a given shape is essentially linked to the stability and repeatability of the system. This aspect will be described in the next Section. Here we show results for these two tests. We applied delta-commands starting from the flatteningPLUSco-phasing command. Zernike modes were projected onto the DP shell, considering them as two smaller sub-apertures located near the external rim of the whole M4AU shell, where the effective strokes are larger, in order to be conservative.

Zernike functions (as defined in the Appendix B) were normalized in order to have a given maximum PtV, over the whole M4AU aperture. Figure 5.27 shows few examples of the first Zernike modes, as projected onto the aperture of the DP surface.

Results are given at different maximum PtV values of the delta-commands applied on the DP. These values ranges from -5 to +5 μm (as applied on the whole M4AU), corresponding to wavefront excursion (on the DP) of -10/+10 μm. For each Zernike mode, six different plots summarize results, as shown in the example of Figure 5.28. On the left side of the plot set, three plots give wavefront vs. actuator number, while on the right corresponding maps are given.

From top to bottom, three different values are shown: delta-commands sent to the DPCS (top), measured wavefront shape (middle), and the residual between the two (bottom). All values are converted to WFE units, to be easily comparable. The surface shape was reconstructed from the RCT measurements.

5.7.1 Piston mode

As sub-product of our Zernike test, we obtained also the piston mode, for different piston values. In Figure 5.29 some maps of the residual WFE at different delta-commands are shown. Values of the PtV delta-commands as projected onto the final M4AU. Starting from the left-up this values are: $-8\mu m$, $-4\mu m$, $-2\mu m$, $2\mu m$, $4\mu m$, $10\mu m$. Two runs were made and compared to get information about repeatability of this kind of delta-commands. Results of the residuals are summarized in a graph, together with those ones obtained for TiltX and TiltY modes (see Figure 5.32). As shown, all of them are below the given threshold of 250 nm rms.

5.7.2 Tip/Tilt mode

Tip and tilt modes correspond to the first two Zernike modes after piston. The scope of this test is to check if the system is able to maintain the flat shape in a condition of maximum tilt stroke of the actuators. Figure 5.30 and figure 5.31 show some of these measurements for the Z1 and Z2 modes, respectively. As it can be seen, delta-commands can have an average value different from zero, as expected due to the off-axis portion of the section extracted from the full M4AU surface and represented by the DP (see also Figure 5.27). Of course, once measured via interferometers, this average value that represent a piston term cannot be seen. This is why the other plots have null averages. Figure 5.32 gives a summary plot of wavefront error residuals after tip-tilt delta-commands. As shown, all of them are below the given threshold of 250 nm rms.

5.7.3 Zernike modes

As shown in the previous sections about piston and tip/tilt modes, also all the first 20 Zernike modes were commanded to the DP and measured. Many of them can be seen as an overlap of a piston and tip-tilt command, with a smaller additional term. This is due to the particular choice about the location of the DP area with respect to the final M4AU area (see Figure 5.27). Then, the DP area will “see” only a small fraction of the whole Zernike mode.

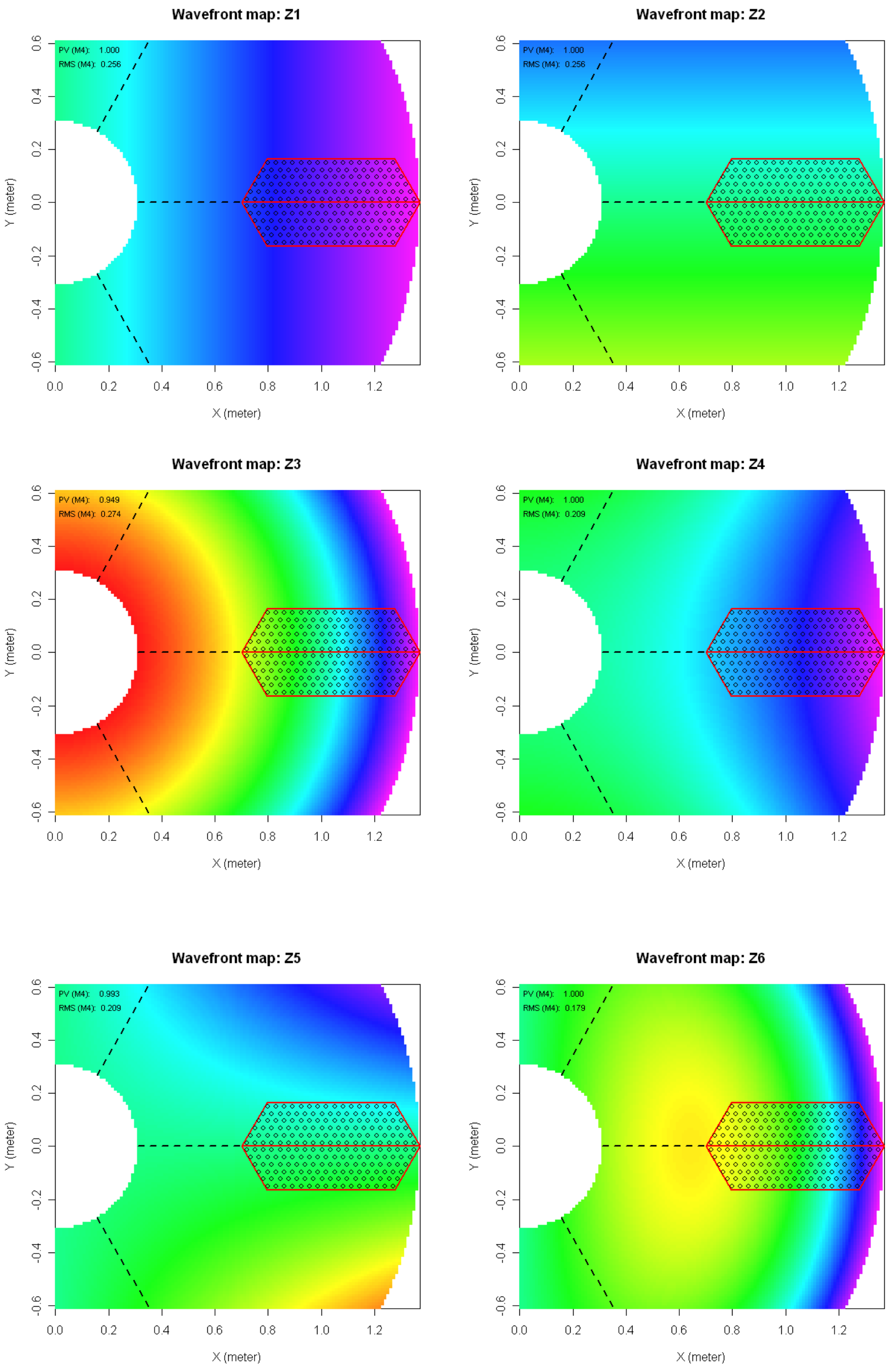

Figure 5.27: First Zernike modes as projected onto the DP surface.

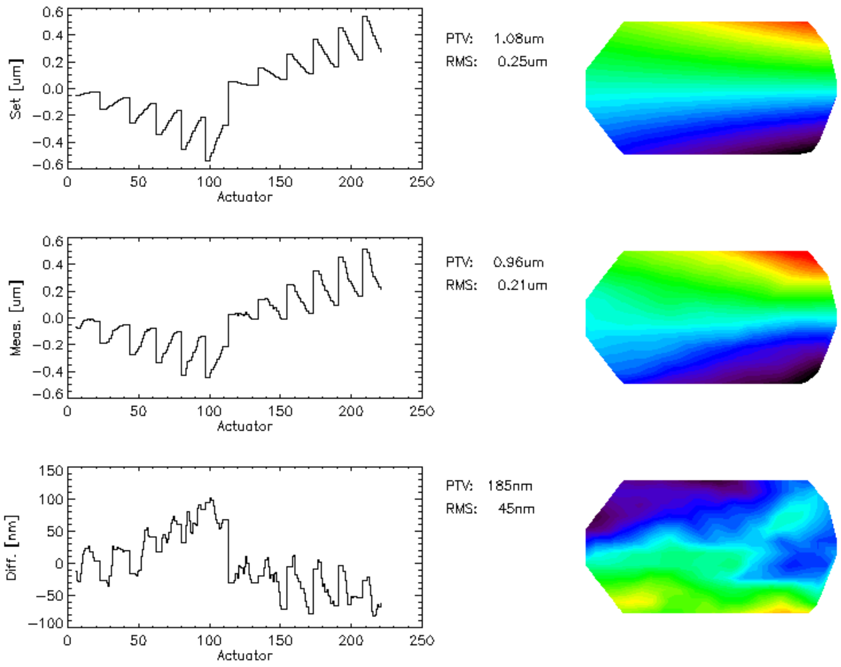

Figure 5.28: Example of Zernike plots (Z11, PtV = $5 \mu m$ on M4AU). Top: delta-command. Middle: measured surface shape. Bottom: residual. Units: nm WFE(EELT) (average conversion factor = 1).

Some measurements were affected by wrong reconstruction of the OPD map along the gap, as result of the unwrapping process that looks at the edges between different islands. When errors due to small drifts near that edge or air-turbulence, or other noise sources are present, then the reconstruction SW will loose 1 wavelength. This effect was also noticed and tracked during repeated measurement of a fixed shape of the shell (e.g., during stability tests). We made no attempts to repeat those measurements, because a quite large dataset was built anyway, from which results can be extrapolated.

Figure 5.33, Figure 5.34, and Figure 5.35 show the Zernike modes from 3 to 12, for the maximum values of the delta-commands ($\pm 5 \mu m$ PtV as applied on the M4AU).

Figure 5.36 gives a summary plot of all the collected residual WFE values, up to the Zernike 20. As shown, all values are generally lower than 100 nm rms (on the WFE), and only few cases give higher values. As it can be noticed, residuals do not always increase when moving from the starting flat position (PtV = 0), partially due to noise in the measurement process and post-process of the interferometric images. This is also true for the piston and tip-tilt modes (see Figure 5.32). The reason why Zernike modes near the PtV=0 value are higher than 20 nm rms is that the starting point of the Zernike test was worse than the best one shown after flattening+cophasing was achieved. Anyway, because we are interested only on the variation from the starting position to the final one, only differential variations should be looked at. They will add quadratically to good flattening+cophasing command, so even better results can be expected.

5.8 Stability test

One of the goals of our tests was to provide data about the stability of the DP system, as function of varying environmental conditions.

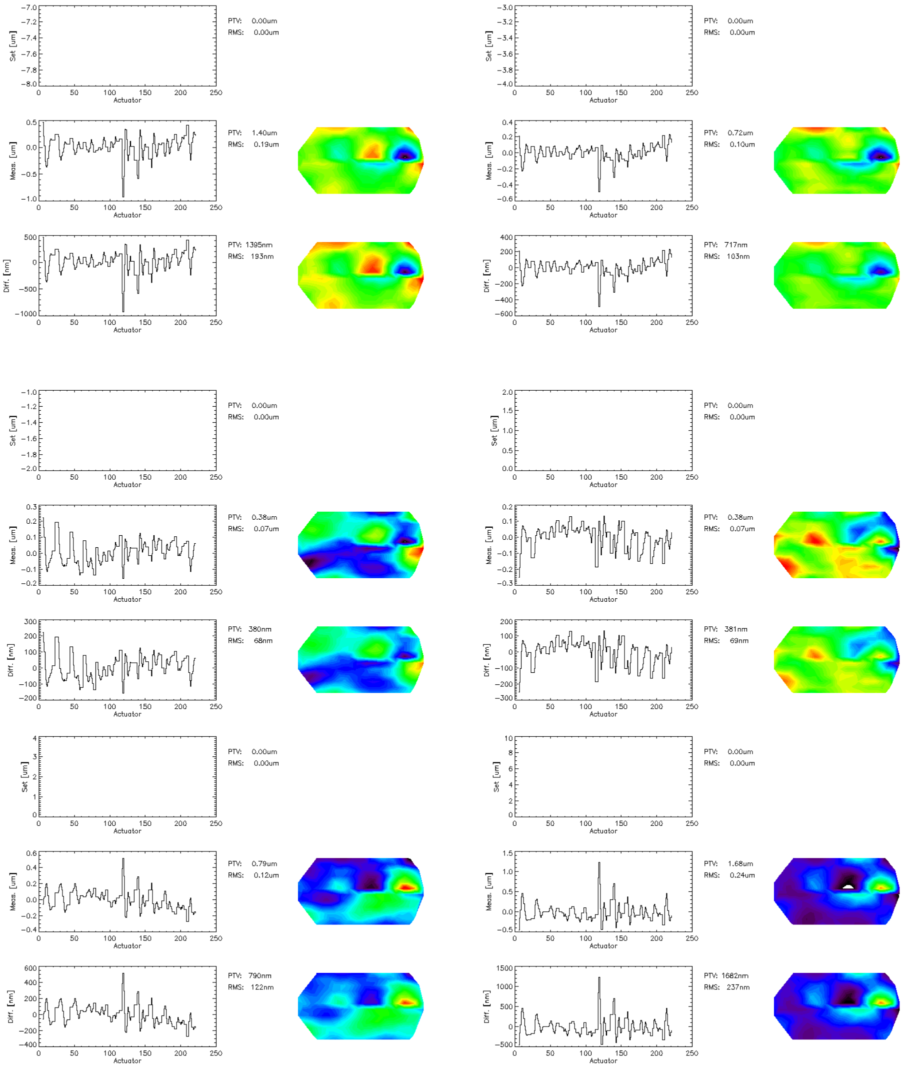

Figure 5.29: Piston mode at different delta command values.

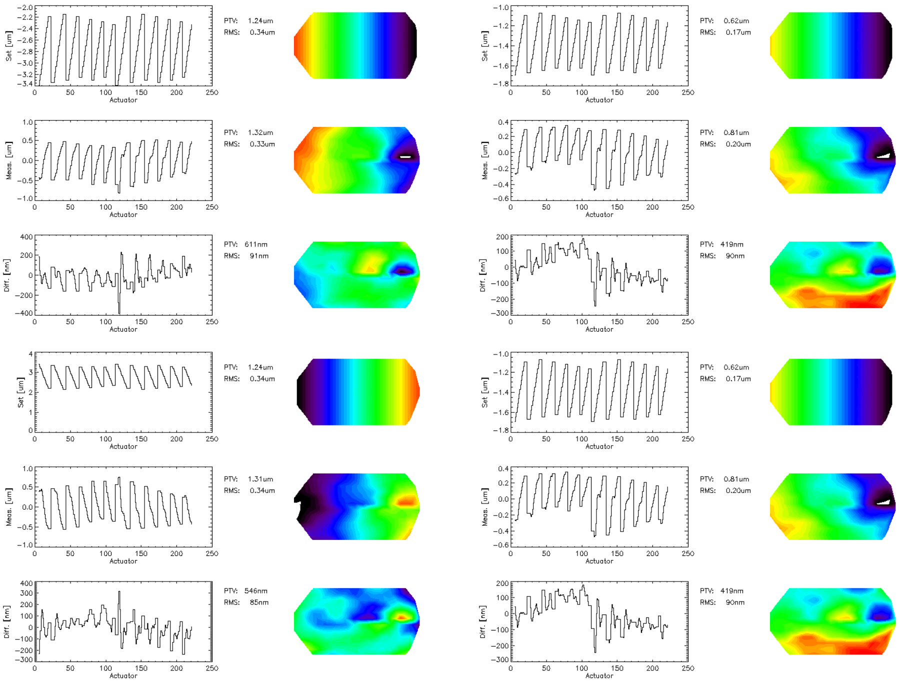

Figure 5.30: TiltY mode (Z1) as function of different PtV delta-commands, respectively, start to top-left: $-8\mu m$, $-4\mu m$ and $8\mu m$, $4\mu m$.

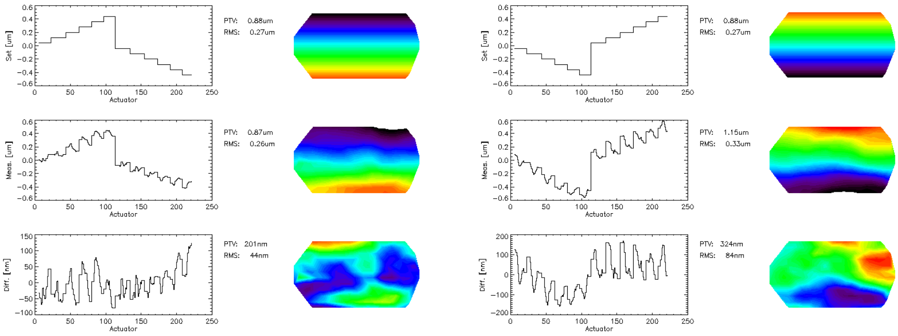

Figure 5.31: TiltX mode (Z2) as function of different PtV delta-commands, respectively $-8\mu m$ (left) and $8\mu m$ right.

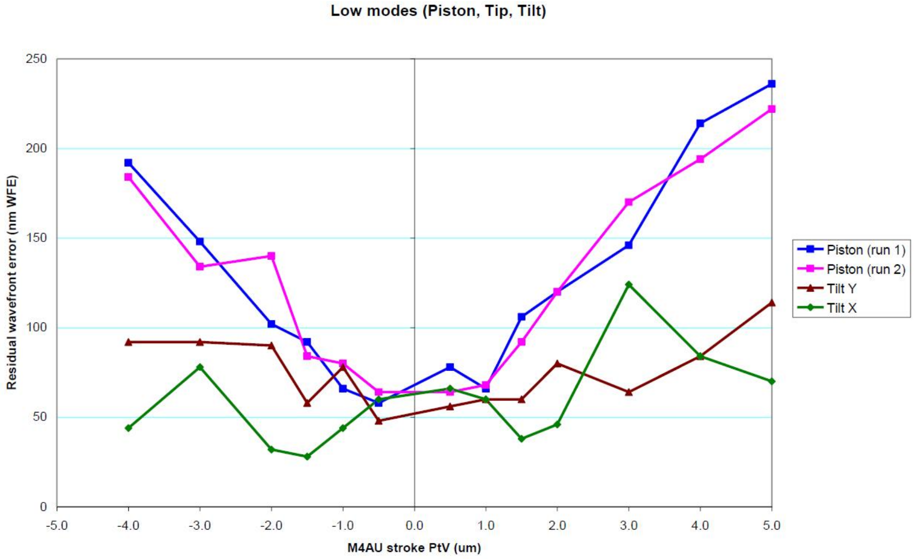

Figure 5.32: Residual wavefront error (WFE) after piston and tip/tilt commands as function of different PtV.

Report this test for completeness even though it was not performed by me because absent for maternity leave

A reference temperature profile inside the EELT dome was provided by ESO, reported in graphic in figure 5.37. Maximum variation is ± 1 degC around a mean value, with a maximum 0.4 degC/hr rate. It was decided to check stability of the flattening command + co-phasing as function of the thermal gradient between ambient and the DP body.

To make it possible in our lab, we changed the temperature of the cooling system, by steps of 1.5 - 2 degC, with rates higher than expected in the dome. Temperature of fluids, air and the reference body of the DP were acquired, to correlate WFE variations with them.

5.8.1 Stability of the flattening command

Figure 5.38 shows the WFE_{EELT} (nm rms) as function of the time in stationary conditions. The temperature value was that one measured at the outlet of the couling plant. A median filter (over 7 adjacent measures) was applied to smoothed out noise, mainly due to residual air-turbulence. WFE was measured removing piston and tip-tilt terms (on the DP coordinate system). Indeed, these terms are the only ones introduced by the cavity itself, when experiencing thermal variations.

Figure 5.39 shows the WFE variation when a temperature profile is applied to the cooling system. The PtV variation was 5 degC, larger than what typically expected during one observing night.

As shown, WFE correlate pretty well with thermal variations around the average temperature. Moreover, some noise is present when thermal gradients between ambient and the DP system are larger, due to increased air-turbulence near the DP surface area.

Spikes are due to wrong unwrapping of the reconstruction SW between the two islands (i.e., the two shells).

Results are within specifications, being smaller than 60 nm rms over the whole DP area.

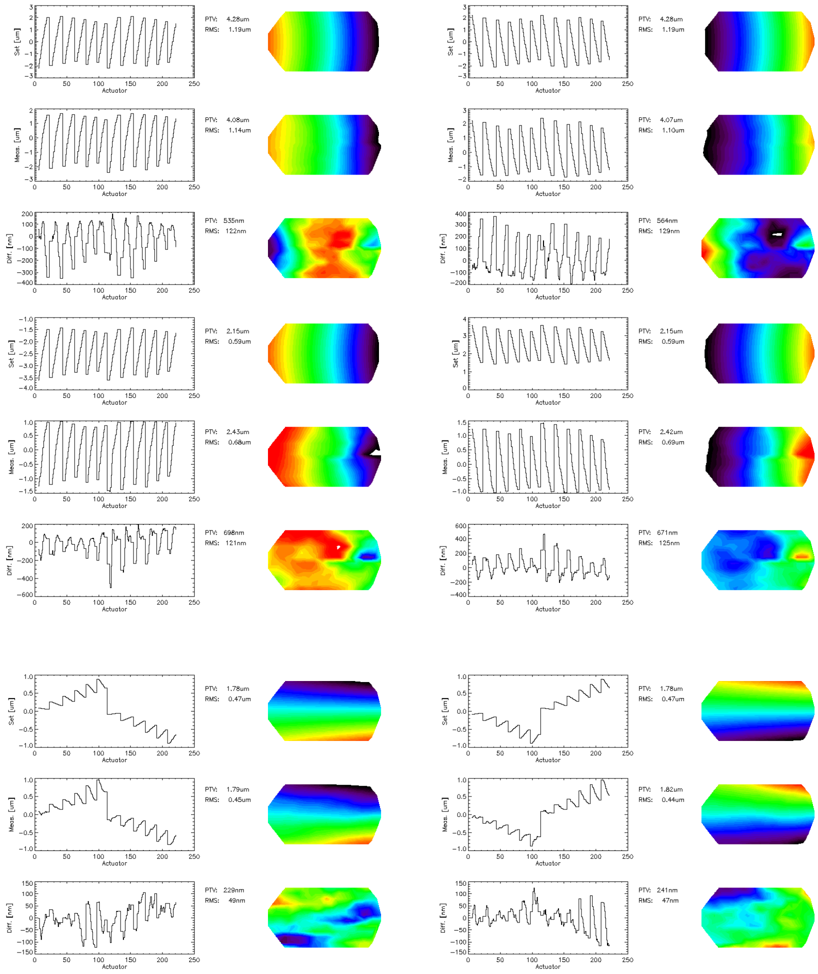

Figure 5.33: Zernike mode 3 (focus) - 4 (Y-astigmatism) - 5 (X-astigmatism) at maximum PtV values.

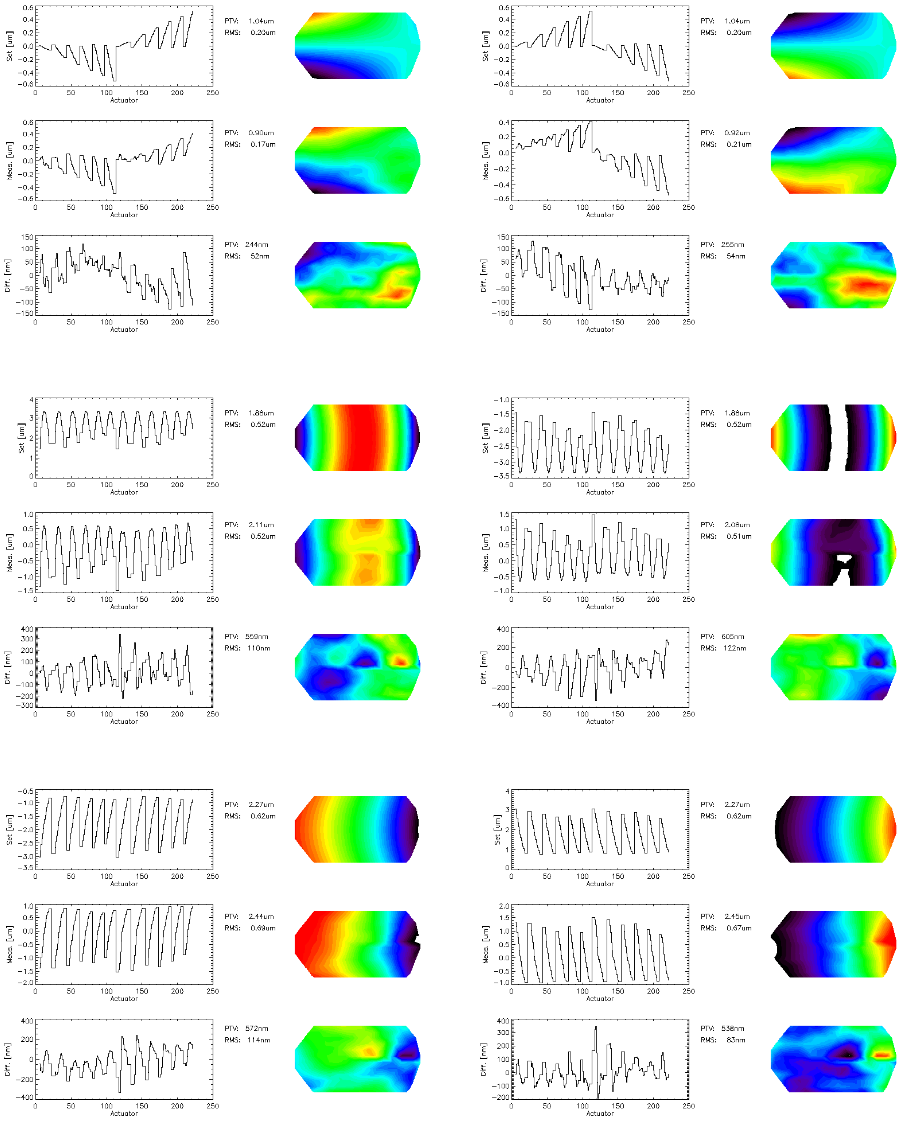

Figure 5.34: Zernike mode 7 (coma) - 8 (spherical) - 9 (trefoil) at maximum PtV values.

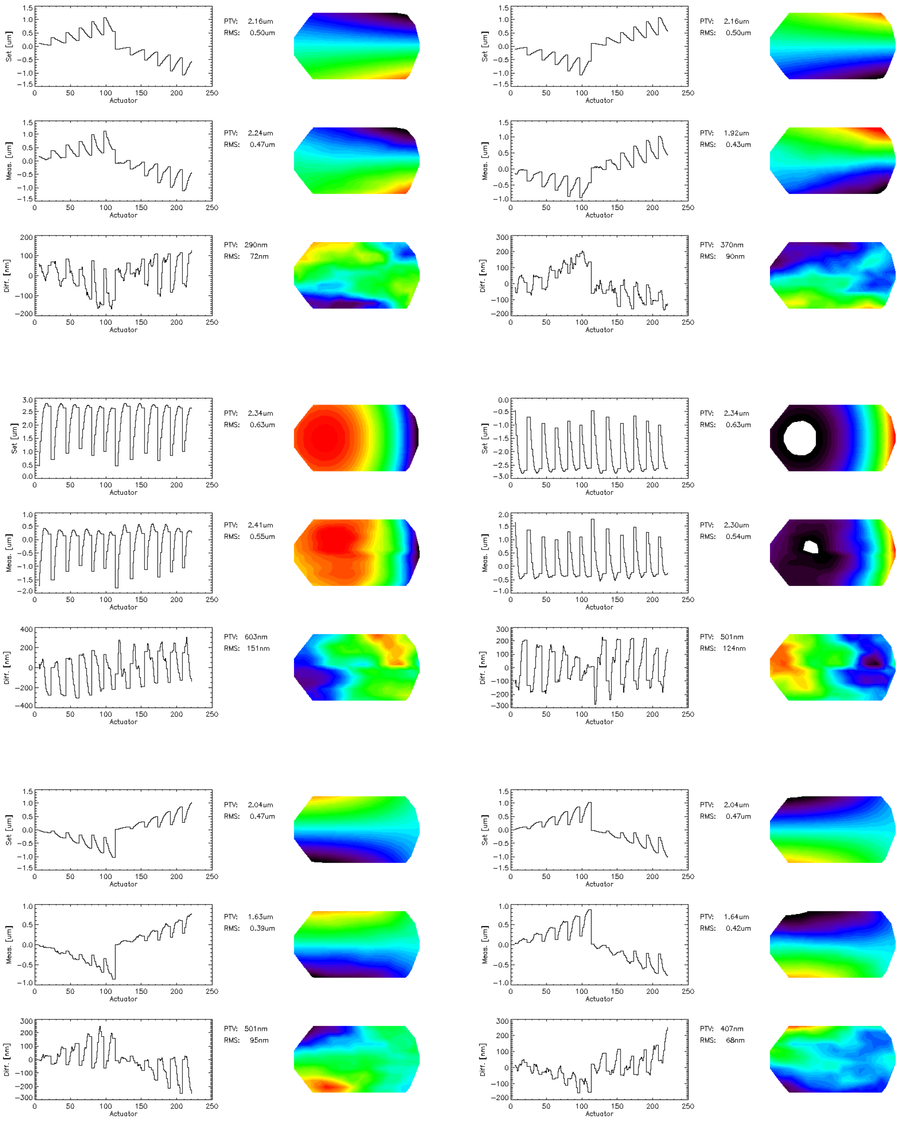

Figure 5.35: Zernike mode 10 - 11 - 12 at maximum PtV values.

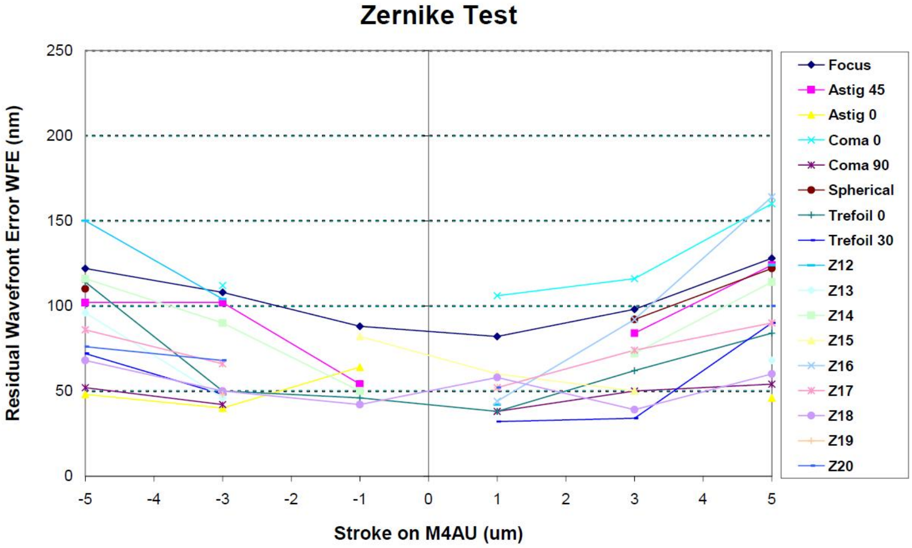

Figure 5.36: Zernike residual WFE for all Zernike modes from 3 to 20.

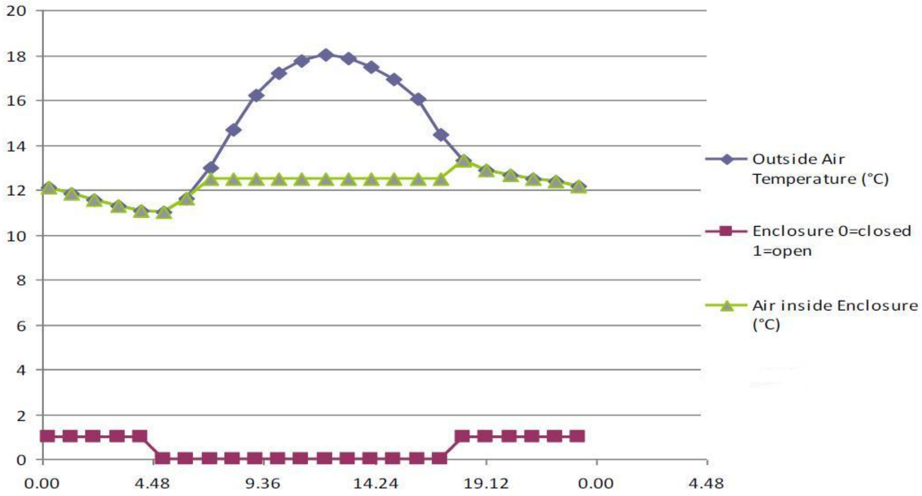

Figure 5.37: Temperature profile inside the dome.

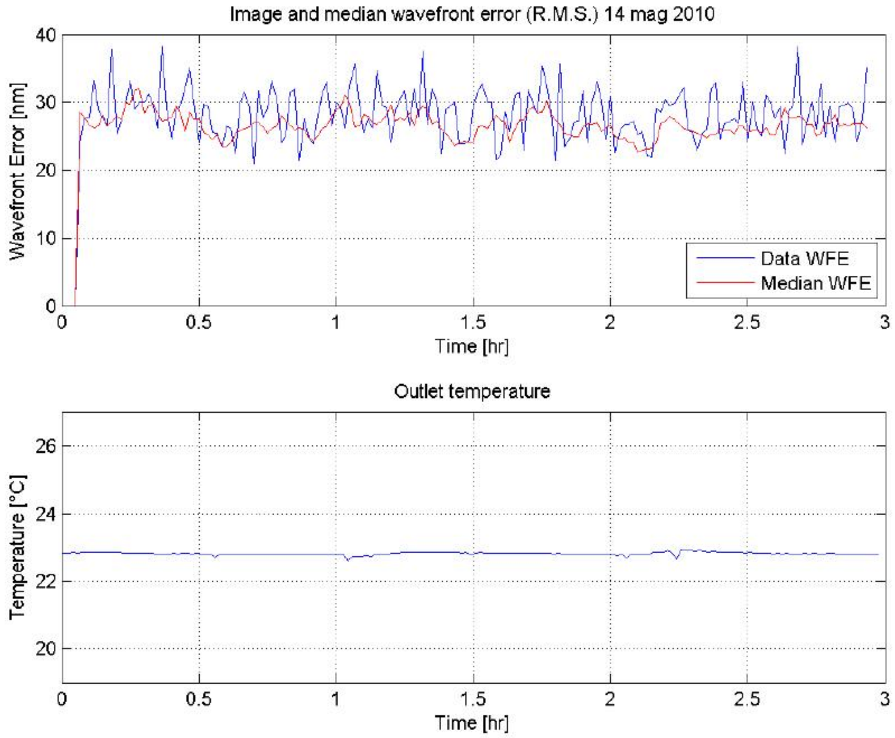

Figure 5.38: WFE(EELT) vs. time when no environmental changes happen.

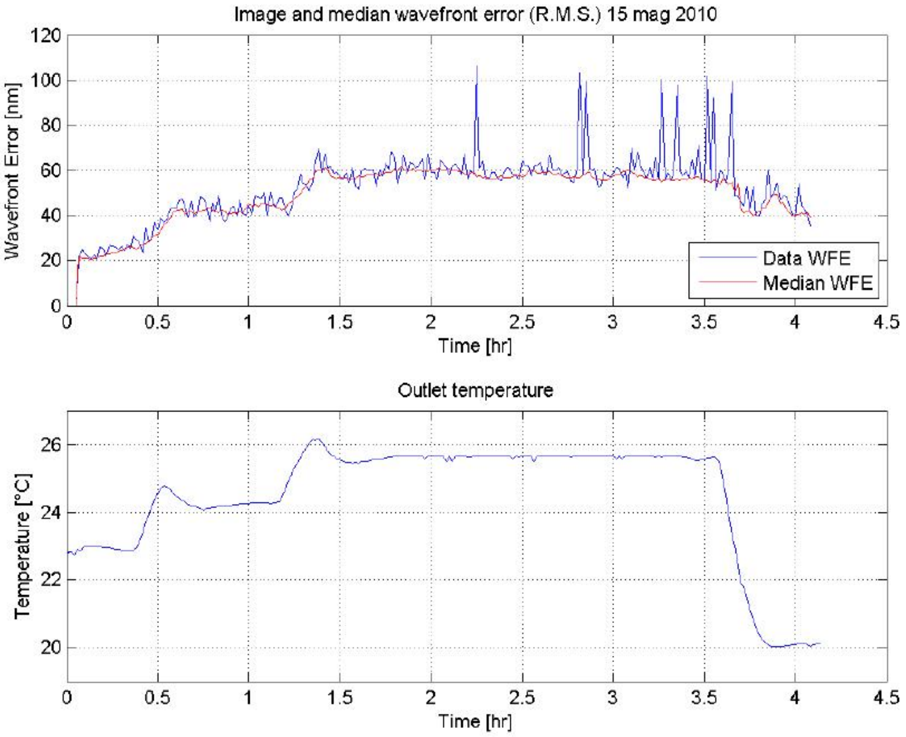

Figure 5.39: WFE(EELT) vs. time when outlet temperature varies as shown in the plot below.

5.8.2 Stability of the co-phasing

Together with flattening stability, we checked also the stability of the co-phasing, especially near the gap between the two shells. We measured the differential piston between the two edges of the shells as function of position along the gap and time. Proper conversion factors were applied to get the WFE (EELT) values. The results are reported hereafter. Figure 5.40 and Figure 5.41 present the differential piston measured along the segments separation. The position along the separation is reported in the left Y legend, pixel 0 corresponds to the shell free edge and pixel 250 corresponds to the last unmasked point, close to the membrane (see Figure 5.22 for the masked area). The color bar legend reports the differential piston error, in nm rms WFE. The X-axis represents the time from the beginning of the test. The lower plot reports the cooling water outlet temperature. In Figure 5.41 there is an evident drift of the differential piston located in a restricted area of the shell, corresponding to the DP area near to the membrane. These measurements confirm that shells maintain their average co-phasing, except on isolated zones affected by the membranes that, as reported, are strongly different and stiffer than the final ones.

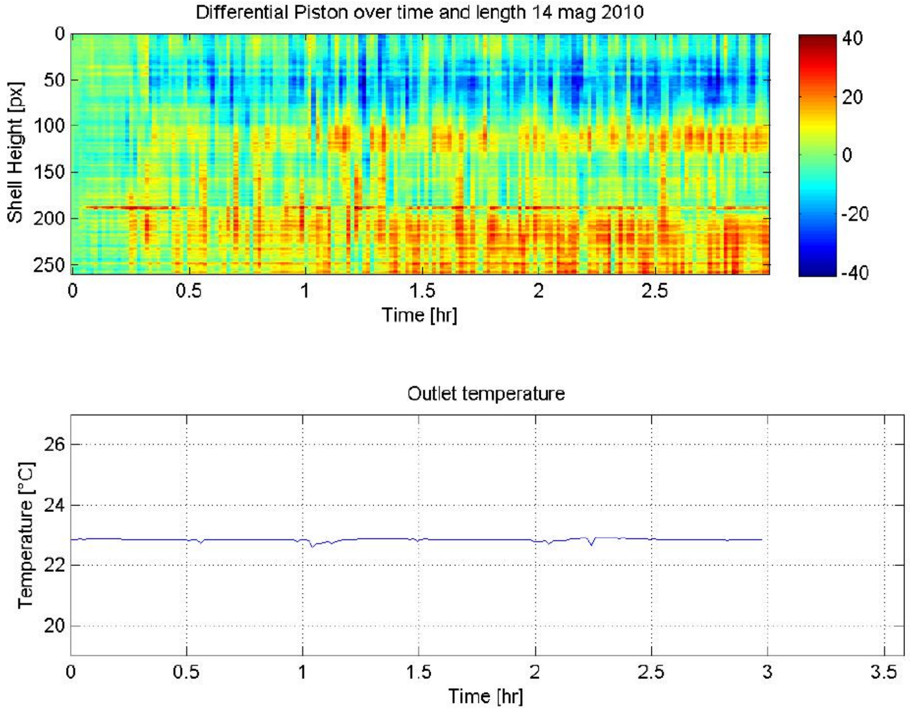

Figure 5.40: Piston (nm in DP coordinates) vs. time and gap position in stationary conditions.

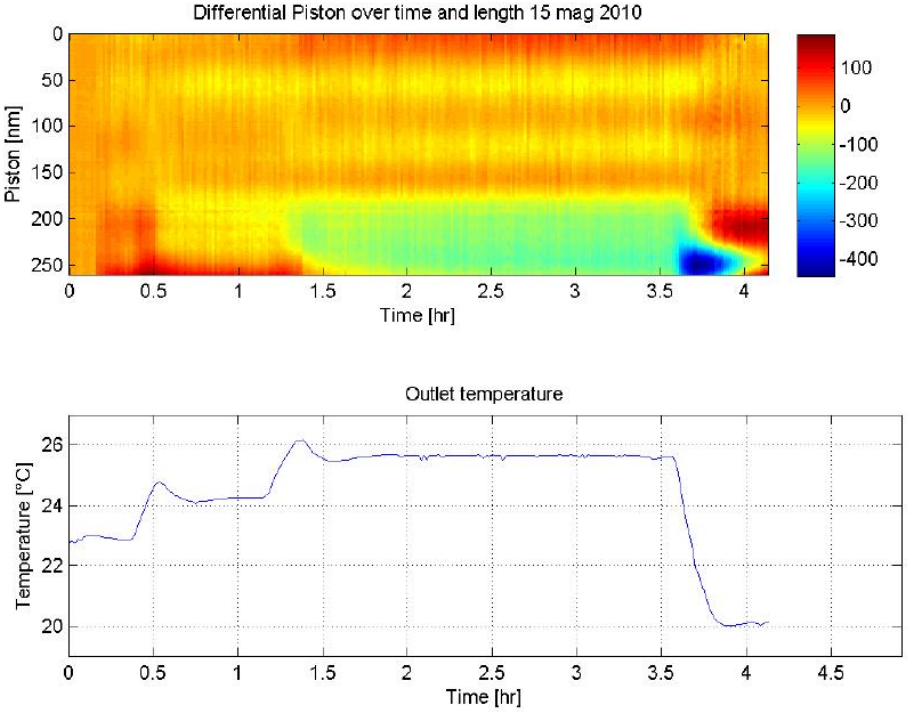

Figure 5.41: Differential piston (nm in DP coordinates) vs. time and gap position under thermal loads.

Chapter 6

Conclusion

The preview chapter reports about the M4DP optical tests that have been carried out. The performed tests cover all different aspects, including *system calibration, flattening, correction capability, co-phasing and stability*.

These results are supported with a quite large dataset, covering all important issues about this prototype.

Two different test setups, namely the SIS and the RCT, have been successfully verified and used for the test execution. Moreover a dedicated Piston Sensing Unit has proved his functionality and performance on the Demonstration Prototype. The SIS setup is useful when the initial shape of the mirror is very out of the range of the interferometer. Another possibility to take into account to test the final unit is to improve the resolution of the interferometer.

The tests development, and in particular the initial calibration activity, has allowed practicing with the real system and digging into the planned test procedures, adapting them to the real needs when necessary. These optical test facilities and procedures gave enough degrees of freedom to overcome unknown effects in a fast and effective way. The tests ***have widely demonstrated the validity of the proposed concept*** that has fulfilled the given specifications in most cases, with just few limitations.

Flattening and co-phasing of the DP shells were achieved, within given specifications, demonstrating that the whole manufacturing process loop is properly working, including the mechanical assembly, the integration process of many different sub-components, electronic drivers and controllers, both on-board and on the DP control system. In particular, the correction capability over a large stroke range has been proved. Also the stability of the system has been confirmed, not only by the acquired data, but also by a general feeling of stability and repeatability operating the system over a significant time and under different setup conditions.

The membranes constraining the shells in-plane, being significantly different and stiffer than the ones designed for the final M4 unit, forced us to exclude from the measurements a not negligible portion of the shells, and caused also some limitation in the final performances. Concerning the co-phasing issue, we demonstrated that the two shells remain well in phase over a large temperature range. The results show a very good behavior over most of the shell gap, with a limited area were a higher, but still acceptable drift has been observed. Referring to the optical fabrication quality, the tests have confirmed a very low residual at sub-Nyquist spatial scales and, last but not least, an excellent quality of the shells cuts.

In the next table (6.1) we can see that all the optical tests performed have been successfully passed.

Table 6.1: Verification Matrix

TITLE	SUCCESS CRITERIA	RESULTS	NOTE
Pre-flattening of the shell	Reduce the shape error below a 2 micron shape error (PtV) over most of the shell area	Shape error on shell DX: $< 1.1 \mu m$, SX: $< 1.6 \mu m$ PASSED	
Static optical influence function measurements (zonal and modal)	Mismatch between measured and FEA stroke-per-unit-force < 15 %	Measured mismatch: -6%	PASSED
Optical flattening	DP WFE (rms) < 20 nm for larger scales than twice inter-actuator spacing. WFE(EELT) < 15 nm (rms) for smaller scales. The stroke requested to maintain the shape shall not be larger than 10% of the total actuator stroke in force (< 0.14N)	WFE(EELT) SX: 14 nm rms DX: 12 nm rms Forces (0.5 PtV) SX: 0.13N DX: 0.12N WFE(EELT) SX: 9 ± 4 nm DX: 9 ± 7 nm	PASSED
Absolute calibration of actuator stroke	After a full range piston command WFE(EELT) < 250 nm (rms)	WFE(EELT) <240 nm rms	PASSED
Removal of differential tilt	WFE(EELT) < 20 nm (rms)	WFE(EELT) = 19 nm rms	PASSED
Co-phasing of the two shells	WFE(EELT) < 20 nm (over both shells)	WFE(EELT) = 19 nm rms	PASSED

Appendix A

Test Plans and Test Procedures

TITLE **Absolute Calibration of the return sphere**

SCOPE The test is finalized to check the surface quality of the spherical mirror. If large, this error must be subtracted from the WFE measurement in RCT mode.

TEST EQUIPMENT Optical bench, Fizeau interferometer with a transmission sphere, Folding mirror, Some white paper sheets to check alignment, Reduction SW.

TEST SEQUENCE

1. Place the spherical mirror on its support in the same working condition of the Sferovsy optical test
2. Load the transmission sphere into the interferometer
3. Rough alignment of the optical beam, using paper masks, with the help of the adjustments
4. Switch from align to view mode on the interferometer and fine adjustment of fringes
5. Take a first WFE map
6. Rotate the spherical mirror around its normal by 180 degrees, check alignment, and take a second WFE map
7. Place a flat reference mirror in the focus of the transmission sphere and take a third WFE map
8. Compute the shape of the spherical mirror surface
9. Repeat the whole measurement process (steps 1-8) to check reproducibility

SUCCESS CRITERIA Verify compliance with the cavity error budget, where we assigned a WFE<60nm (rms) over the whole area of the mirror.

TEST RESULTS The manufacturer provided a quality certificate for the mirror in vertical position, of about 5 nm (rms), and 34 nm (PtV) over 99% of the area. In our operating condition, with a different gravity load, we measured $WFE < 15nm(rms)$, much lower than the given budget. By the way, this measurement include errors on the flat folding mirror, at the level up to 10 nm rms. As a result, we decided to avoid WFE subtraction from RCT measurements.

TITLE **Alignment of the RCT optical bench**

SCOPE Adjustment of each component of the optical test setup in the correct position in order to minimize the fringes into the interferometer.

TEST EQUIPMENT RCT test setup will be mounted onto the optical bench, Fizeau interferometer with a transmission sphere, Flat Folding mirrors for alignment purposes, Spherical Mirror with diameter of 50 cm, Mechanical Support, White paper sheets to check alignment.

TEST SEQUENCE

1. Mount all the optical elements within the mechanical tolerances on the optical bench
2. Mount a flat mirror in the same position of the DP shell mirror
3. Align the optical path of the system with the fine adjustments of the folding mirror and the spherical ones in order to minimize fringes in the interferogram
4. Remove the flat alignment mirror, and mount the DP system on the RCT setup. Repeat step 3.
5. Correct for imaging focus and maximize the spatial sampling with a zoom capability of the interferometer
6. After flattening command, refine alignment, focus and zoom.

SUCCESS CRITERIA Maximum area of the DP surface illuminated by the optical beam, well centered on the sample beam. Well focused edges of the mirror area.

TEST RESULTS This alignment was carried out onto a 200 mm flat mirror as a preliminary step. Exchanging it with the DP drastically reduced the amount of time to align the RCT cavity over the final DP surface.

TITLE **Alignment and calibration of the SIS setup**

SCOPE Alignment of optical components and motorized stages in order to minimize systematic errors during the acquisition process. Calibration of the cavity error and of the spatial scale.

TEST EQUIPMENT Fizeau interferometer with a high-quality flat transmission reference plate, Two flat folding mirrors, High- precision motorized rails, Tip-tilt platform to align the cavity, on top of the motorized rails, Good reference flat mirror (10 cm diam.), Fine tip/tilt stage for alignment during calibration, White paper sheets to check alignment.

TEST SEQUENCE

1. Mount a flat transmission reference on the interferometer
2. Align the two folding mirrors within mechanical tolerances
3. Check the co alignment of the folding mirrors w.r.t the chief ray of the optical beam, moving the rails along their full range
4. Acting on the tip/tilt stages, close the cavity and minimize fringes
5. Check repeatability of fringe number at the same location (at a fixed XY coordinate)
6. Place a flat mirror, with fiducials, before and after the two folding mirrors, and measure the two WFEs
7. Check repeatability of WFE measurement (including averages to reduce noise) below the 3 nm (rms) level
8. Subtract the two WFEs and save this calibration map for the following SIS measurements
9. Put a known size mask along the cavity and check its size in pixel. The ratio between the two measurements gives the spatial scale.

SUCCESS CRITERIA WFE repeatability must be smaller than 3 nm (rms). Spatial scale about 0.25 pixel/mm.

TEST RESULTS All these steps were preliminary performed with a flat mirror at the same DP position. Fiducials were applied to accurately calibrate the spatial scale. Rails movements were aligned w.r.t. optical beam giving a overall shift of <5 pixels over the whole travel of both axes.

TITLE **Pre-flattening of the shell**

SCOPE This test measure and correct shape error of the shells exceeding the capture range of the RCT setup and allow measuring of influence functions.

TEST EQUIPMENT SIS setup, Acquisition and reduction SW

TEST SEQUENCE

1. Make SIS setup well aligned
2. Set shell to the nominal gap with respect to reference plate using the standard setting procedure
3. Measure the feed-forward matrix (pure electronic measurement: force vs. capacitive sensor output) and compute the corresponding SVD modes (FF modes)
4. The electronic (capacitive sensor reading) measurement of the gap is decomposed in FF modes and low-order FF modes are removed (excluding piston)
5. Align SIS cavity and start acquisition of single OPD maps on sub-apertures of 100 mm
6. Collect data and stitch single maps to create the whole map of the shell area
7. Compute actuator position (applying small strokes on single actuators) to calibrate them on the stitched map
8. Compute the correction to be applied
9. Filter the correction over few modes (<30) and apply correction
10. Iterate from step 5 to 9 until 2 μm (PtV) level is reached
11. If not, increase the number of modes to be applied, and repeat steps 6-10
12. Record the pre-flattening command

SUCCESS CRITERIA Reduce the shape error below a 2 micron shape error (PtV) over most of the shell area.

TEST RESULTS This procedure was performed successfully with only few iterations on both shells. Applying less than 60 modes, and masking the area near the membrane, a 80 nm (rms) level was reached. PtV variation was $< 1\mu m$ on shell DX, and $< 1.6\mu m$ on shell SX.

TITLE **Static optical influence function measurements (zonal and modal)**

SCOPE This test verifies the match between the stroke applied by the actuator per unit force and the corresponding values given by the FEA simulation. Moreover, it gives the basis to flatten the shells.

TEST EQUIPMENT RCT setup, Acquisition and reduction SW

TEST SEQUENCE

1. Put shell at the EM preliminary flattening position (from FFWD)
2. Apply the pre-flattening command

3. Refine RCT alignment
4. Meas A: move one actuator to $-\Delta$ ($\Delta = 100, 200$ nm) and take a WFE map
5. Meas B: move one actuator to $+\Delta$ and take a WFE map
6. Compute the *zonal influence function* map as (B-A)/2
7. Per each step, store capsens position and force of each actuator
8. Repeat steps 3-6 for all the visible actuators
9. Store *Zonal Influence Functions*
10. Meas C: send delta-command $-\Delta$ (not exceeding forces) to all actuators
11. Meas D: send delta-command $+\Delta$
12. Compute the modal influence function maps as (D-C)/2
13. Per each step, store capsens position of each actuator
14. Repeat steps 9-12 for all the visible actuators
15. Store Modal Influence Functions
16. Compute the stroke-per-unit-force on actuators.

SUCCESS CRITERIA Mismatch between measured and FEA stroke-per-unit-force $< 15\%$

TEST RESULTS Both zonal and modal influence functions were measured many times, in different working conditions, variable incidence angles, and flattening steps. As realized during these tests, a preliminary flattening, through SIS, is very helpful to reduce the first large error shape, and make RCT measures possible over the whole DP area. Zonal influence functions were compared with FEA. On average, measured stiffness at the peak of zonal influence functions, measured inside the shell area (i.e., not along the edges), was 6% lower than expected, well within expectations. A relatively large scatter was observed, but it can be traced back to measurement uncertainties, and miscalibration of the force reading.

TITLE **Optical flattening**

SCOPE Calibration of the flattening actuators commands

TEST EQUIPMENT RCT setup, SIS setup, Acquisition and reduction SW

TEST SEQUENCE

1. DP mounted on the RCT test setup
2. Influence functions were measured, and interaction matrix computed
3. Put shell at the EM preliminary flattening position (from FFWD)
4. The optical alignment of the test facility is refined
5. Meas A: apply k-th mode with amplitude $+\Delta k/2$ and take OPD map
6. Meas B: apply k-th mode with amplitude $-\Delta k/2$ and take OPD map
7. Compute the optical modal influence function of k-th mode as (B-A)/2
8. Repeat steps 5-7 for all decomposed modes (equal to the enabled actuators)
9. Collect data of the optical influence functions in the columns of the modal influence matrix
10. Compute the pseudo invert of matrix M using SVD and filtering out singular modes having singular values below a given threshold ($0.1 \div 0.01$ to be optimized), obtaining the reconstruction matrix R

11. Take OPD map of the DP and compute the coefficients of first N FF modes via the reconstruction matrix R
12. Compute the actuator commands from the modal coefficients obtained in the previous step, reverse the sign and apply the result as command to the DP actuators
13. Increase the number of modes N and iterate steps 11-12 until no further improvement in rms flattening residual or force threshold is reached
14. If too high forces are generated, relax forces and start again iterative loops 11-12
15. Record the flattening command
16. Switch to the SIS setup
17. Take OPD maps over the whole DP area moving folding mirrors
18. Compute the stitched image
19. If WFE > 100 nm rms, then compute the correction command and apply on the DP
20. Iterate steps 16-19, until threshold is reached
21. Switch to RCT setup again, and repeat steps 7-15 to refine the flattening
22. Repeat steps 2-22 until convergence below given threshold is reached

SUCCESS CRITERIA WFE (rms) < 15 nm for scales smaller than twice inter-actuator spacing WFE (rms) < 20 nm for larger scales.

The stroke requested to maintain the shape shall not be larger than 10% of the total actuator stroke (in force or in position)

TEST RESULTS Test was performed many times to fine tune the procedure, debug all the related routines, define convergence parameters in the best way. After this preliminary steps, once modal influence functions are acquired, flattening of the shell can be reached within few days or even less, strongly depending on the accuracy and noise level of the influence functions. Both requirements in WFE was reached on both shells over a quite large area, excluding the portion near the membrane, due to its highly distorted initial state and higher stiffness, due to the clamping system. Actuator stroke, both in force and position. The reached values are: - shell DX: WFE = 12 nm (rms), 110 (ptv) forces: 0.04 N (rms), 0.23 N (ptv) - shell SX: WFE = 14 nm (rms), 133 (ptv) forces: 0.04 N (rms), 0.25 N (ptv)

TITLE **Optical calibration of actuator stroke**

SCOPE This calibration was done to reduce the induced WFE on surface shape due to miscalibration of capacitive sensors. This is a preliminary step toward co-phasing of the two shells

TEST EQUIPMENT SIS setup, Acquisition and reduction SW

TEST SEQUENCE

1. Apply the flatness command on the DP (see the Optical Flattening procedure)
2. Switch to SIS
3. Center the SIS on one actuator position
4. Apply $\lambda/2$ piston stroke on DP shells, and record fringes
5. Compute the phase shift after this step, and apply correction on the next $\lambda/2$ piston stroke

6. Apply $\lambda/2$ piston stroke including correction from previous step
7. Iterate steps 4-6 until a full range of actuator stroke is reached
8. Move the next actuator position and repeat steps from 3 to 7
9. Iterate over all actuators
10. Compute calibration curves to be applied on each actuator and update capsens LUT
11. Switch to RCT setup
12. Apply re calibrated piston command and check if surface is flat below a given threshold

SUCCESS CRITERIA WFE after a full range piston command < 250 nm (rms)

TEST RESULTS This test was implemented and performed successfully. After +/- 5 um piston command, the WFE < 240 nm rms

TITLE **Removal of differential tilt**

SCOPE This calibration was done to reduce the induced WFE on surface shape due to miscalibration of capacitive sensors. This is a preliminary step toward co-phasing of the two shells

TEST EQUIPMENT SIS setup, Acquisition and reduction SW

TEST SEQUENCE

1. Apply the flatness command on the DP (see the Optical Flattening procedure)
2. Switch to SIS
3. Take OPD map over the gap between the two shells
4. Over single OPD maps, compute the local differential tilt between the two shells
5. Average between all acquired OPD maps, and apply half tilt correction to each shell
6. Iterate steps 3-5 until no further improvement is possible
7. Switch to RCT setup
8. Take a full OPD map over both shell area
9. Compute the differential tilt between the two shells
10. Apply half correction to each shell
11. Iterate steps 9-10 until no further improvement is reached

SUCCESS CRITERIA WFE (rms) < 20 nm

TEST RESULTS This test was successfully performed reaching a 10 nm (rms) level.

TITLE **Co-phasing of the two shells**

SCOPE This measurement will be done to test the ability of the system to reach the phasing of the two shells and validate the PSU functionality.

TEST EQUIPMENT PSU, Acquisition and reduction SW

TEST SEQUENCE

1. Apply the flatness command on the DP
2. Switch to RCT setup
3. Take a OPD map of flattening residual

4. Control the gap between the two shells over the area where PSU will be located
5. Mount PSU under DP shell within mechanical tolerance
6. Align PSU with adjustment, until a spot is centered on its detector area
7. Inject broadband light via optical fiber on the PSU
8. While scanning DP shells, take images with PSU
9. Compute differential piston and apply correction command to both shells (half-half)
10. Change to a narrow-band filter
11. Repeat steps 8-9 to refine differential piston measurement
12. Apply final correction
13. Switch to RCT setup
14. Take OPD map over the whole DP area and measure the global differential piston
15. Compute correction on each shell and apply it
16. Iterate 14-15 until a given threshold is reached
17. Record this as "flattening + co-phasing" command

SUCCESS CRITERIA WFE (rms) < 20 nm (over both shells)

TEST RESULTS This test was successfully performed. Properly selecting the area for the PSU, really few iterations with RCT is required to go below the 20 nm (rms) level.

TITLE **Static flat tilt test**

SCOPE This measurement will be done to test the ability of the system to maintain the flat shape when the actuators work in a condition of maximum tilt stroke.

TEST EQUIPMENT RCT setup, Acquisition and reduction SW.

TEST SEQUENCE

1. Switch to RCT
2. Send a tilt command of amplitude 3 μm PV
3. Take OPD map
4. Compute reconstructed surface shape error by SW and residuals
5. Repeat steps 2-4 for all these amplitudes: -10, -6, -3, 3, 6, 10 μm
6. Repeat steps 2-5 for the tip mode

SUCCESS CRITERIA WFE (rms) < 250 nm (REQ NAO)

TEST RESULTS Test was successfully performed for both tip and tilt modes. Worst result is at $-9\mu m$ PtV with 146nm rms.

TITLE **Low order Zernike optics tests**

SCOPE This test is performed to study the ability of the M4AM to correct the lowest 20 Zernike modes.

TEST EQUIPMENT RCT setup, Acquisition and reduction SW.

TEST SEQUENCE

1. Switch to RCT
2. Send a Zernike mode command of amplitude $3\mu m$ PV

3. Take OPD map
4. Compute reconstructed surface shape error by SW and residuals
5. Repeat steps 2-4 for all these amplitudes: -10, -6, -3, 3, 6, 10 μm
6. Repeat steps 2-5 for the lowest 20 Zernike modes

SUCCESS CRITERIA Residual errors will be: WFE (rms)< 250 nm (REQ NAO)

TEST RESULTS Test was successfully performed for all Zernike modes; we report here the result of Z4, 10μm PtV amplitude: 136 nm rms

TITLE **Stability of mirror shape test**

SCOPE With this test we intend to verify the capacity of the system to maintain a flat shape in a given time interval.

TEST EQUIPMENT RCT setup, Acquisition and reduction SW.

TEST SEQUENCE

1. Apply the flatness command to the DP
2. Switch to RCT setup
3. Take OPD map of flattening residual (piston and tip-tilt removed)
4. Repeat step 3 every 30-60 seconds for at least 2 hr to check initial stability
5. Change cooling liquid temperature by -1.5 deg C, while continuing acquisition process
6. Wait until a steady state is reached
7. Apply another temperature step, still continuing acquisition process
8. Apply another temperature step, until a full temperature history will be applies
9. Extract WFE (rms) and correlate with temperatures

SUCCESS CRITERIA WFE (rms) < 250 nm

TEST RESULTS Test was successfully performed. WFE (rms) < 140 nm for delta T in excess of +/- 4 deg C

Appendix B

Zernike functions

Z0	1	PISTON
Z1	$2\rho\cos\vartheta$	TILT Y
Z2	$2\rho\sin\vartheta$	TILT X
Z3	$\sqrt{3}(2\rho^2-1)$	FOCUS
Z4	$\sqrt{6}\rho^2\cos 2\vartheta$	ASTIGMATISM 0°
Z5	$\sqrt{6}\rho^2\sin 2\vartheta$	ASTIGMATISM 45°
Z6	$\sqrt{8}(3\rho^3-2\rho)\cos\vartheta$	COMA 0°
Z7	$\sqrt{8}(3\rho^3-2\rho)\sin\vartheta$	COMA 90°
Z8	$\sqrt{5}(6\rho^4-6\rho^3+1)$	SPHERICAL
Z9	$\sqrt{8}\rho^3\cos 3\vartheta$	TREFOIL 0°
Z10	$\sqrt{8}\rho^3\sin 3\vartheta$	TREFOIL 30°
Z11	$\sqrt{10}(4\rho^4-3\rho^2)\cos 2\vartheta$	
Z12	$\sqrt{10}(4\rho^4-3\rho^2)\sin 2\vartheta$	
Z13	$\sqrt{12}(10\rho^5-12\rho^3+3\rho)\cos 2\vartheta$	
Z14	$\sqrt{12}(10\rho^5-12\rho^3+3\rho)\sin 2\vartheta$	
Z15	$\sqrt{7}(20\rho^6-30\rho^4+12\rho^2-1)$	
Z16	$\sqrt{10}\rho^4\cos 4\vartheta$	
Z17	$\sqrt{10}\rho^4\sin 4\vartheta$	
Z18	$\sqrt{12}(5\rho^5-4\rho^3)\cos 3\vartheta$	
Z19	$\sqrt{12}(5\rho^5-4\rho^3)\sin 3\vartheta$	
Z20	$\sqrt{14}(15\rho^6-20\rho^4+6\rho^2)\cos 2\vartheta$	

Z1

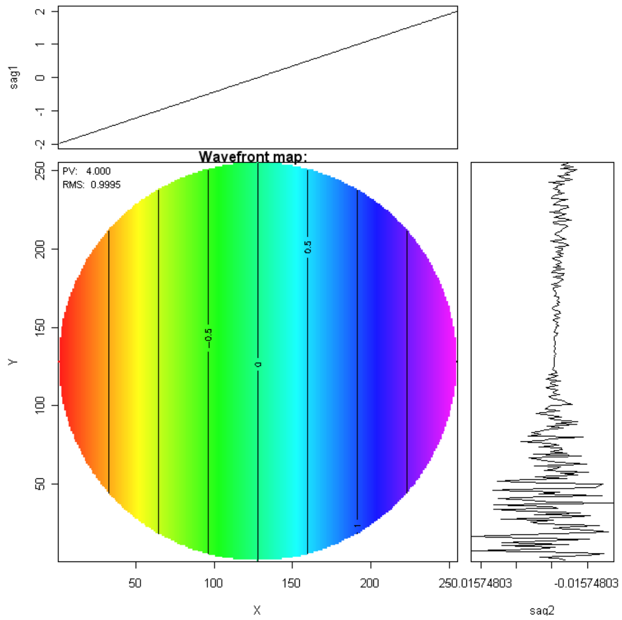

Z2

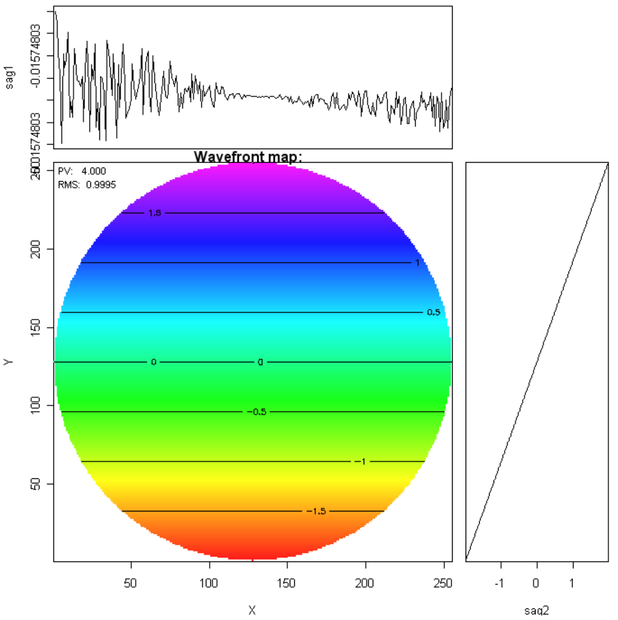

Z3

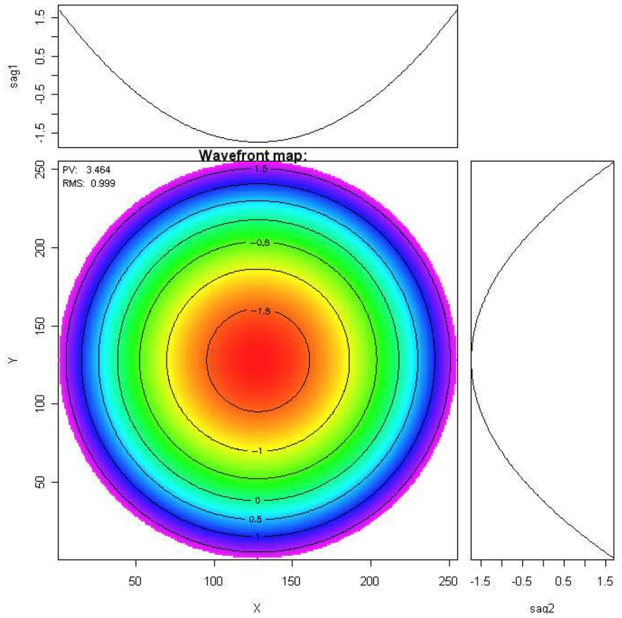

Z4

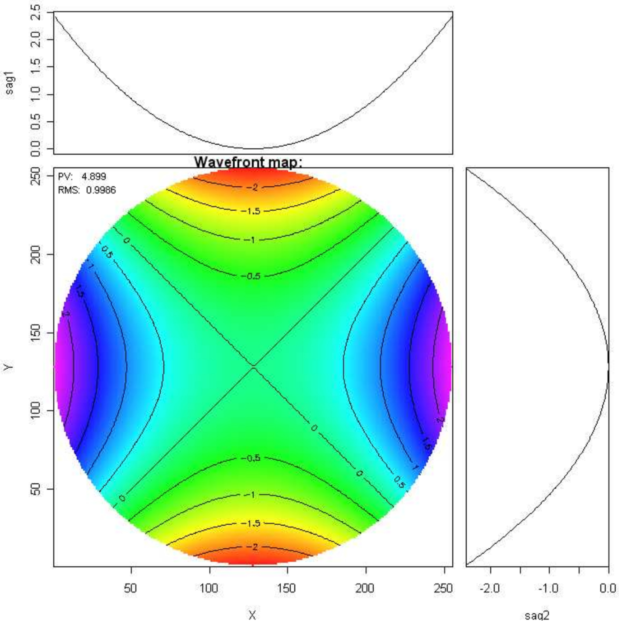

Z5

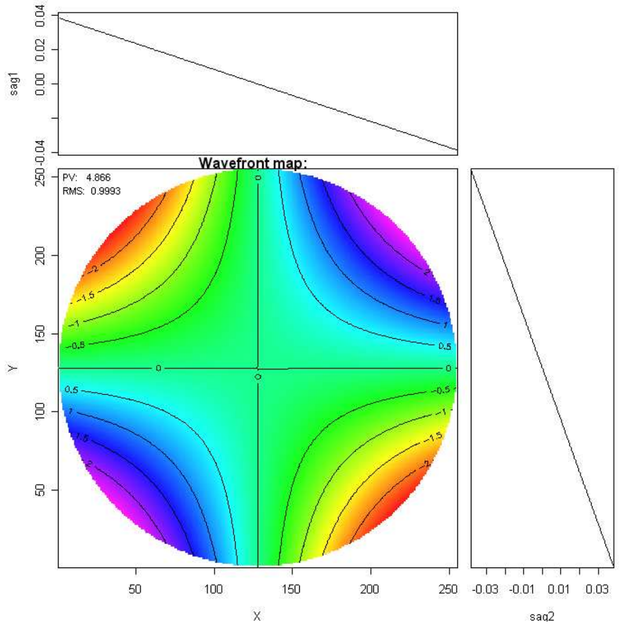

Z6

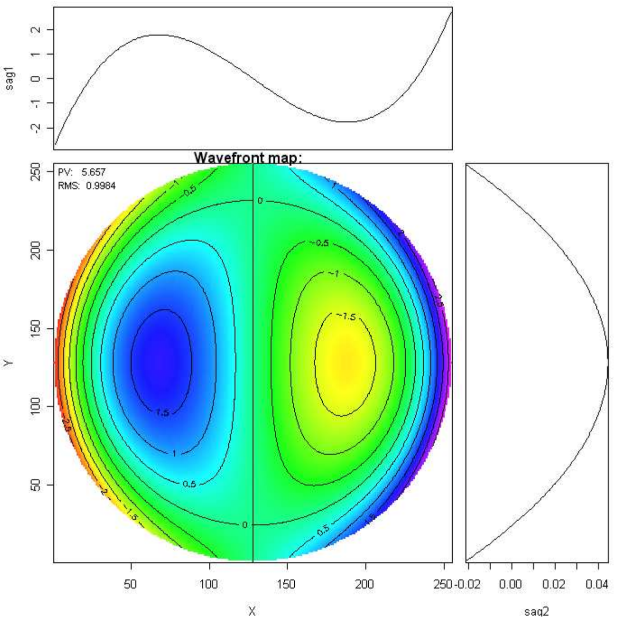

Z7

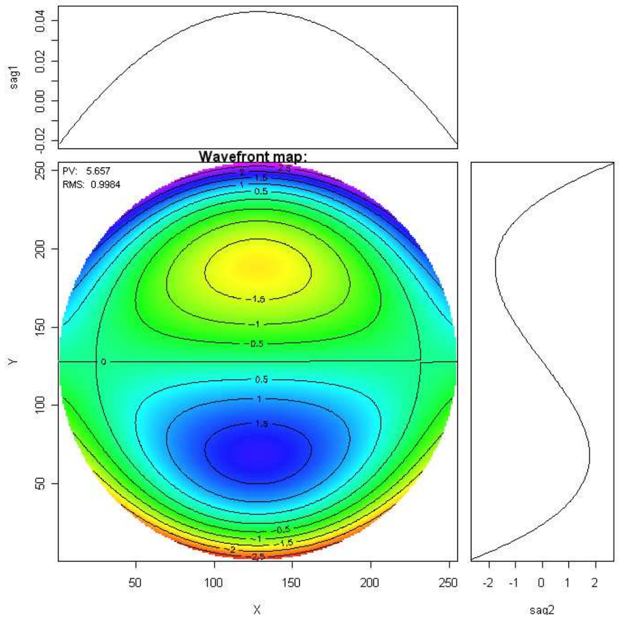

Z8

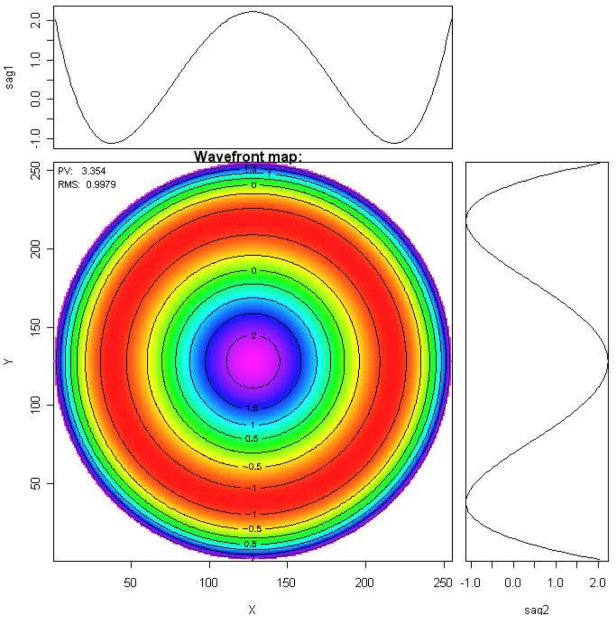

Z9

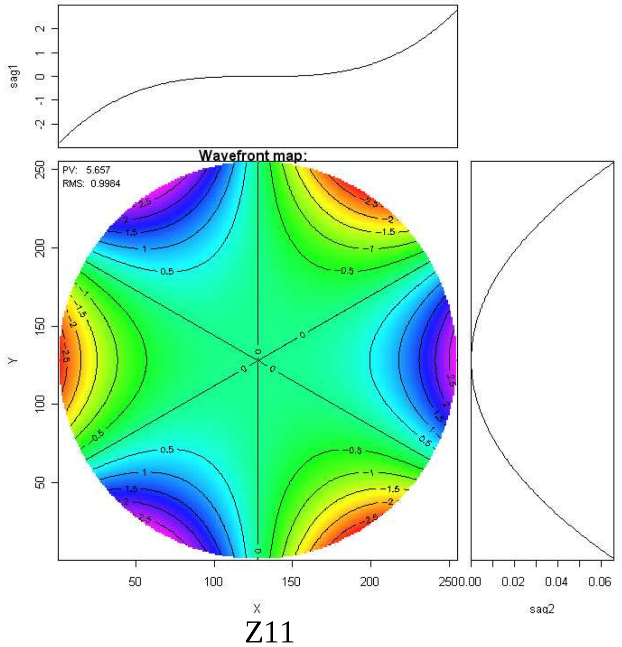

Z10

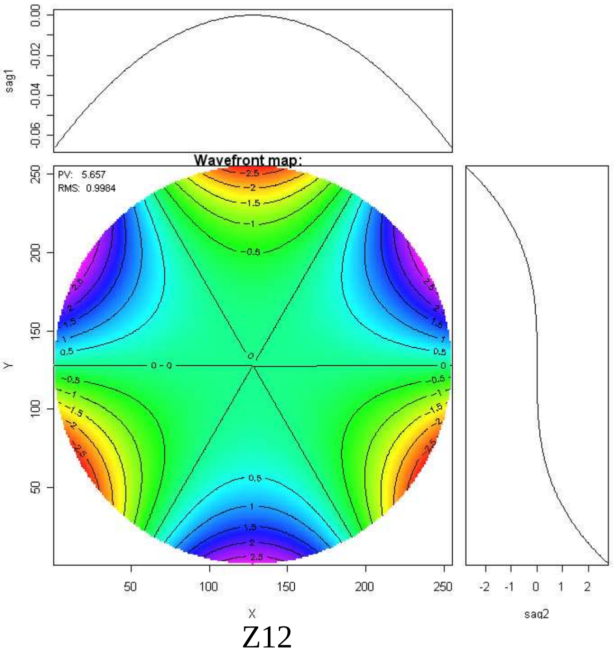

Z11

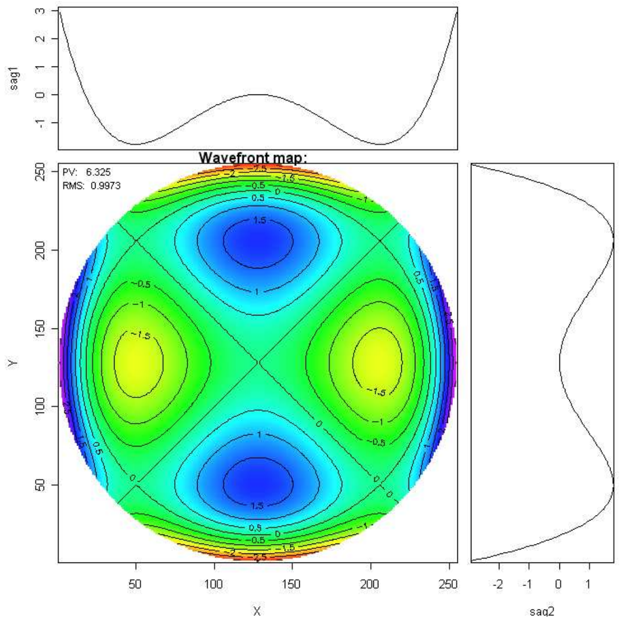

Z12

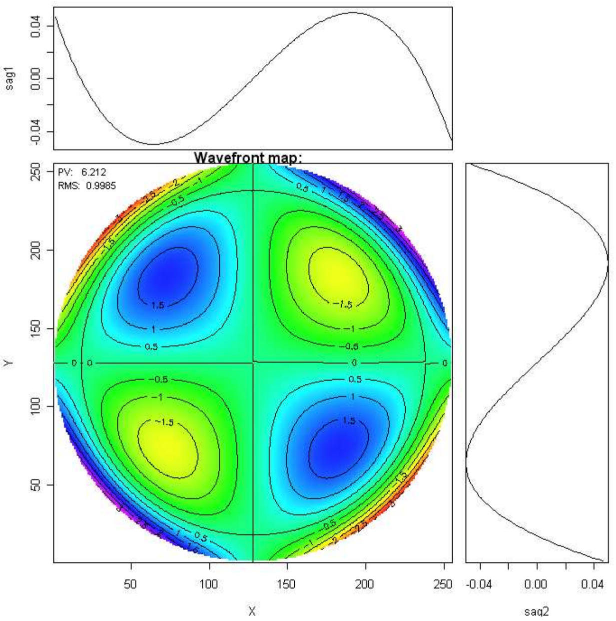

Z13

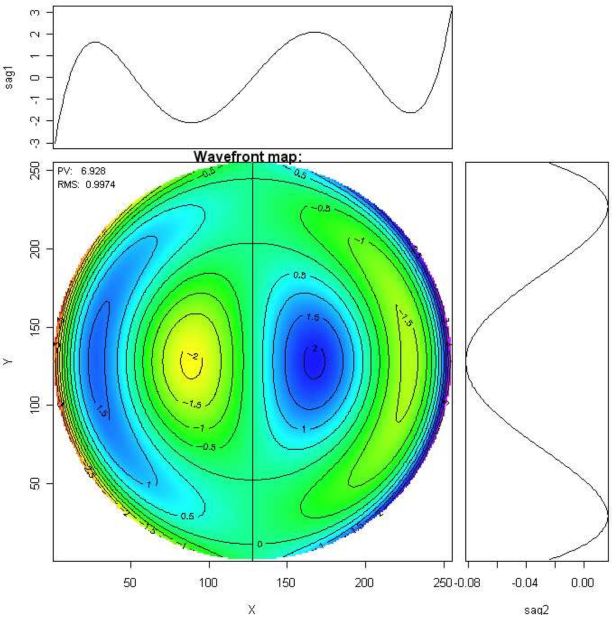

Z14

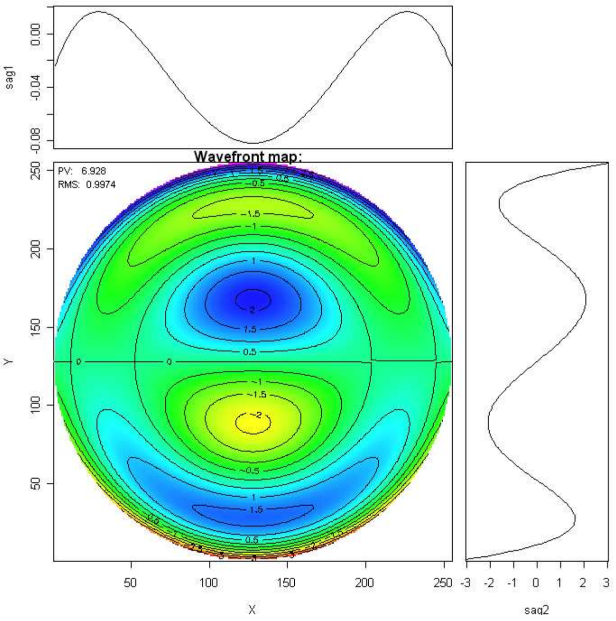

Z15

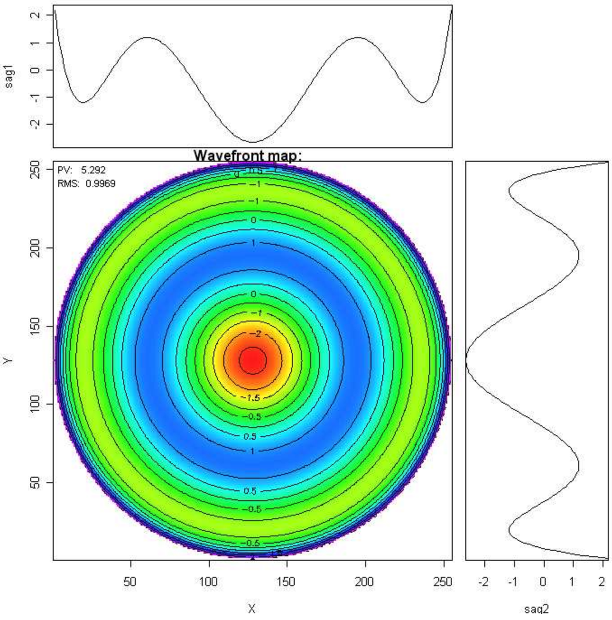

Z16

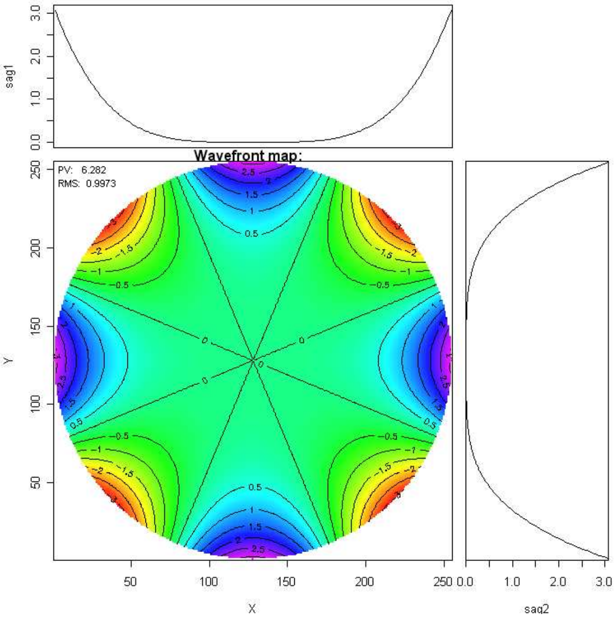

Z17

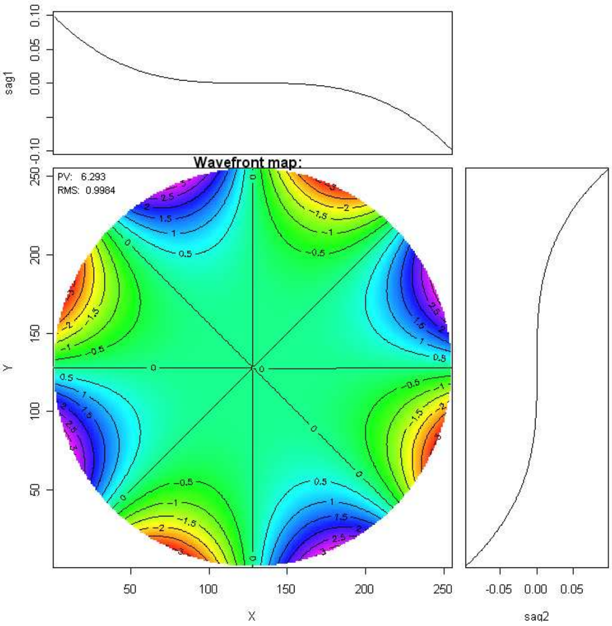

Z18

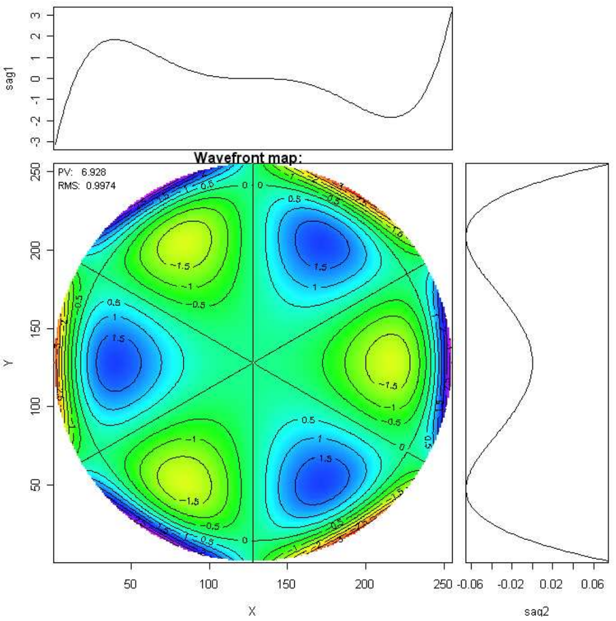

Ringraziamenti

Un grandissimo grazie diviso poche persone!!!

Il mio grazie è per

Emilio e la sua meravigliosa famiglia, prima o poi mi devi riportare a S.Andres a cenare!!! Io aspetto.

Giorgio che so che non leggerà mai queste righe ma che è stata sempre una presenza fondamentale nel mio "restare" qui. Ed ora finalmente è tornato!

Ruben, mi ha insegnato piu' di chiunque altro, nonostante il suo essere stato soltanto di passaggio qui.

Paolo, grazie.

Tutte le persone che mi sono accanto ogni giorno, a cui voglio bene, e che condividono tutta o solo una parte della loro vita con me, non hanno bisogno di comparire nei ringraziamenti di questo lavoro...
Sono loro a dare un vero "senso" a tutto!

Bibliography

[1] *http://en.wikipedia.org/wiki/stardate*.

[2] *http://www.ads-int.com/*.

[3] *http://www.brera.inaf.it/*.

[4] *http://www.ctio.noao.edu/ atokovin/tutorial/part3/wfs.html*.

[5] *http://www.eso.org/public/teles-instr/vlt.html*.

[6] *http://www.eso.org/sci/facilities/eelt/docs/index.html*.

[7] *http://www.eso.org/sci/facilities/eelt/telescope/index.html*.

[8] *http://www.eso.org/sci/facilities/lasilla/telescopes/ntt/*.

[9] *http://www.gemini.edu/*.

[10] *http://www.lbto.org/index.htm*.

[11] *http://www.microgate.it/engineering/adaptive-secondaries/projects/e-elt-m4*.

[12] *http://www.mmto.org/*.

[13] *http://www.oldscope.org/*.

[14] *http://www.ps.uci.edu/physics/news/chanan.html*.

[15] *http://www.sagem-ds.com/spip.php?rubrique32lang=en*.

[16] E. Viard N. Hubin A. Tokovinin, M. Le Louarn and R. Conan, *Optimized modal tomography in adaptive optics*, Astronomy and Astrophisics **Volume 7015** (2008), pp. 70153Q–70153Q–9.

[17] F. Schillke W. Wiedmann B. Doerband, S. Schulte, *Testing large plane mirrors with the ritchey-common test in two angular positions*, (1999).

[18] E.J.Cohen B.Catanzaro, J.A.Thomas, *Comparision of full-aperture interferometry to subaperture stitched interferometry for a large diameter fast mirror*, Proc. SPIE **vol. 4444** (2001), 224.

[19] Roland Shack Ben C. Platt, *History and principles of shack-hartmann wavefront sensing*, Journal of Refractive Surgery **Volume 17** (2001).

[20] Devaney N. Jochum L. Ronquillo B. Cavaller L. Castro, J., *Status of the design and fabrication of the gtc mirrors*, Proc. SPIE **4003, 24** (2000).

[21] Bernard Delabre, *Optical design for an adaptive anastigmatic five-mirror extremely large telescope*, Astronomy and Astrophisics **vol. 487, Number 2** (2008), 389.

[22] Renè Descartes, *Discours de la methode*, 1637.

[23] G.Toso P.Spanò E.Molinari, D.Tresoldi, *Radetzky: a new, large grazing incidence interferometer for large plane surface testing*, Proc. SPIE **vol. 7015** (2008), 70153O.

[24] E.Pinna, *Applicazione del sensore a piramide alla misura di discontinuità del fronte d'onda.*, Degree Thesis (2003-2004).

[25] S. Esposito and A. Riccardi, *Pyramid wavefront sensor behavior in partial correction adaptive optic systems*, Astronomy and Astrophisics **369, Number 2** (2001), L9 – L12.

[26] Duncan et al., *Precision surface figure measurements of large flat mirrors using grazing incidence interferometery*, Current Developments in Optical Engineering II **vol. 818** (1987), 373.

[27] Elssner et al., *Absolute sphericity measurements*, Applied Optics **vol. 28** (1989), 4649.

[28] Luca Pasquini et al., *Codex: the high resolution visual spectrograph for the e-elt*, **vol. 51** (2008), 7014E.

[29] Murty et al., *An oblique incidence interferometer*, Optical Engineering **vol. 15(5)** (1976), 461.

[30] Saunders et al., *Interferometer for large surfaces*, Journal of Research of the National Bureau of Standards **vol. 62, no 4** (1959), 2986.

[31] Jean-Gabriel Cuby et all, *Eagle: an moao fed multi-ifu working in the nir on the e-elt*, (2009), 7439B.

[32] Vernet et all, *The field stabilization and adaptive optics mirrors for the european extremely large telescope*, SPIE Vol. 7015, 70150S (2008).

[33] Galileo Galilei, *Sidereus nuncius*, Baglioni, Venezia, 1610.

[34] Frank Dekens Scott Michaels Jerry Nelson Terry Mast Gary Chanan, Mitchell Troy and David Kirkman, *Phasing the mirror segments of the keck telescopes: The broadband phasing algorithm*, Applied Optics **vol. 37** (1998), 140.

[35] R.D.Day G.N.Lawrence, *Interferometric characterization of full sphere:data reduction techniques*, Applied Optics **vol. 26, Issue 22** (1987), 4875.

[36] E-ELT Science Working Group, *An expanded view of the universe - science with the european extremely large telescope*, (2010).

[37] Hariharan, *Improved oblique-incidence interferometer*, Optical Engineering **vol. 14(3)** (1975), 80.

[38] A. N. KOLMOGOROV, *Dissipation of energy in the locally isotropic turbulence.*, Comptes rendus (Doklady) de l'Académie des Sciences de l'U.R.S.S. **32** (1941 a), 16–18.

[39] ———, *The local structure of turbulence in incompressible viscous fluid for very large reynold's numbers.*, Comptes rendus (Doklady) de l'Académie des Sciences de l'U.R.S.S. **30** (1941 a), 301–305.

[40] Dietrich Korsch, *Closed form solution for three-mirror telescopes, corrected for spherical aberration, coma, astigmatism, and field curvature*, Appl. Opt. **vol. 11** (1972), 2986–2987.

[41] Eriksson H. Löfdahl M., *An algorithm for resolving 2 ambiguities in interferometric measurements by use of multiple wavelengths*, Opt. Eng. **vol. 40** (2001), 2019.

[42] Daniel Malacara, *Optical shop testing*, WILEY, 2007.

[43] Christophe Verinau Natalia Yaitskova Pierre Baudoz Anthony Boccaletti Raffaele G. Gratton Norbert Hubin Florian Kerber Ronald Roelfsema Hans Martin Schmid Niranjan A. Thatte K. Dohlen M. Feldt Lars Venema S. Wolf Markus E. Kasper, Jean-Luc Beuzit, *Epics, the exoplanet imager for the e-elt*, (2008).

[44] E. Vernet N. Hubin, *Technical specifications for the conceptual design, prototyping, preliminary design of the m4 adaptive unit for the e-elt*, (2007).

[45] R. Geyl J. Paseri M. Cayrel P. Béraud P. Dierickx, D. Enard, *The vlt primary mirrors: mirror production and measured performance*, www.eso.org.

[46] Francois Roddier, *Curvature sensing and compensation: a new concept in adaptive optics*, Applied Optics **Vol. 27, No. 7** (1988), 1223.

[47] Erik Novak Sen Han and Mike Schurig, *Ritchey-common test used for measurement of astronomical optic*, Proceeding of SPIE **vol. 4842** (2003), 270.

[48] K.L. Shu, *Ray-trace analysis and data reduction methods for the ritchey-common test*, Applied Optics **vol. 22** (1983), 1879.

[49] Paolo Spanò, *Free-forms optics into astronomical use: the case of an all-mirror anamorphic collimator*, SPIE **Volume 7018** (2008).

[50] V. I. Tatarski, *Wave propagation in a turbulent medium.*, McGraw-Hill. (1961).

[51] B. Truax, *Absolute interferometric testing of spherical surfaces*, Proc. SPIE **Volume 1400** (1990).

[52] Robert K. Tyson, *Introduction to adaptive optics*, SPIE, 2000.

[53] B.Leibundgut WG1: M.Franx, *Science cases and requirements for the eso elt*, Tech. report, april 2006.

[54] R.N. Wilson, *Reflecting telescope optics ii*, Astronomy and Astrophysic Library, 1999.

[55] ______, *Reflecting telescope optics i*, Astronomy and Astrophysic Library, 2007.

[56] Zanotti D. Xompero M., Riccardi A., *Adaptive secondary mirror for lbt and its capacitive sensors: how can we calibrate them?*, Proceedings of the SPIE **Volume 7015** (2008), pp. 70153Q–70153Q–9.

[57] R. Mazzoleni; F. Gonté; I. Surdej; C. Araujo; R. Brast; F. Derie; P. Duhoux; C. Dupuy; C. Frank; R. Karban; L. Noethe; N. Yaitskova, *Design and performances of the shack-hartmann sensor within the active phasing experiment*, Proceeding SPIE **vol. 7012** (2008).

[58] P. R. Yoder, *Opto-mechanical systems design*, SPIE Press, 2005.